JUKKA KOLEHMAINEN

# Aluminium Oxide Coatings for Electrical Insulation of Hard Carbon Thin Film Sensors

Tampere University Dissertations 855

Tampere University Dissertations 855

JUKKA KOLEHMAINEN

# Aluminium Oxide Coatings for Electrical Insulation of Hard Carbon Thin Film Sensors

ACADEMIC DISSERTATION
To be presented, with the permission of
the Faculty of Engineering and Natural Sciences
of Tampere University,
for public discussion in the K1702
of the Konetalo building, Korkeakoulunkatu 6, Tampere,
on 6 October 2023, at 12 o'clock.

ACADEMIC DISSERTATION
Tampere University, Faculty of Engineering and Natural Sciences
Finland

| | | |
|---|---|---|
| *Responsible supervisor and Custos* | Professor Emeritus Petri Vuoristo<br>Tampere University<br>Finland | |
| *Supervisor* | Professor Jukka Vanhala<br>Tampere University<br>Finland | |
| *Pre-examiners* | Assistant Prof. Dr Ashish Ganvir<br>University of Turku<br>Finland | Privatdoz. Dr Lutz-Michael Berger<br>Fraunhofer Institute IKTS<br>Germany |
| *Opponents* | Privatdoz. Dr Lutz-Michael Berger<br>Fraunhofer Institute IKTS<br>Germany | Prof. Dr Erja Turunen<br>VTT Technical Research Centre of Finland<br>Finland |

The originality of this thesis has been checked using the Turnitin OriginalityCheck service.

Copyright ©2023 Jukka Kolehmainen

Cover design: Roihu Inc.

ISBN 978-952-03-3039-2 (print)
ISBN 978-952-03-3040-8 (pdf)
ISSN 2489-9860 (print)
ISSN 2490-0028 (pdf)
http://urn.fi/URN:ISBN:978-952-03-3040-8

Carbon dioxide emissions from printing Tampere University dissertations have been compensated.

PunaMusta Oy – Yliopistopaino
Joensuu 2023

# PREFACE

This dissertation work was carried out at Oerlikon Balzers Coating Finland Oy during the period from 2019 to 2023. I want to express my gratitude to the team leader Dr Juergen Becker for the opportunity to conduct this research at Oerlikon Balzers.

I am grateful to my supervisors Prof. Petri Vuoristo and Prof. Jukka Vanhala for the help and comments I received during this study. The guidance of Prof. Vuoristo on thermal spray coatings and magnetron sputtering has been a great help in this study.

I wish to express my gratitude to pre-examiners Privatdoz. Dr Lutz-Michael Berger and Assistant Prof. Dr Ashish Ganvir for their guidance and valuable comments.

I want to express special thanks to my team members Sanna Tervakangas M.Sc., Juha Haikola M.Sc. and Esa Haikola B.Sc. for preparing the test equipment and samples for the measurements. I wish to thank Dr Astrid Gies for her help on the SEM and XRD analysis of PVD aluminium oxide coatings, and Dr Tommi Varis and Dr Jussi Laurila for preparing the thermal spray aluminium oxide coatings and SEM analysis of the test samples for the study, respectively.

I want to thank Dr Oliver Hunold for reading the manuscript before publishing.

I also wish to express my gratitude to my wife Anne and my son Juhani for the loving and encouraging support that has been of such importance in the process to accomplish this thesis.

6th October 2023, Espoo, Finland

Jukka Kolehmainen

# ABSTRACT

Thin film sensors embedded into the component level of machines are future solutions to bring functionality and control to automotive and industrial applications, such as autonomous control functions and robotics. Piezoresistive hard carbon thin film sensors represent this kind of approach to the function of sensing temperature and strain conditions on component level, as they possess a high sensitivity for measurement of physical actions with components of small dimensions and tight tolerances.

Piezoresistive hard carbon sensors, when applied on steel substrates, have to be isolated from the electrically conductive substrate. Two basic requirements were set for the necessary electrical insulation. The first requirement was a minimum resistivity of $10^8$ Ωm over the temperature range between -10 °C and +100 °C under ambient air conditions of 20% RH, and the second one was the breakdown voltage of the insulating layer up to 200 VDC. However, there were several open questions in the leakage current measurements, related to the stability of the aluminium oxide layers when determining the resistivity of the coatings when they were exposed to changing ambient conditions. Much of the work in the study consisted of leakage current measurements performed as step response type measurements of 30 min transient periods in consecutive steps.

Atmospheric plasma spray (APS), high velocity oxygen fuel (HVOF) and physical vapour deposition (PVD) aluminium oxide coatings were investigated as-deposited, without additional post-treatment. All the APS and HVOF coatings fulfilled the set requirements at coating thicknesses over 40 µm. The practical range for thermal spray coatings was between 40–100 µm with resistivity between $10^{10}$ and $10^{11}$ Ωm. A slightly higher resistivity of between $5 \times 10^{10}$–$10^{12}$ Ωm was measured from suspension high velocity oxygen fuel coatings (S-HVOF). Thicker APS coatings demonstrated a much longer humidity-related current drift time in leakage current to decrease to a constant level.

Resistivity in the PVD aluminium oxide coatings varied between $4x10^9$–$10^{12}$ Ωm, which was influenced by the high defect density observed in the resistance screening of the samples. Practical minimum thickness for PVD aluminium oxide coatings was estimated to be between 2 and 3 μm to fulfil the requirement of a voltage duration of 200 V. Drift caused by humidity was also observed with the PVD aluminium oxide coatings but the stability in the leakage current was reached much faster than with the thermal spray coatings.

The thin PVD films made of Ti6Al4V as counter electrodes in the determination of leakage current, and as the contact pads of the piezoresistive hard carbon thin films highlighted the influence of surface roughness and porosity of the insulating layers under variable ambient conditions, especially with thermal spray insulating coatings. The Ti6Al4V films deposited were conformal and conductive enough for measurements but not pinhole-free, which allowed the permeation of moisture. The advantage of this was the possibility to study the ionic space charge polarization of water in the aluminium oxide layers with leakage current measurements under different temperature and humidity conditions. The polarization phenomena of aluminium oxide coatings were complex, starting from adsorbed water in chemisorbed state, changing to physiosorbed and finally to ionic movement in the electric field and anodic corrosion on the mild steel substrates. Direct current measurement cannot distinguish between surface and bulk conductivity but the rapid changes in leakage current seen close to the dew point temperatures implied that the huge changes measured in resistivity were related more to changes in surface resistivity caused by the condensed water on the hydrophilic γ-aluminium oxide surfaces of the thermal spray aluminium oxide coatings. This is also supported by the fact that the APS coatings without the use of a sealant showed a similar change in resistance close to dew point conditions at 80% RH. The adsorbed water in the aluminium oxide coatings caused more long-term drift influenced by the effect of ionic movement in the space charge polarization.

Measurements of the thermistor beta value and gauge factor of the hard carbon thin film sensor elements on thermal spray coatings as-deposited were new and the results were encouraging for future work with embedded hard carbon sensors. The conformity of the Ti6Al4V contact electrode and hard carbon layers was good over rough aluminium oxide coatings. The conductivity and functionality of the sensor

layers were achieved by compensating for the thickness of the thin film layers. The good adhesion of the hard carbon layer on the aluminium oxide dielectric coatings was also a positive result seen in the study of mechanical fatigue resistance. It was observed that the roughness of the thermal spray aluminium oxide coatings brought additional improvement by means of mechanical adhesion to the PVD sensor thin film layers.

In this study it has been demonstrated successfully that it is possible to deposit functional piezoresistive hard carbon thin film sensors on steel substrates by using as-deposited APS and HVOF thermal spray aluminium oxide coatings for electrical insulation between the sensing element and the substrate. The beta value 1070 ± 15 and gauge factor 5.83 ± 0.46 of such sensors are comparable to those earlier measured on a polyimide substrate.

The scientific novelty of the thesis is also the extensive study of moisture-induced polarization effects in porous aluminium oxide structures performed with the direct current measurement concept developed for the measurement of leakage current in electrical insulating coatings.

# AUTHOR'S CONTRIBUTION

Jukka Kolehmainen was the principal researcher and the writer of this thesis. He has developed PVD vacuum cathodic arc coating technology for the thin film deposition of piezoresistive hard carbon and Ti6Al4V electrode coatings. He has planned and organized the experiments with development of the test equipment for the measurements and performed the analysis of leakage current, piezoresistive strain and thermistor properties. The deposition of the thin film coatings for experiments and measurements and build up or test equipment have been performed with the help of the research team members Sanna Tervakangas M.Sc., Juha Haikola M.Sc. and Esa Haikola B.Sc.

APS and HVOF aluminium oxide coatings deposited on the cantilever beam samples were provided for the research by Dr Tommi Varis. The SEM and EDS measurements of the APS and HVOF samples and Ti6Al4V electrode thin film layers were performed by Dr Jussi Laurila at Tampere University.

Dr Astrid Gies helped with the delivery of suspension thermal spray S-HVOF, sealed APS thermal spray and PVD coatings for the testing and analysis in the study. She also provided SEM and XRD measurements of the PVD aluminium oxide coatings.

Prof. Petri Vuoristo and Prof. Jukka Vanhala gave advice on the experimental part and commented on the manuscript.

# CONTENTS

Preface ... iii

Abstract ... v

Author's contribution ... viii

List of symbols and abbreviations ... xxi

1 Introduction ... 27

2 Aim of the study ... 28

3 Embedded hard carbon thin film sensors ... 30
- 3.1 Structure and electrical conduction of hard carbon thin film sensor ... 30
- 3.2 Piezoresistance in hard carbon thin film ... 31

4 Requirements for electrical insulation in embedded hard carbon thin film sensors ... 33
- 4.1 Dielectric layer for electrical insulation of hard carbon sensors ... 33
- 4.2 Mechanical requirements for the dielectric layer ... 35

5 Dielectric materials for electrical insulation of hard carbon thin film sensors ... 37
- 5.1 Thermal spray deposition of $Al_2O_3$ coatings ... 39
- 5.2 Physical vapour deposition of $Al_2O_3$ coatings ... 42
- 5.3 $Al_2O_3$ as dielectric material for electrical insulation ... 50
  - 5.3.1 Electrical properties of thermal spray deposited $Al_2O_3$ coatings ... 52
    - 5.3.1.1 Resistivity of thermal spray $Al_2O_3$ coatings ... 55
    - 5.3.1.2 Relative permittivity of thermal spray $Al_2O_3$ coatings ... 58
    - 5.3.1.3 Dielectric strength of thermal spray $Al_2O_3$ based coatings ... 59
  - 5.3.2 Electrical properties of physical vapour deposited $Al_2O_3$ thin film coatings ... 62
    - 5.3.2.1 Growth and microstructure of sputter deposited $Al_2O_3$ thin films ... 63
    - 5.3.2.2 Resistivity of sputter deposited $Al_2O_3$ thin films ... 75

5.3.2.3 Relative permittivity of sputter deposited $Al_2O_3$ thin films ... 77
5.3.2.4 Dielectric strength of sputter deposited $Al_2O_3$ thin films ... 78
5.4 Summary of dielectric coatings applicable for electrical insulation of hard carbon sensors ... 79

6 Materials and methods ... 81
6.1 Substrate materials for $Al_2O_3$ coatings ... 81
6.2 Deposition of $Al_2O_3$ based coatings ... 83
6.2.1 APS and HVOF thermal spray of $Al_2O_3$ based coatings ... 83
6.2.2 PVD deposition of $Al_2O_3$ coatings by reactive RF sputtering ... 84
6.2.3 RF-sputtered aluminium oxide coatings ... 88
6.3 Test methods of electrically insulating coatings ... 89
6.3.1 Leakage current measurement of electrically insulating coatings ... 91
6.3.2 Capacitance measurement of electrically insulating coatings ... 92
6.3.3 Strain measurement of electrically insulating coatings performed with hard carbon thin film sensor ... 93

7 Results and discussion ... 96
7.1 General discussion of the experimental results ... 96
7.2 Electrical insulation of HVOF- and APS-deposited $Al_2O_3$ coatings ... 99
7.2.1 Structure of Ti6Al4V contact electrodes deposited on HVOF and APS insulating layers ... 100
7.2.2 Dielectric properties of HVOF- and APS-deposited thermal spray coatings ... 106
7.2.3 Leakage current in HVOF-deposited $Al_2O_3$ coatings ... 113
7.3 Influence of sealant resin on electrical resistance of APS $Al_2O_3$ coatings measured in humid conditions. ... 122
7.4 Electrical insulation of S-HVOF-deposited $Al_2O_3$ coatings ... 127
7.4.1 Structure of Ti6Al4V contact electrodes deposited on S-HVOF $Al_2O_3$ insulating layers ... 132
7.4.2 Dielectric properties of S-HVOF-deposited $Al_2O_3$ layers ... 133
7.4.3 Leakage current in S-HVOF-deposited $Al_2O_3$ coatings ... 134
7.5 Performance of piezoresistive hard carbon thin films deposited on thermally sprayed HVOF and APS $Al_2O_3$ coatings ... 138
7.5.1 Thermistor beta value of piezoresistive hard carbon thin films deposited on thermally sprayed HVOF and APS coatings ... 139
7.5.2 Strain sensitivity and gauge factor of piezoresistive carbon thin film deposited on thermally sprayed HVOF and APS coatings ... 143

7.5.3 Mechanical fatigue resistance of thermal spray $Al_2O_3$ measured with hard carbon thin film on a S235JR steel cantilever beam ..... 146
7.6 RF-sputter deposited PVD $Al_2O_3$ coatings on 90MnCrV8 tool steel samples ..... 151
7.6.1 Structure of PVD $Al_2O_3$ coatings deposited by RF sputtering. ..... 151
7.6.2 Resistivity of RF-sputtered PVD $Al_2O_3$ coatings ..... 166
7.6.3 Leakage current in RF-sputtered PVD $Al_2O_3$ coatings ..... 167

8 Conclusions ..... 173
8.1 Answer to the research questions ..... 175
8.2 Novelty of the study ..... 179

9 Suggestions for future work ..... 180

10 Bibliography ..... 181

## *List of Figures*

**Figure 1.** Planar structure of an embedded piezoresistive hard carbon thin film sensor. ..... 30

**Figure 2.** Schematic presentation of a plasma spray gun using DC power for plasma forming in APS [7]. ..... 40

**Figure 3.** Schematic presentation of an HVOF spray torch [7]. ..... 41

**Figure 4.** Principle of physical vapour deposition. ..... 42

**Figure 5.** Physical vapour deposition techniques [26]. ..... 43

**Figure 6.** Principle of planar magnetron for PVD sputtering [29]. ..... 44

**Figure 7.** Discharge voltage and total pressure behaviour during reactive magnetron sputtering of Al in an $Ar/O_2$ mixture. The argon pressure and total current were kept constant at 0.3 Pa and 0.3 A [28]. ..... 46

**Figure 8.** Schematic presentation of pulsed dual magnetron sputtering with bipolar operation. ..... 47

**Figure 9.** Schematic presentation of capacitively coupled RF sputtering. ....................... 49

**Figure 10.** Schematic presentation of a thermally sprayed metallic coating structure [7]. ........................................................................................ 54

**Figure 11.** The mechanism of water adsorption on a ceramic oxide surface: I. Chemisorption of water and formation of hydroxylated oxide surface; II. Physisorption of water; III. Dissociation of physisorbed water; and IV. Generation of protons responsible for $H^+$ ionic conduction [47]. ........................................................................................ 57

**Figure 12.** Thornton's zone diagram of film growth as a function of temperature $T/T_m$ and deposition pressure [70]. ............................................ 64

**Figure 13.** Cantilever beam of S235JR deposited with a thermal spray aluminium oxide layer (30x20 $mm^2$) and a test electrode of Ti6Al4V (10x10$mm^2$) on top of the layer. ........................................................... 81

**Figure 14.** Test disc of THYRODUR 2842 – 90MnCrV8. With PVD aluminium oxide coating and patterned Ti6Al4V contact pad layer deposited on the disc on the left. ......................................................... 82

**Figure 15.** Top left: Disc samples patterned with Ti6Al4V contact pad layer. Bottom left: Samples with the stencil mask are shown. Right: Fixturing of the stencil mask on the disc samples for patterning of the contact pads. ........................................................................................ 82

**Figure 16.** MeiVac MAK 2 sputter source with a two-inch aluminium target. ................ 85

**Figure 17.** MeiVac MAK 2 sputter connection to SEREN IPS R301 RF power supply with SEREN IPS AT3 automatic matching network and MC2 matching network controller. ....................................................... 85

**Figure 18.** RF-sputter deposition set-up in the vacuum chamber. .................................... 86

**Figure 19.** Heater with control set-up (left) and sample holder (right). ............................ 87

**Figure 20.** Calibration of substrate temperature with Omega IR sensor probe to heater temperature measured with a thermocouple. .................................... 87

**Figure 21.** Hysteresis in reactive RF sputtering of aluminium oxide coating at 200 °C. ........................................................................................ 88

**Figure 22.** Two-point measurement of sheet resistance of Ti6Al4V contact electrode on HVOF- and APS-deposited aluminium oxide coatings. ............ 90

**Figure 23.** Principle of leakage current measurement of aluminium oxide dielectric layers. ........ 91

**Figure 24.** Direct current measurement of cantilever beam test specimen. ........ 92

**Figure 25.** Strain measurement with piezoresistive carbon thin film. ........ 94

**Figure 26.** Bend test set-up for strain measurement of cantilever beam samples. ........ 94

**Figure 27.** Aluminium oxide samples placed on a Peltier cooling element for leakage current and capacitance measurement at temperatures between +5 and +50 ºC. ........ 97

**Figure 28.** HVOF- and APS-deposited insulating coatings on S235JR cantilever beams. ........ 99

**Figure 29.** Measured average roughness ($R_a$), mean roughness depth ($R_z$), maximum peak ($R_p$) and maximum valley roughness ($R_v$) of HVOF- and APS-deposited aluminium oxide and spinel coatings with comparison to polyimide as reference substrate ........ 100

**Figure 30.** Ti6Al4V contact electrodes of 10x10 $mm^2$ deposited on HVOF and APS test samples. ........ 101

**Figure 31.** Sheet resistances of contact electrodes on HVOF- and APS-deposited samples. ........ 101

**Figure 32.** SEM image of HVOF-deposited AlO1_70 surface with Ti6Al4V contact electrode layer on top of the rough coating surface. ........ 102

**Figure 33.** Cross-section of cantilever beam sample with HVOF-deposited AlO1_70 aluminium oxide insulation layer and Ti6Al4V electrode layer on top. ........ 103

**Figure 34.** Cross-section of Ti6Al4V layer on top of HVOF-deposited AlO1_70 sample. ........ 103

**Figure 35.** Slant view of Ti6Al4V layer on HVOF-deposited aluminium oxide. ........ 104

**Figure 36.** EDS mapping from a cross-section of HVOF-deposited AlO1_70 sample with Ti6Al4V top layer. ........ 105

**Figure 37.** EDS analysis from a cross-section of HVOF-deposited AlO1_70 sample with Ti6Al4V top layer. ........ 105

**Figure 38.** Leakage current of AlO1_70 sample in three consecutive measurement step runs....106

**Figure 39.** Leakage current of HVOF- and APS-deposited electrical insulation layers measured at a voltage level of 20 VDC....107

**Figure 40.** Leakage current of HVOF electrical insulation layer AlO1_70 in 10 and 20 VDC steps....108

**Figure 41.** Resistivity of HVOF- and APS-deposited electrical insulation layers calculated from 30 min average of leakage current measurements at 20 VDC....109

**Figure 42.** Resistivity of AlO5_70 and AlO5_200 samples measured on Peltier element in temperature range +5 °C to +55 °C....110

**Figure 43.** Capacitance of thermal spray coatings measured with an Amprobe LCR55A on a Peltier element as a function of substrate temperature in ambient air conditions of 21 °C and 20% RH....112

**Figure 44.** AlO1_70 sample kept for 4 days at 35 °C and 5% RH before leakage current measurement at 200 VDC....114

**Figure 45.** AlO1_70 sample exposed for 3h at 20 °C and 50% RH before leakage current measurement at 200 VDC....115

**Figure 46.** AlO1_70 sample exposed for 3h at 20 °C and 80% RH before leakage current measurement at 200 VDC....115

**Figure 47.** AlO1_70 sample exposed for 3h at 40 °C and 80% RH before leakage current measurement at 200 VDC....116

**Figure 48.** Leakage current at 200 VDC of AlO1_70 sample measured when voltage polarity was reversed at 5 min intervals....118

**Figure 49.** HVOF AlO1_70 sample after three exposures to conditions of 40 °C and 80% RH....119

**Figure 50.** Leakage current measured of the dried AlO1_70 sample at 200 VDC when polarity was reversed at 5 min intervals....119

**Figure 51.** Leakage current measurement at 200 VDC of the second AlO1_70 sample at 21.5 °C and 40% RH....120

**Figure 52.** Leakage current measurement at 200 VDC of the second AlO1_70 sample measured at 21 °C and 46% RH after treatment in an IPA ultrasonic bath for 5 min. ....................121

**Figure 53.** APS samples impregnated with two-component sealant for the study of dielectric properties....................122

**Figure 54.** Placing of APS samples in resistance measurement with type K thermoelement in Vötsch VCL 4003 climatic test cabinet. ....................123

**Figure 55.** Electrical resistance of APS samples measured between - 10 °C and + 30° C before exposure to humidity. ....................124

**Figure 56.** Electrical resistance of APS coatings at 40 °C in a cyclic change of humidity from 80% RH to 40% RH and back to 80% RH. ....................125

**Figure 57.** Electrical resistance of APS samples measured between -10 °C and +30 °C after exposure to 80% RH. ....................126

**Figure 58.** APS insulating samples on S235JR cantilever beam after the study of exposure to humidity....................127

**Figure 59.** Suspension-HVOF coatings on S235JR cantilever beam samples for study of electrical insulation resistance with direct current measurement....................128

**Figure 60.** Measured average roughness ($R_a$), mean roughness depth ($R_z$), maximum peak ($R_p$) and maximum valley roughness ($R_v$) of S-HVOF coating samples in comparison to 40 µm HVOF AlO1_40 as a reference sample....................129

**Figure 61.** Optical cross section image of 12 µm thick S-HVOF aluminium oxide layer of 210012TC sample deposited from suspension B....................130

**Figure 62.** Optical cross section image of 220 µm S-HVOF aluminium oxide layer of 210016TC sample deposited from suspension A with NiCr bond coat....................130

**Figure 63.** SEM cross section image of 220 µm S-HVOF aluminium oxide layer of 210016TC deposited from suspension A. ....................131

**Figure 64.** SEM cross-section image of 75 µm S-HVOF aluminium oxide layer of 200076TC deposited from suspension A. ....................131

**Figure 65.** Sheet resistance of Ti6Al4V contact electrodes measured from S-HVOF aluminium oxide samples deposited from feedstock suspensions A and B....132

**Figure 66.** Leakage current measurement of 50 µm S-HVOF aluminium oxide sample 200075TC deposited from suspension A....135

**Figure 67.** Leakage current measurement of 40 µm HVOF aluminium oxide reference sample AlO1_40....135

**Figure 68.** Leakage current measurement of 200 µm S-HVOF aluminium oxide sample 210015TC deposited from suspension B....136

**Figure 69.** Resistivity of S-HVOF coatings measured under different humidity conditions....137

**Figure 70.** Leakage current of 70 µm S-HVOF aluminium oxide coating in three consecutive direct current measurements performed at 20.3 °C and 18.4% RH....138

**Figure 71.** Resistance measurement of hard carbon thin film sensor structure deposited on HVOF and APS dielectric coatings on S235JR cantilever beams....139

**Figure 72.** Resistance measurement of piezoresistive hard carbon thin film thermistors on HVOF and APS insulating coatings to determine thermistor beta value....140

**Figure 73.** Temperature sensitivity of resistance in piezoresistive hard carbon thin films deposited on HVOF and APS aluminium oxide coatings....141

**Figure 74.** Determination of thermistor β value of piezoresistive hard carbon thin films on HVOF and APS coatings with a linear regression fit model....142

**Figure 75.** Resistance change of 750 nm hard carbon film deposited on AlO1_70 sample in strain measurement with cyclic 1 mm deflection of S235JR cantilever beam....145

**Figure 76.** Gauge factor of hard carbon film on 200 µm APS $Al_2O_3$ layer and bending force of 3 mm deflection in mechanical fatigue resistance measurement....147

**Figure 77.** APS $Al_2O_3$ sample after measurement of mechanical fatigue resistance on the S235JR cantilever beam....148

**Figure 78.** Optical image of contact interface between hard carbon layer and Ti6Al4V contact pad after fatigue resistance measurement. ........................148

**Figure 79.** Deflection of cantilever beam at the anchor point (x=0) caused by plastic deformation. ........................149

**Figure 80.** Force-deflection relation measured at end point C of S235JR cantilever beam. ........................149

**Figure 81.** Correlation of resistance $R_0$ with ambient temperature conditions during fatigue resistance measurement. ........................150

**Figure 82.** Samples of RF-sputtered $Al_2O_3$ coatings deposited at room temperature with Ti6Al4V metallic contact matrix of 3x3mm$^2$ and 1x1mm$^2$ elements as a top layer. ........................151

**Figure 83.** Average roughness ($R_a$), mean roughness depth ($R_z$), maximum peak ($R_p$) and maximum valley roughness ($R_v$) of RF-sputtered $Al_2O_3$ coatings measured with a Dektak XT profilometer. ........................152

**Figure 84.** Optical image of RF-sputtered $Al_2O_3$ sample 120721A1 of 0.58 μm deposited at 20 °C (RT). ........................153

**Figure 85.** Optical image of RF-sputtered $Al_2O_3$ sample 040821A1 of 0.85 μm deposited at 125 °C. ........................153

**Figure 86.** Optical image of RF-sputtered $Al_2O_3$ sample 050821A1 of 1.3 μm deposited at 250 °C. ........................154

**Figure 87.** SEM surface image of RF-sputtered $Al_2O_3$ sample 120721A1 deposited at 20 °C. ........................154

**Figure 88.** SEM cross-section image of RF-sputtered aluminium oxide sample 120721A1. ........................155

**Figure 89.** SEM surface image of sample 261121A (scale bar: 10 μm) ........................156

**Figure 90.** SEM surface image of sample 261121A1(scale bar: 1 μm). ........................157

**Figure 91.** SEM cross-section image of sample 261121A1 (scale bar: 300 nm) ........................157

**Figure 92.** XRD pattern of sample 261121A1. ........................158

**Figure 93.** SEM surface image of sample 301221A1 (scale bar: 10 μm). ........................158

**Figure 94.** SEM surface image of sample 301221A1 (scale bar: 1 μm). ......159

**Figure 95.** SEM cross-section image of sample 301221A1 (scale bar: 1 μm). ......159

**Figure 96.** XRD pattern of sample 301221A1. ......160

**Figure 97.** SEM surface image of sample 160921A1 (scale bar: 10 μm). ......161

**Figure 98.** SEM surface image of sample 160921A1 (scale bar: 1 μm). ......161

**Figure 99.** SEM cross-section image of sample 160921A1(scale bar: 1 μm). ......162

**Figure 100.** SEM surface image of sample 240921A1 (scale bar: 10 μm). ......162

**Figure 101.** SEM surface image of sample 240921A1 (scale bar: 1 μm). ......163

**Figure 102.** SEM cross-section image of sample 240921A1(scale bar: 1 μm). ......163

**Figure 103.** SEM surface image of sample 280921A1 (scale bar: 10 μm). ......164

**Figure 104.** SEM surface image of sample 280921A1 (scale bar: 2 μm). ......164

**Figure 105.** SEM cross-section image of sample 280921A1 (scale bar: 1 μm). ......165

**Figure 106.** XRD patterns of samples 160921A1, 240921A1 and 280921A1 ......165

**Figure 107.** Resistance screening of RF-sputtered Al203 sample 050821A1. Contact pads marked in green possessed a resistance of over 2 MΩ. ......166

**Figure 108.** Leakage current measurement of 1.3 μm thick RF-sputtered sample 050821A1at 50 V and at 18 °C and 49.7% RH ......168

**Figure 109.** Leakage current measurement of 1.3 μm RF-sputtered sample 050821A1 at 100 V and at 19 °C and 47.2% RH. ......169

**Figure 110.** Leakage current measurement of 1.3 μm RF-sputtered sample 050821A1 at 200 V and at 21.7 °C and 69.9% RH. ......170

**Figure 111.** 1x1 $mm^2$ electrode pad of the sample 050821A1 after leakage current measurement at 200 VDC level. ......170

**Figure 112.** Leakage current measurement of 1.7 μm thick RF-sputtered sample 261121A1 at 200 V and at 20.9 °C and 8.7% RH. ......171

**Figure 113.** Leakage current of 8.8 μm thick RF-sputtered sample 301221A1 at 200 V and at 21.7 °C and 13.2% RH in three consecutive measurement runs. 172

List of Tables

**Table 1.** Common processing routes resulting in formation of different metastable $Al_2O_3$ structures and the sequences of phase transformations towards the stable $\alpha$-$Al_2O_3$ phase [45]. 51

**Table 2.** APS and HVOF thermal spray deposited aluminium oxide samples from the study. 84

**Table 3.** PVD aluminium oxide coatings deposited by RF sputtering. 89

**Table 4.** Capacitance and relative permittivity of thermal spray electrical insulation layers measured at 21 °C and 20% RH. 111

**Table 5.** Capacitance and relative permittivity of thermal spray coatings at +50 °C. 113

**Table 6.** Dielectric properties of S-HVOF coatings deposited from suspensions A and B 133

**Table 7.** Average resistivity of S-HVOF coatings calculated from leakage current measurements. 136

**Table 8.** Beta values of carbon thin film measured on HVOF and APS thermal spray coatings. 143

**Table 9.** Parameters of S235JR cantilever beam used in gauge factor calculation. 144

**Table 10.** Calculated gauge factor of 750 nm hard carbon thin film on thermal spray coatings measured at 1 mm cyclic deflection of S235JR cantilever beam. 145

**Table 11.** Mechanical properties and chemical composition of RF-sputtered $Al_2O_3$ coatings. 155

**Table 12.** RF-sputtered AlO3 samples screened with criterion of $R_{pad}$ resistance > 2 MΩ. 167

**Table 13.** Resistivity of RF-sputtered $Al_2O_3$ coatings calculated from leakage current measurements. ....................................................................................168

# LIST OF SYMBOLS AND ABBREVIATIONS

| | |
|---|---|
| $\alpha$-$Al_2O_3$ | Alpha phase aluminium oxide |
| $Al_2O_3$-30%MgO | Magnesium aluminate spinel |
| $Al_2O_3$-3%$TiO_2$ | Alumina titania |
| $A_{target}$ | Target surface area |
| $A_{substrate}$ | Substrate surface area |
| $\beta$ | Thermistor beta value |
| C | Carbon |
| $C_m$ | Measured capacitance |
| $C_o$ | Geometrical capacitance of the specimen in vacuum |
| Cr | Real capacitance |
| $Cr_2O_3$ | Chromium oxide |
| d | Thickness of the cantilever beam |
| E | Elastic modulus |
| $\varepsilon$ | Strain |
| $\varepsilon_o$ | Vacuum permittivity |
| $\varepsilon_r$ | Real part of relative permittivity |

| | |
|---|---|
| $\varepsilon^*_r$ | Total relative permittivity |
| $\varepsilon'_r$ | Complex part of relative permittivity |
| $\gamma$-$Al_2O_3$ | Gamma phase aluminium oxide |
| I | Second moment of area |
| L | Length of the cantilever beam |
| M | Moment |
| $\omega$ | Angular frequency |
| ɯ | Deflection |
| ɯc | Deflection at point C |
| P | Bending force |
| $P_c$ | Cyclic bending force |
| $\pi$ | Pi bond |
| $\varrho$ | Resistivity |
| $R_a$ | Roughness average |
| $R_0$ | Resistance at reference temperature |
| $R_p$ | Maximum profile peak height |
| $R_{pad}$ | Resistance of the contact pad to the substrate |
| $R_v$ | Maximum valley depth |
| $R_z$ | Mean roughness depth |

| | |
|---|---|
| $\sigma$ | Stress |
| $\sigma_y$ | Yield strength |
| Ti6Al4V | Titanium alloy grade 5 |
| $T_m$ | Melting temperature |
| $T_0$ | Reference temperature |
| Um | Measured voltage over shunt resistor |
| $V_{target}$ | Target voltage |
| $V_{substrate}$ | Substrate voltage |
| w | Width of the cantilever beam |
| Z | Elastic section modulus |

| | |
|---|---|
| ALD | Atomic layer deposition |
| APS | Atmospheric plasma spray |
| CVD | Chemical vapour deposition |
| DBS | Dielectric breakdown strength |
| DC | Direct current |
| DMS | Dual magnetron sputtering system |
| DOMS | Deep oscillation magnetron sputtering |

| | |
|---|---|
| DVS | Dynamic vapour sorption |
| EDS | Energy dispersive X-ray spectroscopy |
| EIT | Indentation elastic modulus |
| ERDA | Elastic recoil detection analysis |
| GF | Gauge factor |
| GIXRD | Grazing incidence X-ray diffraction |
| HiPIMS | High power impulse magnetron sputtering |
| HIT | Indentation hardness |
| HVOF | High velocity oxygen fuel |
| IMS | Ionized reactive sputtering |
| IPA | Isopropyl alcohol |
| LPPS | Low pressure plasma spray |
| MF | Medium frequency |
| NTC | Negative temperature coefficient |
| OFHC | Oxygen free high conductive copper |
| PEI | Plasma emission intensity |
| PVD | Physical vapour deposition |
| RBS | Rutherford backscattering spectrometry |
| RF | Radio frequency |

| | |
|---|---|
| RGA | Residual gas analyser |
| RT | Room temperature |
| SADP | Selected area diffraction pattern |
| SCCM | Standard cubic centimetres per minute |
| SEM | Scanning electron microscope |
| S-HVOF | Suspension high velocity oxygen fuel |
| TEM | Transmission electron microscopy |
| UHV | Ultra high vacuum |
| VDC | Voltage direct current |
| XRD | X-ray diffraction analysis |
| XRF | X-ray fluorescence |

# 1 INTRODUCTION

There is a growing demand for new control systems with built-in intelligence in the automotive and industrial automation sectors to sense and to steer the operation so as to reduce energy consumption and emissions, and to improve the life cycle management of the components. At the same time, the emergent complexity of control systems has introduced a need for a new type of embedded sensing integrated into the components of the system to control operations in a favourable way. This has made smart sensing materials essential in the development of detection and control of the operational conditions in vehicles and equipment.

A sensor is a device that receives a stimulus from operation and responds to it with an electrical signal [1]. The signals from embedded hard carbon thin film sensors will transmit information on the physical temperature and strain conditions found in the system. A carbon thin film sensor consists of an active piezoresistive hard carbon layer which is deposited by physical vapour deposition (PVD) on top of a dielectric insulating layer to isolate the carbon film and its metallic contact pads electrically from the conductive steel substrate shown in Figure 1. The piezoresistive hard carbon film possesses sensitivity for both temperature and strain, detected as a change in resistance. At the same time, the dielectric layer forms a parallel impedance between the sensing layer and the conductive steel substrate. The drift of the impedance has an influence on the measured resistance value of the piezoresistive sensing element and sets a limit for the accuracy of the temperature and strain measurements.

# 2 AIM OF THE STUDY

This study is related to materials science of the electrical properties in aluminium oxide coatings prepared by thermal spray and PVD sputtering techniques on steel substrates. The aim of the thesis is to understand the functionality of the aluminium oxide coatings that are used as a dielectric layer for embedded piezoresistive hard carbon thin film sensors on steel substrates. The research is focused on the study of the feasibility of APS and HVOF thermal spray and RF-sputtered PVD aluminium oxide coatings as-deposited without grinding or polishing as post-treatment for the electrical insulation from conductive substrates of piezoresistive sensor elements.

The research questions in the thesis are the following:

1. What thickness of APS and HVOF thermal spray or PVD aluminium oxide coating is required for effective electrical insulation on conductive steel substrates of piezoresistive hard carbon sensors?

2. How the ambient conditions, temperature and humidity influence on the dielectric properties and resistivity of aluminium oxide coatings deposited by thermal spray and PVD techniques?

3. What is the thermistor beta sensitivity of piezoresistive hard carbon films on as-deposited aluminium oxide coatings?

4. What is the gauge factor of piezoresistive hard carbon film measured on as-deposited aluminium oxide coatings?

5. What is the fatigue resistance of aluminium oxide coatings on steel substrate measured with piezoresistive hard carbon film?

6. How to improve the electrical insulation of thermal spray and PVD aluminium oxide coatings?

In the literature review of this thesis, at first the requirements for the electrical insulation of piezoresistive hard carbon sensors are presented, followed by a review of the deposition techniques applicable, together with known materials and methods for aluminium oxide coatings. The measurement methods applied for the study of the electrical properties of aluminium oxide coatings are described before a discussion of the electrical properties and measurement results of aluminium oxide coatings prepared by APS, HVOF and PVD.

# 3 EMBEDDED HARD CARBON THIN FILM SENSORS

The study concentrated on the requirements and technical performance of the aluminium oxide dielectric layers required for the electrical insulation of piezoresistive hard carbon thin film sensor elements on conductive metal substrates.

## 3.1 Structure and electrical conduction of hard carbon thin film sensor

The basic planar structure of embedded hard carbon sensor element is shown in Figure 1, where the dielectric insulating layer is depicted between the piezoresistive hard carbon sensing element film with metal contact pads and the conductive steel substrate.

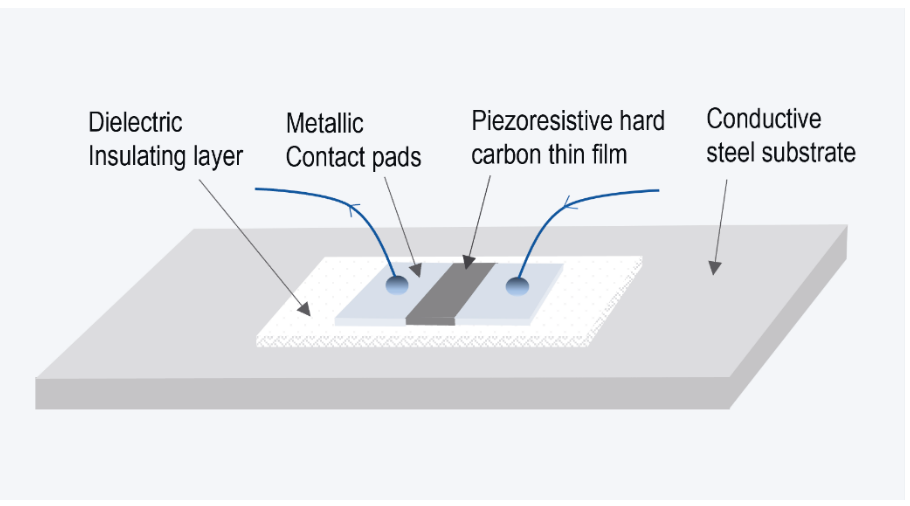


**Figure 1.** Planar structure of an embedded piezoresistive hard carbon thin film sensor.

Carbon can form bonds in three hybridizations: $sp^3$, $sp^2$ and $sp^1$, allowing the existence of a huge variety of crystalline and disordered forms of carbon materials. Hard carbon films deposited by arc evaporation possess an amorphous film structure with a random $sp^3$-bonded tetrahedral network and a small amount of $sp^2$-bonded carbon clusters in the structure. The $sp^3$ orbital configuration forms tetrahedrally directed strong σ bonds to adjacent carbon atoms, as in a diamond, but in an amorphous form without a long-range order. The fraction of $sp^2$ hybridized carbon forms a configuration with three of the valence electrons directed trigonally with strong σ bonds, as in graphite, and with the fourth valence electron in a pπ orbital which lies in the normal direction to the σ bonding plane. The σ bonds of all carbon sites form occupied σ states in the valence band and empty σ* states in the conduction band separated by a wide energy gap. The π bonds of $sp^2$ and $sp^1$ form filled π states and π* with a much narrower energy gap. In amorphous carbon, σ and π states lie at different energies and π states lie in an orthogonal plane to the σ bonds at $sp^2$ sites having only minor interaction. The $sp^2$ sites tend to form planar π bonded clusters of a certain size embedded in the $sp^3$ bonded matrix closest to the Fermi level $E_f$ controlling the electronic properties while the $sp^3$ matrix controls mechanical properties such as elastic modulus and hardness [2].

The resistivity of the amorphous hard carbon film is determined by the level of $sp^3/sp^2$ hybridization. The factors influencing the ratio are the carbon plasma kinetic energy and ionization, deposition rate and substrate heating, and potential dopants increasing the $sp^2$ defect level in the hard carbon film. The piezoresistive effect comes from the $sp^3$ matrix in the film acting as a tunnel barrier between the $sp^2$ clusters with a variable gap depending on the density and inhomogeneous disorder. The quantity of $sp^2$ sites give rise to a broad density of states in the π bands, which is the origin for thermal sensitivity in the resistivity of a hard carbon material [2], [3].

## 3.2 Piezoresistance in hard carbon thin film

Piezoresistive effect of semiconductive amorphous hard carbon film makes it sensitive for both temperature and strain. Typical resistance $R_0$ of a hard carbon thin film layer measured at room temperature varies between 100 kΩ and 500 kΩ for an element with a channel width/length ratio of 2.0 and layer thickness of 100–500 nm.

As a negative temperature coefficient (NTC) thermistor [4], the temperature sensitivity of a piezoresistive hard carbon element is determined at temperature T according to formula (1):

$$R = R_0 e^{\beta\left(\frac{1}{T} - \frac{1}{T_0}\right)}, \tag{1}$$

in which the measured beta value β is typically between 900 and 1200 when resistance $R_0$ of the hard carbon film is 100 kΩ at temperature $T_0$ of 295 K.

Gauge factor (GF) described in formula (5) as relative change in electrical resistance R, to the mechanical strain ε can vary significantly depending on $sp^3/sp^2$ ratio in carbon thin films [5]. The sensitivity of amorphous carbon strain gauges as a semiconductor can be ten to hundred times higher compared to metallic strain gauges [4].

# 4 REQUIREMENTS FOR ELECTRICAL INSULATION IN EMBEDDED HARD CARBON THIN FILM SENSORS

The dielectric material has the important function of isolating the carbon sensing layer from the conductive substrate in the design of embedded sensors. The electrical stability of the dielectric layer with low leakage current and drift in permittivity are the main factors influencing the measurement accuracy of sensor impedance. Good fracture toughness, and the strength of adhesion to the metallic substrate and to the piezoresistive carbon film are the factors which determine the boundaries for the operation conditions of the sensing element.

## 4.1 Dielectric layer for electrical insulation of hard carbon sensors

The resistivity and dielectric strength of the insulating material determine the required film thickness at the typical operating voltage level. The surface roughness and the finishing methods of the steel substrate have a major impact on the thin film coverage and conformal uniformity of the dielectric coating formed [6]. Steel surfaces after machining have grooves and burrs which, even after grinding and polishing, tend to leave cavities and pockets together with grinding particles, causing uneven thickness and coverage for thin film coatings.

Thermal spray coatings may have different surface roughness depending on coating method and powder material used [7]. Surface roughness is also influenced by grit blasting of the steel substrate needed to ensure the mechanical adhesion of the thermal sprayed coating on steel substrate.

The typical resistance $R_0$ of a piezoresistive hard carbon thin film layer measured at room temperature varies between 100 kΩ and 500 kΩ for an element with a channel width/length ratio of 2.0 and layer thickness of 100–500 nm. The dielectric layer

forms an impedance between the sensor element and the conductive substrate, acting as a parasitic path for conduction in parallel with the carbon layer. Defects such as impurities, cavities and holes found in the dielectric layer can cause a short circuit of the carbon film or the contact pads to the conductive substrate. Polarization of the dielectric layer causes an additional change in the impedance between the substrate and sensor element which has a direct influence on the accuracy of the measured resistance [8]. The relative dR/R change caused by the drift in the dielectric layer must be limited to the level needed to achieve accuracy.

For such a piezoresistive sensor element the temperature sensitivity of resistance dR/dT is typically 1 kΩ/K. When an accuracy of 0.1 K is requested for the detection level in the temperature measurement of a 100 kΩ hard carbon element then the effect on the measured resistance R caused by the parallel impedance of the dielectric layer between the sensor film and conductive substrate should be reduced to less than 100 Ω. This sets the requirement for the minimum resistance of the insulating layer impedance to the level of 100 MΩ.

Most of the dielectric coatings applicable for electrical insulation have a dielectric strength far below 50 MV/m, which sets a minimum requirement for the coating thickness of 2–5 μm. Additional thickness for the dielectric layer is needed depending on the substrate and layer roughness and porosity to avoid electrical break down or increase in leakage current caused by Poole-Frenkel emission [9] in the dielectric layer. A resistivity of $10^8$ Ωm is a practical minimum level set for dielectric material. This is related to the change in resistivity of the dielectric layer to a 1% dR/R change in the measured hard carbon thin film.

The polarization of the dielectric layer in the planar structure determines the impedance of the capacitive element formed between the thin film sensor layers of conductive carbon and metal contact pads and the substrate. Four different types of polarization: electronic, ionic, dipolar, and space charge, have an influence on the measured impedance depending on the frequency range of operation [8]. Electronic, ionic and dipolar polarizations are all relatively fast processes in the uniform volume of the element, but space charge polarization is a slow, non-linear process caused by charge trapping and molecular diffusion in an inhomogeneous and porous dielectric material. A slow impedance change, caused by space charge polarization [8], [10], is

seen as an additional leakage current in the capacitive element formed with the dielectric layer, and is strongly influenced by the combination of temperature and humidity.

## 4.2 Mechanical requirements for the dielectric layer

The mechanical requirements vary depending on the intended application to be performed by the embedded carbon thin film sensor, but it is of importance that the mechanical performance of the steel substrate materials remains intact after the coating process. A process operating at a low enough operating temperature (preferably below 250 °C) is needed, which will not affect the hardness and tempering of the steel substrates during the deposition of the aluminium oxide dielectric layer for the embedded sensors.

When a sensor element is applied for temperature measurement, the tension caused by a thermal mismatch between the dielectric layer and the steel substrate is the major contributor to the adhesion between the dielectric layer and the substrate.

The bonding strength of the deposited dielectric layer to the steel substrate depends on the deposition technique used. The coating techniques with ionized plasmas form stronger chemical bonding compared to thermal spray deposition in which the adhesion is more mechanical in nature. The internal stress formed in vacuum plasma coated metal oxide layers is usually compressive, and in thermally deposited coatings it is tensile, both reducing adhesion. Rapid cooling during deposition will also increase the probability of crack formation or peeling in the deposited aluminium oxide layer [7].

Adherence of ionized plasma deposited dielectric coatings can be further promoted with prior etch cleaning with plasma and with the deposition of bond interlayers for adhesion enhancement [11]. Surface roughening of the substrate can also improve mechanical adhesion, but the method is applicable only with relatively thick coatings, such as thermal spray coatings capable of forming a conformal coating layer over rough surface topology.

During strain measurement, the dielectric layer must withstand tension without fracturing. The strain can be as high as the proof stress level of 0.2% in the steel substrate. Such a fracture toughness is exigently demanding for metal oxide ceramics. Cracks formed in the metal oxide insulating layer due to low fracture toughness can cause discontinuity and nonlinearity in the measured resistance value of the piezoresistive hard carbon film sensor.

The mean roughness depth ($R_z$) of substrate surfaces with thin film coatings should also be kept as low as possible to ensure conformality and dielectric strength of the deposited dielectric layers over the substrate. In practice, this means a need for polished metal surfaces having an $R_z$ value of not more than the coating thickness to ensure conformality and electrical shielding with thin films [6].

# 5 DIELECTRIC MATERIALS FOR ELECTRICAL INSULATION OF HARD CARBON THIN FILM SENSORS

The basic requirements for the dielectric layer in embedded hard carbon sensors are good adhesion to both the substrate material and to the carbon thin film, a relatively high elastic modulus to avoid mechanical damping during dynamic strain measurement, low surface roughness to ensure uniformity of the functional carbon layer as well as low porosity to minimize the effects caused by the space charge polarization of the dielectric layer in altered temperature and humidity. The application requirements in temperature or strain measurement determine the material selection of the electrical insulating layer, but this is strongly affected by the available deposition techniques and their economy. The most demanding aspect is to achieve the uniform and defect-free dielectric coating structure needed for electrical insulation, especially with thin films on rough substrate surfaces; equally critical is the adhesion of the dielectric layer. Fused silica is an example of a dielectric material which has excellent electrical insulation properties as a thin film, but the adhesion experienced with our study on PVD hard carbon thin films was poor.

Techniques considered for the study to produce electrically insulating layers for sensors on steel substrates consist of two major categories, either free-standing transferable layers or coating materials applicable for the electrical shielding.

Free-standing layers are most often plastic films or ceramic sheets glued or brazed onto the substrate. Polyimide films and aluminium oxide plates can be mentioned as common electrical insulating materials in this group. Their dielectric properties are good, but the limitation is most often the bonding strength of the adhesive material, which is greatly influenced by its thermal and chemical endurance during operational conditions. Free-standing layers are also bulky in size when considering use of an embedded sensor structure limited with tight tolerances. The technique is commonly used in preparing metal foil strain gauges on polyimide films.

Dielectric paints can be considered as the most common technique for applying electrically insulating layers of polymer or composite materials on conductive substrates. The electrical insulation of these materials is good, but the limiting factor of paints, such as epoxy or polyurethane, is that they cannot reach the maximum temperature range of up to 250 °C needed in some applications of embedded carbon sensors. The high thermal expansion and relatively low elastic modulus of these materials compared to ceramic materials additionally limit the use of these materials.

Sol–gel coatings for electrical insulation can be produced by spray, dip or spin deposition on metallic substrates using two basic techniques. The first technique consists of the dispersion of colloidal particles in a liquid to form a sol, which is then destabilized to further produce a gel form. The second technique involves a polymerization process by removing stabilizing organic components from organometallic compounds such as alkoxides to form a gel with a continuous network. The coatings usually have good adhesion on metallic substrates and good dielectric properties, but thermal sintering is needed to form a dense structure. Ceramic sol-gel coatings of silica-aluminium oxide have been reported to possess a dielectric strength of 17 MV/m with a thickness of 300 um, but the gel phase processing needs temperatures of 400 °C to 600 °C to pyrolyze the organic components from the coating, which limits the use of the coatings [12]. Based on our experience, without the high-temperature drying the sol-gel coatings tend to outgas during the PVD deposition of hard carbon thin films, causing cracking of the dielectric layer and sensor films.

Electrically insulating metal oxide coatings can be deposited on steel at atmospheric pressure by thermal spray, and at low pressure by physical vapour deposition (PVD), chemical vapour deposition (CVD) or atomic layer deposition (ALD). The benefit of the thermal spray and PVD techniques compared to CVD is the possibility for low-temperature deposition of aluminium oxide coatings compared to CVD [7], [13], [14]. Conformal aluminium oxide coatings can be deposited by ALD at a relatively low deposition temperature of below 500 °C [15]; however, ALD suffers from a relatively slow deposition rate and poor adhesion when an electrical insulating layer on steel substrates is concerned.

## 5.1 Thermal spray deposition of $Al_2O_3$ coatings

The three major categories in thermal spray techniques are flame spray, electric arc spray and plasma arc spray. The techniques are used as energy sources to heat the feedstock materials to molten or semi-molten state and to accelerate and propel them towards a prepared surface by either process gases or atomization jet [16]. Thermal spray is well-established and effective with a high deposition rate, an abundance of feedstock materials available for deposition and relatively inexpensive manufacturing of coatings. Thermal spray processes are non-atomistic, and the feedstock materials in the processes for metal oxide ceramics usually come in the form of powders with a 10–50 μm particle size [17].

Because of the high enthalpy in thermal spray processes, they possess high coating rates relative to other coating processes, such as chemical vapour or physical vapour deposition and electroplating. Thermal spray processes can also operate over a wide range of temperature, velocity and atmospheric conditions, which enables them to be applied to a broad variety of materials. Additional advantages of thermal spray processes include the ability to deposit thick coatings of 0.1–1 mm , and a small quantity of waste-disposal stream [18].

Thermal spray techniques form coatings without mixing the deposited layer into the substrate. They preserve the composition of the base material due to the very rapid cooling rates of the individual molten droplets that impact the cold substrate [18].

The temperature of the heat source in thermal spray is crucial for high-melting point ceramics which can be melted only by plasma spray based processes. The particle velocities of different spray processes have a direct impact on the properties of the coatings, such as adhesion on the substrate, density of the coating, and on mechanical hardness and corrosion resistance. The mechanical adhesion of the deposited layer is achieved by mechanical roughening of the substrate surface prior to thermal spraying, which is done typically by grit blasting [7].

The microstructure of a thermal spray coating is a complex mixture of splats formed from melted or semi-melted particles which have rapidly solidified to lamellae. The splats are disc-shaped, typically 50–200 μm in size and 0.5–5 μm in thickness. Rapid

quenching forms porous irregularities and cracks in the structure during the relaxation of stresses in the deposited layer with interlamellar and globular pores and intrasplat cracks in the coatings [19], [20]. The porosity in plasma-sprayed coatings can vary from 3% to 20% depending on the deposition parameters, which have a direct impact on both the mechanical and electrical properties of the coatings [21]. The lowest residual porosity in thermal spray coatings is deposited with high-velocity spray processes [7]. New liquid precursor-based suspension thermal spray techniques are emerging with the possibility to spray smaller ceramic particle sizes, from a few μm down to 0.01 μm in size, to reduce the coating thickness and porosity [22], [23], [24].

The focus in this review is on the two major thermal spray techniques applicable for the deposition of dielectric aluminium oxide $Al_2O_3$ coatings on steel substrates. These techniques are atmospheric plasma spray (APS) and high velocity oxygen fuel spraying (HVOF), which are both capable of melting aluminium oxide feedstock materials for the deposition of aluminium oxide coatings.

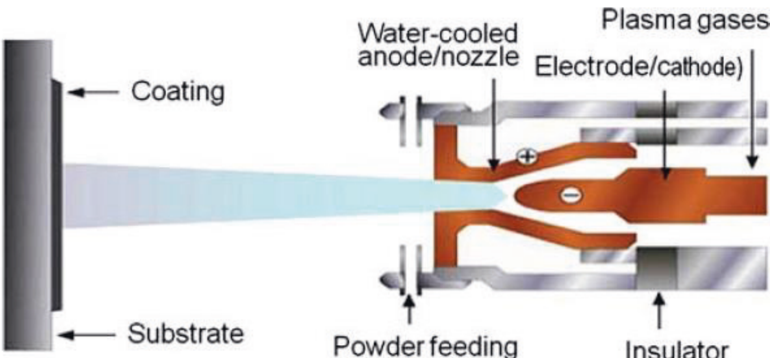


**Figure 2.** Schematic presentation of a plasma spray gun using DC power for plasma forming in APS [7].

In the APS process, shown above in Figure 2, the material for coating is added radially in powder form and is supplied by a carrier gas routed through the arc discharge between the anode and the cathode, generating the working plasma in the spray gun. The feedstock powder is melted in the arc zone as the hot carrier gas expands, pushing the melted particles at high velocity toward the substrate to be coated. The advantage of this technique is that, even though the plasma temperature

is high (between 10 000 °C and 20 000 °C), and can melt the aluminium oxide particles, the deposition can be controlled by interpass layers and distance to keep the substrate temperature moderately low, below 200 °C. The porosity of atmospheric plasma-sprayed coatings is relatively low, at 1–3% with optimal deposition parameters. Typical layer thicknesses are from 100 μm up to 2 mm [17].

The second technique, high velocity oxygen fuel spraying (HVOF), is a flame process in which the feedstock powder is transported through a fuel gas chamber, where the gas is forced to expand through a small de Laval nozzle to obtain very high particle velocities of up to 1000 m/s [17]. The powder particles are heated in the fuel and oxygen gas stream at a high combustion temperature and transferred towards the substrate with very high kinetic energies. The principle of the spray torch in HVOF spray gun is shown in Figure 3. The combination of ethylene burnt as the main fuel together with oxygen can generate torches with high combustion temperatures of up to 2924 °C [7]. The density and adhesion of the coating are improved by the increase of kinetic energy in the torch. The high kinetic energy of the torch shortens the dwell time in the gas stream, which lowers the particle temperature compared to plasma spray and reduces the degree of particle melting and oxidation. The high particle impact velocity in HVOF can deform particles which are not fully melted, and high coating density can be achieved at lower average particle temperatures. Heating also occurs through the particle impact, which converts kinetic energy to heat in the particles and further promotes the formation of dense coatings [18]. The combination of high particle velocity with moderate particle temperature results in dense coatings with porosities of 0.5–2% that adhere well to the substrate [17].

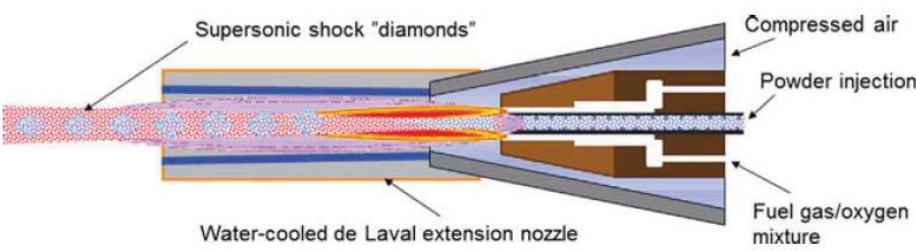


**Figure 3.** Schematic presentation of an HVOF spray torch [7].

## 5.2 Physical vapour deposition of $Al_2O_3$ coatings

Physical vapour deposition (PVD) covers a broad family of vacuum coating techniques in which the employed material is physically removed from the target or cathode by evaporation or sputtering into a vapour phase of atomic particles, which are transported by the energy of these neutral or ionic vapour particles. The transported particles condense into a solid phase as a deposit on the surfaces of appropriately placed substrates in a vacuum to form a coating [25], as shown in Figure 4.

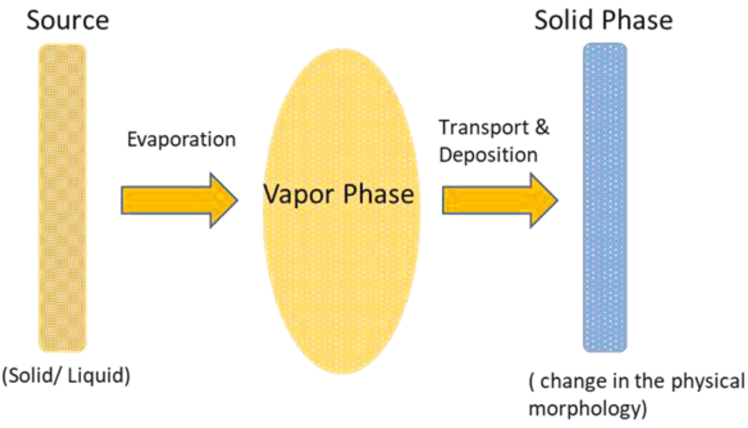


**Figure 4.** Principle of physical vapour deposition.

The most common PVD techniques for preparing metal oxide coatings are reactive magnetron sputtering and vacuum cathodic arc evaporation, shown in Figure 5. In the sputtering process, the target in solid or liquid form is bombarded by ions or kinetic particles energetic enough to evaporate the target material into the vapour phase. Reactive sputtering includes direct current (DC), radio frequency (RF) and medium frequency pulsed cathode magnetron sputtering (MF), or high-power pulsed magnetron sputtering (HiPIMS) techniques with ionized gas mixtures. The reactive vacuum cathodic arc can be operated by direct or pulsed current [26]. Laser ablation and laser assisted deposition are also emerging potential techniques offering possibility for low-temperature coating [27].

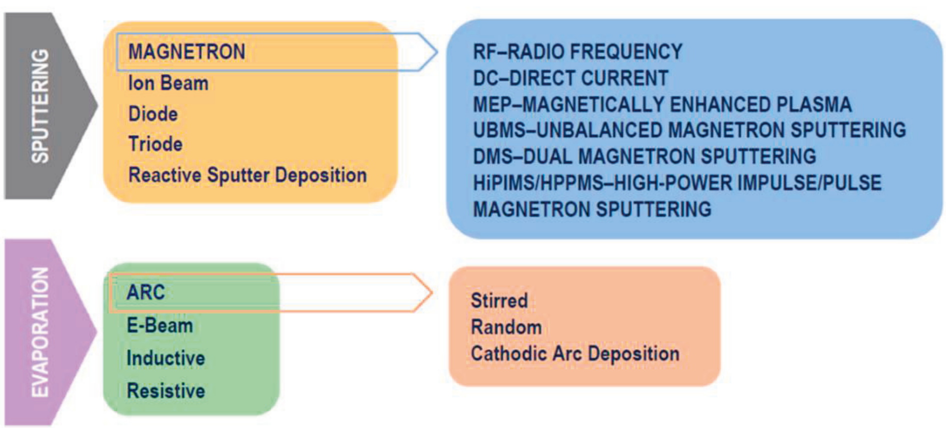


**Figure 5.** Physical vapour deposition techniques [26].

A magnetron is a versatile component to enhance the deposition rate in sputtering. It can be operated with all the powering options from direct current (DC) or medium frequency pulsed current (MF), radio frequency (RF) and high-power impulse current (HiPIMS) as alternatives. In the operation the carrier gas mostly argon, or argon/oxygen in the case of reactive sputtering, is ionized into a glow discharge at a low pressure level typically 0.1–10 Pa by a perpendicular electric field and magnetic field in the vicinity of the cathode surface. Electrons are trapped into helical trajectories along a horizontal magnetic field, enhancing the probability for ionization. The positive argon ions are accelerated towards the cathode potential of the target by the electric field to achieve a kinetic energy capable of sputtering off atoms from the target material [28]. The principle of a planar magnetron for PVD sputtering is depicted in Figure 6.

Magnetrons are operated with either a balanced or unbalanced magnetic field set-up. The latter type possess stronger outer magnets than inner magnets forming the shape of the magnetic field, allowing electrons to move from the electron trap into the plasma. The electrons moving away from the target will enhance ionizing collisions in the plasma towards the substrate being coated. The advantage of sputtering with unbalanced magnetrons is the possibility to use a bias on the substrate to form an effective secondary plasma in the vicinity of the substrate to be coated. Much denser plasma is produced around the substrate when gas ions from the secondary plasma accelerate towards the substrate in comparison to operation with balanced

magnetrons. Much higher ion bombardment is reached on the substrate, resulting in enhanced deposition of a thin film coating [28].

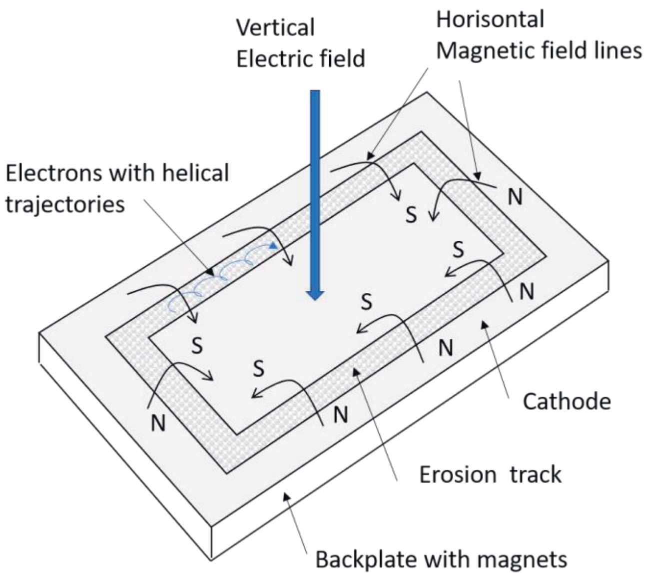


**Figure 6.** Principle of planar magnetron for PVD sputtering [29].

Aluminium oxide films are deposited in sputtering either using a similar source material $Al_2O_3$ target or metallic aluminium target and by introducing a reactive gas mixture containing oxygen to form aluminium oxide compounds on the substrate surface. The reactive sputtering techniques by direct current DC magnetron sputtering, pulsed magnetron sputtering, and RF sputtering of aluminium in an argon-oxygen plasma are nowadays the most common techniques for the manufacture of aluminium oxide coatings [30], [31], [32], [33], [34]. The aluminium oxide thin films manufactured by reactive sputtering are found in several tools, semiconductors and optical components. Reactive cathodic arc evaporation is also successfully applied to prepare aluminium oxide coatings, but it needs dedicated plasma filtering to reduce the defects caused by macroparticles emitted during arc evaporation to avoid formation of conductive clusters in the deposited film [35]. Aluminium oxide coatings prepared by electron beam evaporation have been reported to possess high leakage current and porosity [36].

Reactive sputtering of aluminium oxide is a rather complex process due to the hysteresis effect in the deposition [28]. At low oxygen flow, the operation is in metallic mode, as shown in Figure 7, and the deposited layer is not yet a pure compound, but rather a doped metal. The total pressure stays low if the metallic aluminium can receive the oxygen flow. When the oxygen flow is further increased, the operation moves to compound mode, in which the target surface starts to rapidly oxidize. At the time of a sudden drop in the discharge voltage and increase in the total pressure, the target surface is oxidized, causing a drop in the sputtering yield and deposition rate. At this point, the oxygen flow must be reduced to return to the metallic mode and initial deposition rate. The transient window where the operation stays constant for compound deposition depends on the target material and target size aa well as deposition conditions such as temperature and pressure, along with the pumping speed and control of oxygen flow. Depending on the sputtering technique and conditions, the width of the hysteresis window for the deposition can vary considerably.

Reactive sputtering of aluminium oxide films can be performed using several techniques, but the difficulty is in avoiding the build-up of an aluminium oxide layer causing arcing on the target, which affects the stability of the deposition process and can adversely cause defects in the growing aluminium oxide film. Reactive sputtering with a metal cathode has been studied the most as it enables high rate and controlled deposition with the use of DC power instead of RF power [37]. Suppression techniques have been developed to avoid arcing. Arc detection can be performed by current detection or voltage detection, or a combination. The fastest arc suppression techniques monitor the target voltage. When the target voltage drops below the trip level set for arc detection the suppression prevents the arc from occurring. Very fast detection is possible with detection times as short as 500 ns.

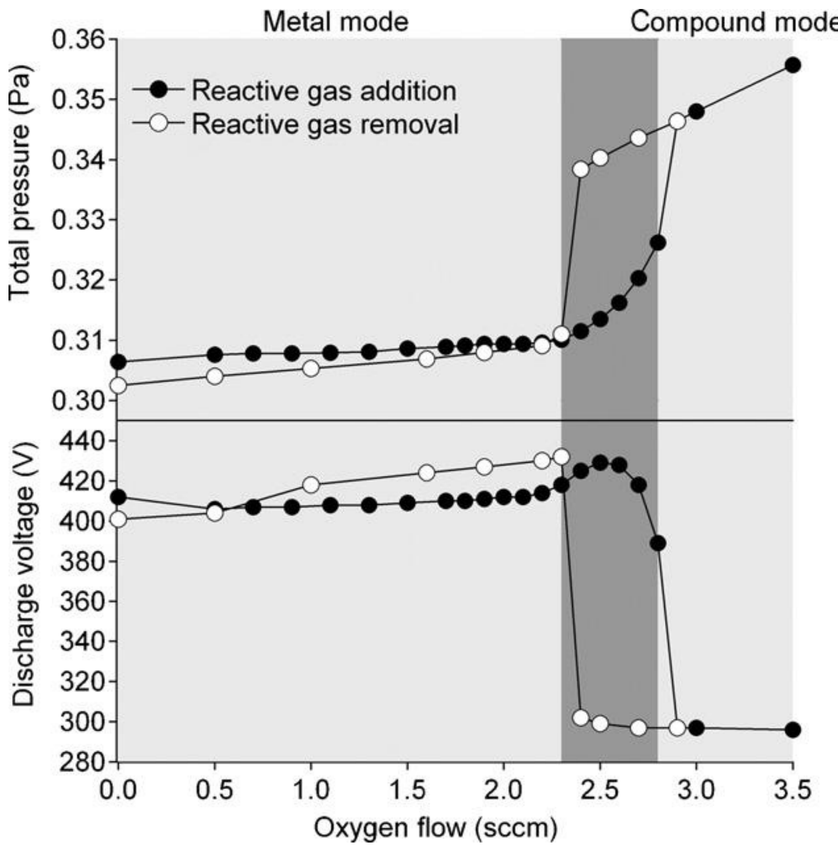


**Figure 7.** Discharge voltage and total pressure behaviour during reactive magnetron sputtering of Al in an $Ar/O_2$ mixture. The argon pressure and total current were kept constant at 0.3 Pa and 0.3 A [28].

DC sputtering has the highest deposition rate of the sputtering techniques, but it is limited with a relatively narrow process window in reactive sputtering between the metal and composition modes to avoid oxygen-caused target poisoning, as compared to pulsed MF or RF sputtering [30]. Reactive sputtering is a non-linear process in which the reactive gas flow influences both the deposition rate and pressure dramatically during sputter deposition at the points of change from metallic mode to reactive mode and back [38]. DC sputtering at low oxygen partial pressure results in non-stochiometric aluminium oxide having metallic aluminium in the film. An excess partial pressure level of oxygen causes a drop in the cathode voltage due to the beginning of aluminium oxide formation on the target, which decreases the sputtering rate, causes arcing on the target or even complete cessation of sputtering.

When the point of stoichiometric aluminium oxide is reached, any additional oxygen flow will cause an irreversible change in the discharge voltage and reduction in the deposition rate, as the excess oxygen begin to form an oxide layer on the cathode. The second issue is the formation of an aluminium oxide layer on the anode. This further reduces the current flow in sputtering, leading to additional arcing, and therefore to poor film quality and control of the process. The methods to prevent cathode and anode poisoning include saturation and feedback control of the reactive gas, increased pump speed, reactive gas pulsing and substrate/cathode distance separation [37], [38].

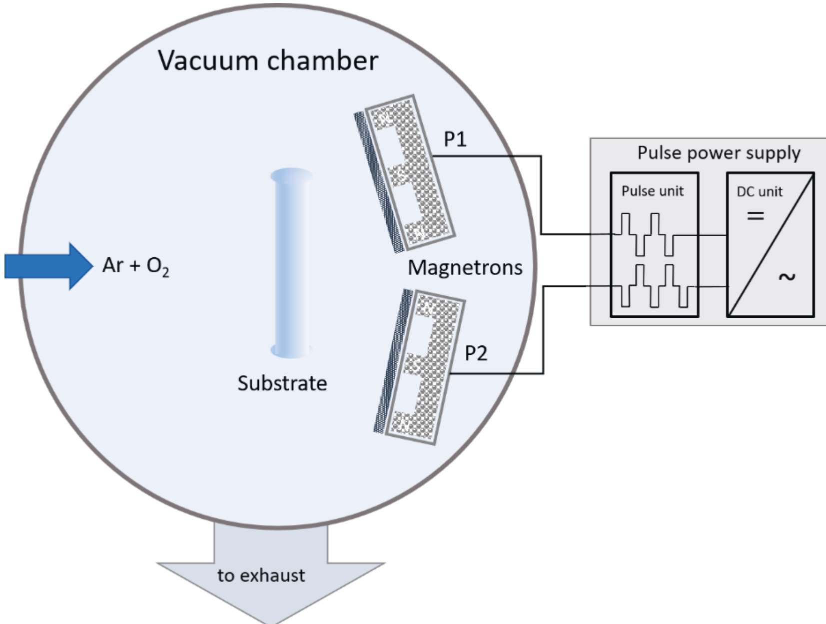


**Figure 8.** Schematic presentation of pulsed dual magnetron sputtering with bipolar operation.

Development of pulsed MF magnetron sputtering has significantly increased the viability of processing aluminium oxide coatings by preventing arcing on the target. Pulsed DC operation is performed as unipolar or bipolar sputtering, mostly with dual magnetrons. Both sputtering techniques achieve quite similar deposition rates, but bipolar sputtering is favoured if a higher substrate temperature and/or particle bombardment of the growing film are required [14], [39], [40]. Both magnetrons in bipolar dual magnetron sputtering operate alternately as cathode or anode, enabling stable arc-free operation during the long-term deposition of oxide layers [32]. A

schematic of reactive dual magnetron sputtering with bipolar pulsing is shown in Figure 8. The pulse power supply consists of a DC unit and a phase pulse unit which supplies pulsed current drive P1 and P2 for the two magnetrons with a 180-degree phase shift to alter the consecutive cathode/anode operation to prevent target poisoning.

MF sputtering has become the main method of thin film sputtering technologies in the deposition of dielectric or non-conducting thin film coatings. Pulsed DC operation at frequencies of 20–70 kHz (used most frequently at 40 kHz) is replacing RF sputtering. Its advantages are that there is no need for sophisticated and expensive power sources, and it can be used for large-scale deposition.

RF sputtering is a technique where argon atoms are accelerated in vacuum conditions by radio frequency in the range of 0.5 to 30 MHz (with 13.56 MHz the most common) to gain energy for sputtering by rapidly alternating the electrical potential, and to avoid charge build-up on the dielectric surfaces [37], [41], as shown in the schematic in Figure 9. At frequencies above 500 kHz electrons, due to their low mass electrons can respond instantaneously to a rapidly varying electric field between the target cathode and anode and shift up in energy, enhancing ionization in the plasma. Heavy ions do not possess high enough mobility to follow and their transit time to both electrodes is very much longer than the RF-period. Therefore, to maintain charge neutrality per cycle, both electrodes will become negatively charged. The electrodes hence form a capacitively coupled voltage divider on which the applied voltage between target and substrate (anode) is distributed as $V_{target}/V_{substrate} = (A_{substrate}/A_{target})^m$. For real deposition systems, the value of m is typically between 1.5 and 2, resulting in an average negative voltage bias at the substrate [28]. RF power supplies are designed to match impedance to a pure resistive 50 Ω load. For this purpose, a tunable matching network is needed in the system to reduce the complex capacitive and inductive reactance of the deposition process.

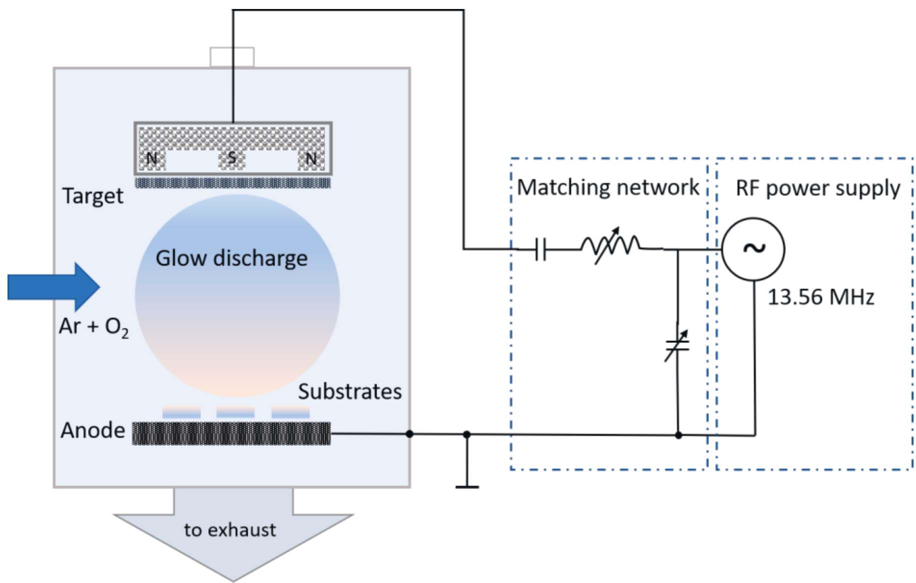


**Figure 9.** Schematic presentation of capacitively coupled RF sputtering.

The advantage of capacitively coupled RF sputtering is that it allows deposition of both dielectric materials such as metal oxide, and reactive sputtering of metals and reduces charge build-up on the target to prevent arc discharges caused by sparks. A second key advantage is the energy shift of electrons during radio frequency oscillation in the electric field, which enhances secondary ionization and plasma density when compared to DC sputtering. RF sputtering can also operate plasma discharge in the vacuum chamber at lower pressure levels from 0.1 to 2 Pa. Operation at lower pressure increases the mean free path of ions, improving the efficiency in the line-of-site deposition [41].

The main disadvantage in the use of RF power supplies is that radio waves require a much higher level of voltage for operation at the same deposition rate, which can cause overheating as a problem. In other word, RF power needs high voltage power supplies that are expensive and special electrical circuitry is required for impedance matching or arc suppression which can also cause additional problems in overheating [30].

HiPIMS is a relatively novel magnetron sputtering technology used for physical vapour deposition of thin film coatings with a high voltage power source in pulsed

operation between a voltage level of 1.3 and 1.5 kV and with pulse widths between 100 and 150 μs. It reaches target currents up to the level of 200 A with very high peak power density to several MW/pulse. Typical average operational power is 20 kW with pulse repetition frequencies up to 500 Hz [28] . The control of the pulsed high voltage in HiPIMS enhances the plasma stream by producing ionized atoms with much higher energy and plasma density, further increasing ionization of the atoms in the sputtered material.

The primary advantages in the films grown by HiPIMS are usually a dense coating structure, a high degree of crystallinity and a smoother surface than films grown by conventional DC or MF sputtering [42]. HiPIMS can produce coatings at lower critical pumping speed and at reduced hysteresis, which improves control of the operational point in reactive sputtering at a given partial pressure [43].

As a drawback in the compound mode, it suffers from arcing on the target material in the same way as DC sputtering. Arcing in HiPIMS can overheat the target, causing ejection of molten metallic microdroplets into the metal oxide coatings. This is especially a problem with lower melting point metals, such as aluminium [28].

## 5.3 $Al_2O_3$ as dielectric material for electrical insulation

Aluminium oxide, $Al_2O_3$, also called alumina, is nowadays the oxide ceramic most widely used in industrial applications. Aluminium oxide has a high melting point (2,040 °C) and high hardness (HV1.0 1500–2000). It possesses good thermal and chemical stability and electrical insulation characteristics. Aluminium oxide exhibits several different metastable crystal structures, but only one thermodynamically stable structure, $\alpha$-$Al_2O_3$ (corundum) in a close-packed hexagonal (cph) arrangement with aluminium ions in two-thirds of the octahedral sites [44].

The metastable $Al_2O_3$ structures are divided into categories of a face-centred cubic (fcc) or a hexagonal close-packed (hcp) arrangement of oxygen anions. The distribution of aluminium cations within each subgroup leads to different polymorphs. Aluminium oxide based on fcc packing of oxygen includes γ, η (cubic), θ (monoclinic) and δ (either tetragonal or orthorhombic) crystalline structures,

whereas the crystalline structures based on hcp packing are represented by the $\alpha$ (trigonal), $\varkappa$ (orthorhombic) and $\chi$ (hexagonal) phases. Together with the crystalline phases listed; aluminium oxide also exists in an amorphous phase. Table 1 shows the common processing routes of different metastable $Al_2O_3$ structures and the sequences of phase transformations in both subgroups (hcp and fcc) toward the stable $\alpha$-$Al_2O_3$ phase [45].

The high hardness, good thermal stability and corrosion resistance of $\alpha$-$Al_2O_3$ makes it superior in mechanical applications such as cutting tools, wear components, heat exchangers and engineering parts. The electrical insulating properties of aluminium oxide are utilized in semiconductor and electronic components.

**Table 1.** Common processing routes resulting in formation of different metastable $Al_2O_3$ structures and the sequences of phase transformations towards the stable $\alpha$-$Al_2O_3$ phase [45].

hcp

$$\alpha\text{-AlOOH (diaspore)} \xrightarrow{700^\circ\text{–}800^\circ\text{C}} \alpha\text{-Al}_2\text{O}_3$$

$$\gamma\text{-Al(OH)}_3\text{(gibbsite)} \xrightarrow{150^\circ\text{–}300^\circ\text{C}} \chi \xrightarrow{650^\circ\text{–}750^\circ\text{C}} \kappa \xrightarrow{1000^\circ\text{C}} \alpha\text{-Al}_2\text{O}_3$$

$$5\text{Al}_2\text{O}_3\cdot\text{H}_2\text{O (tohdite)} \xrightarrow{700^\circ\text{–}800^\circ\text{C}} \kappa' \xrightarrow{750^\circ\text{C}} \kappa \xrightarrow{900^\circ\text{C}} \alpha\text{-Al}_2\text{O}_3$$

$$\text{Vapor (CVD)} \rightarrow \kappa \rightarrow \alpha\text{-Al}_2\text{O}_3$$

fcc

$$\gamma\text{AlOOH (boehmite)} \xrightarrow{300^\circ\text{–}500^\circ\text{C}} \gamma \xrightarrow{700^\circ\text{–}800^\circ\text{C}} \delta \xrightarrow{900^\circ\text{–}1000^\circ\text{C}} \theta \xrightarrow{1000^\circ\text{–}1100^\circ\text{C}} \alpha\text{-Al}_2\text{O}_3$$

$$\alpha\text{-Al(OH)}_3\text{ (bayerite)} \xrightarrow{200^\circ\text{–}300^\circ\text{C}} \eta \xrightarrow{600^\circ\text{–}800^\circ\text{C}} \theta \xrightarrow{1000^\circ\text{–}1100^\circ\text{C}} \alpha\text{-Al}_2\text{O}_3$$

$$\text{Amorphous (anodic film)} \rightarrow \gamma \rightarrow \delta \rightarrow \theta \rightarrow \alpha\text{-Al}_2\text{O}_3$$

$$\text{Melt} \rightarrow \gamma \rightarrow \delta,\theta \rightarrow \alpha\text{-Al}_2\text{O}_3$$

Engineering aluminium oxide is classified as nine different grades from A1 to A9, in two different groups, determined by the purity and density of the alpha aluminium oxide. The first group, high-aluminium oxide engineering ceramics (grades A1-A4), possess a purity > 99% $\alpha$-$Al_2O_3$ and density > 3.75 g/cm$^3$, and the second group of engineering aluminium oxide grades (A5-A9) purity 80% $\leq$ $\alpha$-$Al_2O_3$ $\leq$ 99% [44].

The electrical properties of $\alpha$-$Al_2O_3$ make it interesting as a dielectric insulating layer material for embedded sensors. Depending on the purity of the aluminium oxide, the relative permittivity $\epsilon_r$ of sintered aluminium oxide is from 8 to 10 measured at 1 kHz, and it stays quite constant between 7.8 to 11 at a frequency of 1 MHz with low electrical dissipation between 0.00049 and 0.0013. Both factors, relative permittivity and the dissipation factor, are affected by temperature relatively little, and for many practical purposes an average value is considered sufficient [44]. This is the case with the embedded hard carbon thin film sensors in the determined temperature range from -10 ˚C to +100 ˚C.

### 5.3.1 Electrical properties of thermal spray deposited $Al_2O_3$ coatings

In thermal spray deposition, coatings are grown as lamellae which are formed by rapid solidification of the molten or semi-molten aluminium oxide droplets from individual aluminium oxide particles. The feedstock material used for the APS or HVOF deposition of aluminium oxide is typically from 5 μm to 50 μm sized $\alpha$-$Al_2O_3$ particles. The selection of the particle size and distribution of the feedstock material depends on the thermal spray process. The temperature necessary to melt the aluminium oxide particles, and the particle velocity to form a dense coating structure are the main parameters for modifying the coating microstructure [46].

The plasma temperature of the heat source in APS is typically around 12,000 °C with particle velocities from 200 to 400 m/s, which is well over the melting temperature of aluminium oxide. In HVOF the temperature of the heat source is typically around 3,000 °C with particle velocities from 600 to 800 m/s [7]. The low deposition temperature in HVOF is more critical in the deposition of aluminium oxide coatings, but this can be compensated by selecting a smaller particle size in the feedstock material. HVOF-sprayed aluminium oxide coatings have been reported to have a denser coating structure with improved hardness and roughness in comparison to APS-sprayed coatings [47], [48], [49].

Thermal spray coatings differ from bulk sintered aluminium oxide materials with a lamellar structure with limited interface bonding influenced by the interlamellar voids. The bonding ratio between adjacent lamellae dominates the properties of the

coatings [50]. The structure and properties of the coating depend on the thermal history that is highly influenced by the in-flight time of the particles when travelling from the spray torch to the surface of the substrate. This is affected by factors such as torch and substrate distance and the quantity of interpass layers [20].

Aluminium oxide, however, is strongly affected by the fabrication method which determines the phase structure of the deposited coatings. Rapid quenching of the molten feedstock material or plasma leads to metastable aluminium oxide polymorphs or amorphous coating structures [45], [51]. In thermal sprays, the γ-$Al_2O_3$ phase is described as the predominant phase found in the coatings [20], [52],. It is the very high cooling rate of the lamellae that hinders the formation of the stable rhombohedral α-$Al_2O_3$ phase, mainly found in embedded unmolten particles [53], [54], [55], [56]. Attempts to stabilize the α-phase in thermal spray with additives such as $TiO_2$ or $Cr_2O_3$ have shown a minor influence, but $TiO_2$ has been reported to improve the mechanical and tribological properties of $Al_2O_3$ coatings [52].

The degree of difference in the electrical performance of gamma and alpha aluminium oxide phases also depends on the density and morphology of the thermal spray coating. The aluminium oxide phases have very little difference in breakdown voltage. Dielectric breakdown often occurs due to defects in the coatings such as voids, pores and cracks [57], [47].

Characteristic of thermal spray coatings is the formation of pores and cracks of various sizes and morphologies which are generated during the deposition process and are entrapped in locations between the splats. The microstructure of ceramic coatings is strongly affected by these defects, such as globular pores, delamination or interlamellar pores and micro-cracks, all of which together form the porosity in the structure. Large globular pores are a consequence when contiguous splats and unmelted particles form incomplete contacts in the deposit [58]. The structure of thermally sprayed coating is depicted schematically in Figure 10 [7].

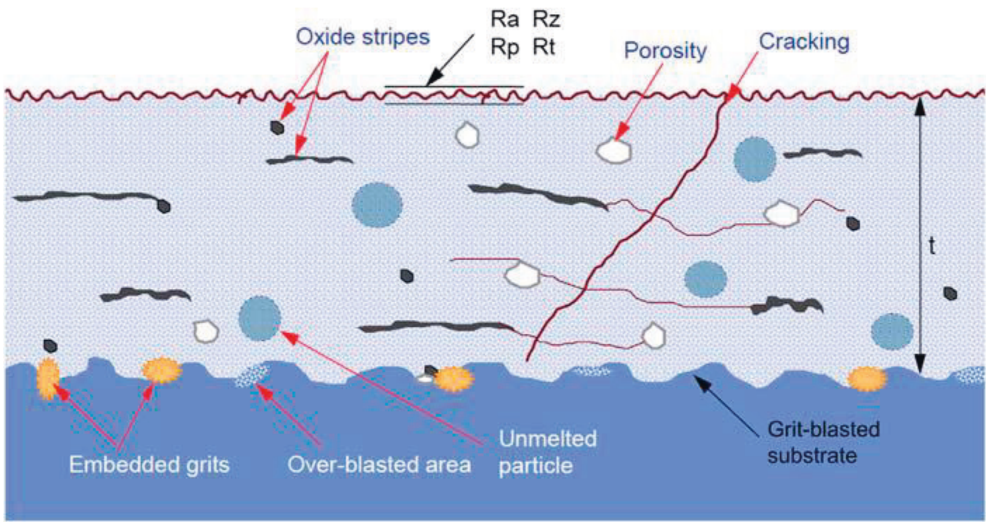


**Figure 10.** Schematic presentation of a thermally sprayed metallic coating structure [7].

The size of the pores in thermal spray coatings covers a large range from nanometre scale pores up to microscopical scale pores, existing between the grains of the ceramic. Large spherical pores which exist between the splats are often observed with coatings deposited with very hot plasma affected by the presence of gas in the molten material [48]. The large voids and vertical cracks may correspond to a lamellar thickness larger than 10 μm from the non-bonded interface area on the substrate [50].

Several factors are involved in the process of residual stress build-up in thermal spray coatings, of which the most relevant ones are related to the quenching and cooling stages. Quenching stress is a consequence of thermal contraction in a thermally sprayed splat when cooling from the solidification temperature to the overall system equilibrium temperature in the underlying solid, whereas cooling stresses are caused by the mismatch of the thermal expansion coefficients of the coating and the substrate. The residual stress of thermal spray coating is tensile in nature and typically of the order of 100 to 200 MPa [53].

As a pre-treatment procedure, metallic substrates are typically grit-blasted prior to deposition to ensure mechanical adhesion of the coating, but it has the drawback

that it may add compressive stress to the substrate and additional roughness to the deposited aluminium oxide layer within a thickness range below 200 μm.

#### 5.3.1.1 Resistivity of thermal spray $Al_2O_3$ coatings

The main factors determining the electrical resistivity of thermal spray deposited coatings include the feedstock material and the spray process together with the method itself [47]. Pawlowski [59] studied the dielectric properties of plasma-sprayed coatings prepared from nine different-sized commercial aluminium oxide feedstock powders. The granulometry of the feedstock α-$Al_2O_3$ particle size was varied from –23 μm + 4; 13 μm to –89 μm + 17; 41 μm and the chemical composition of the $Al_2O_3$ material from 96 wt.% to 99.2 wt.%. The resistivity of the 500 μm thick as-deposited coatings was reported in the range of $10^7$–$10^8$ Ωm, but after baking at 120 °C, the resistivity increased up to a level of $10^{11}$–$10^{12}$ Ωm. The coating porosity increased with the feedstock particle size used. The measured porosity was in the range of 5.5% to 8.5%. The porous coatings had low resistivity and suffered from absorbed water found in the voids of the feedstock material used [59]. This is a typically tendency of thermally sprayed aluminium oxide coatings due to the high γ-$Al_2O_3$ content. The gamma phase is known to be highly hygroscopic, causing changes in permittivity, such as an increase in the dielectric constant and loss factor [57]. The shrinkage is less in ceramic coatings than in metallic substrates. In the cooling phase of plats solidification can cause crack formation in the layer. The porosity found in the APS coatings was higher for coatings deposited from a feedstock powder of smaller grain size. The deposition rate was also lower, extending the spray time with fine feedstock powders to achieve the required coating thickness. Coatings deposited from fine powders also had a higher temperature and residual stress than those deposited from coarse powders.

Toma et al. [47] measured the DC resistance of 100 μm and 200 μm thick APS and HVOF aluminium oxide coatings. The alpha phase content was 21 vol.% in the HVOF coatings, whereas only 4 vol.% was found in the APS coatings. The samples were measured in 30% RH and 95% RH at room temperature, and at 200 °C.

The measured resistances in 30% RH at room temperature were similar for both 100 μm and 200 μm thick APS and HVOF coatings. APS coatings showed a resistance

of 2.70x$10^{11}$ Ω (for 100 μm) and 2.90x$10^{11}$ Ω (for 200 μm), and 1.13x$10^{11}$ Ω and 1.08x$10^{11}$ Ω for HVOF coatings, respectively. The resistance value at room temperature and 95% RH decreased significantly with APS to 4.4x$10^{4}$ Ω (for 100 μm) and 2.24x$10^{4}$ Ω (for 200 μm). For HVOF, it decreased to 3.76x$10^{5}$ Ω and 3.16x$10^{5}$ Ω, respectively. When heated up to 200 °C, the resistance values returned to a high level with both coatings, to a resistance 2.82x$10^{10}$ Ω (for 100 μm) and 2.18x$10^{10}$ Ω (for 200 μm) with APS, and to a resistance 8.03x$10^{10}$ Ω (for 100 μm) and 7.71x$10^{10}$ Ω (for 200 μm) with HVOF. The sensitivity of the HVOF coatings to humidity was less than that of the APS coatings. The resistivity of the coatings deposited with both processes decreased similarly, almost linearly with increased humidity. Open porosity was higher in the APS coatings than in the HVOF coatings. This was assumed to be the reason for the lower sensitivity to humidity found in the HVOF coatings.

Toma et al. [47] also performed dynamic vapour sorption (DVS) measurements at room temperature to determine and quantify the interaction between water vapour and the surface of the oxide ceramics from 0% RH to 95% RH. The measurements were performed both with feedstock powders and coatings. Mass changes during sorption or desorption cycles of vaporized water on solid surfaces can be determined by DVS. The method is also applicable for studying surface and bulk adsorption and desorption phenomena, and hydration or dehydration.

The hygroscopicity observed in thermal spray coatings was explained as surface adsorption of water that weakly interacts with the surface in physisorption by the effect of van der Waals forces or in chemisorption with stronger interaction. Physisorption can be inversed by reducing humidity or by raising temperature. Chemisorption is more permanent and considered irrevocable. Bulk absorption is a reversible process, but much slower than surface adsorption. Water is usually bonded deep inside the material structure in bulk absorption. The mechanism of water adsorption on a ceramic oxide surface is shown in Figure 11.

The benefits of HVOF thermal spraying over APS are the potential to deposit aluminium oxide coatings with improved density and smoothness as well as the ability to deposit thin layers [49]. These are beneficial in sensor applications, as

porosity and gamma phase in aluminium oxide both cause impedance drift in thermal sprayed coating, depending on temperature and humidity [47], [60].

**Figure 11.** The mechanism of water adsorption on a ceramic oxide surface: I. Chemisorption of water and formation of hydroxylated oxide surface; II. Physisorption of water; III. Dissociation of physisorbed water; and IV. Generation of protons responsible for $H^+$ ionic conduction [47].

Niittymäki et al. [61] measured the DC resistivity and permittivity of HVOF aluminium oxide coatings with a layer thickness of 250 μm deposited on stainless steel substrates. The measurement was performed in a climatic cabinet at 20 °C and 20% RH. Voltage on the deposited layer was adjusted between an electric field of 0.1 MV/m and 5 MV/m in the measurement. Resistivity was in the range of $10^{12}$ Ωm in the coating measured. A strong non-ohmic response was observed in the coating as a decrease in resistivity to $10^{11}$ Ωm at an electric field level of 5 MV/m. The influence of humidity on direct current resistivity was investigated with the coatings at 20 °C temperature in 90% RH, and an electric field of 2–4 MV/m. The reduction in resistivity observed in the high humidity conditions was of the order of $10^5$.

Toma et al. [24] measured resistivity of $Al_2O_3$ coatings deposited by suspension oxygen fuel thermal spray (S-HVOF) and HVOF from high purity $\alpha$-$Al_2O_3$ (> 99.99%) powders used as feedstock material. Both feedstock materials (suspension and powder) were sprayed with an HVOF TopGun using ethylene as the fuel. At low humidity levels (up to 40% RH) the electrical resistivity was on the order of $10^{11}$ $\Omega$m obtained for both S-HVOF and HVOF coatings. At a very high humidity (97% RH) the electrical resistivity values for the S-HVOF coatings were in the range $10^6$-$10^{11}$ $\Omega$m, up to five orders magnitude higher than those recorded for the HVOF coating of $10^6$ $\Omega$m. The better electrical stability of S-HVOF coatings in highly humid environments was explained by their specific microstructure with finer pores and lower interconnected porosity and by the retention of a high $\alpha$-$Al_2O_3$ content. However, after long-term exposure of S-HVOF coatings at 97% RH the electrical properties were also found to degrade significantly (by up to 4-5 orders of magnitude).

#### 5.3.1.2 Relative permittivity of thermal spray $Al_2O_3$ coatings

Thermal spray coatings possess relatively constant dielectric properties in conditions of low temperatures below 250 °C and low humidity. Pawlowski [59] measured the dielectric constant from plasma-sprayed coatings deposited from nine different feedstock powders. After baking the samples at 120 °C, the values of relative permittivity were in the range of 6–8, measured at 1 kHz. The high values of permittivity were measured with a high $\gamma$-$Al_2O_3$ content and porous coating structure. The loss tangent measured at 1kHz varied from 0.012 to 0.051. The density of the coatings was measured between 3.25 g/cm$^3$ and 3.45 g/cm$^3$, when the porosity of the coatings varied from 7.9% to 5.3%, respectively. The highest loss factor value was measured in the coatings with the highest porosity.

Niittymäki et al. [62] studied relative permittivity as a function of electric field of HVOF thermal spray coatings deposited from two aluminium oxide feedstock powders: powder material A with a particle size of 2–10 μm and powder material B with a particle size of 5–25 μm. The thicknesses measured from the images of the cross-section were 209 μm for the coating deposited from powder A and 288 μm for the coating deposited from powder B. The result indicated that the coatings made

from powder A produced coatings with a lower dielectric constant at 0.1 Hz than the coatings deposited from powder B with bigger particles. Both samples had a very similar relative permittivity and close to a value of 10 when measured at 100 Hz in the electric field strength range between 0.1 MV/m and 5.0 MV/m. The loss index of the aluminium oxide coating deposited from powder B measured at 0.1Hz indicated a clear increase at electric field values over 0.5 MV/m compared to the sample prepared from powder A. The explanation of lower permittivity observed in the sample deposited from powder A at 0.1 Hz was attributed to the small lamella size and amorphous volume in the structure.

Turunen et al. [63] studied 500 μm thick HVOF thermal spray aluminium oxide coatings by varying the build-up rate and thickness of the interpass layers of 7.6 μm, 22.6 μm, 9.7 μm, 12.4 μm and 11.9 μm per pass to produce different porosity structures. Porosity in HVOF coatings is mainly located at the boundaries of the interpass layers. The dielectric constant measured at 10 kHz showed variation between 5.9 and 8.2 in the coatings. A correlation between the number of interfaces and dielectric constant was observed. The dielectric constant was reduced by the growing number of interface boundaries in the coatings.

#### 5.3.1.3 Dielectric strength of thermal spray $Al_2O_3$ based coatings

Dielectric strength is an important measurement when defining the operating voltage range in a system. In a planar system the dielectric breakdown strength (DBS) is traditionally defined as voltage over the coating layer thickness before the breakthrough of current occurs.

Pawlowski [59] reported values of dielectric strength between 9 MV/m and 18 MV/m for plasma-sprayed aluminium oxide coatings prepared from nine different feedstock powders. In the comparison, they observed that coatings with lower porosity possessed higher dielectric strength. An increase in coating thickness caused a reduction in dielectric strength. This was also observed in coatings with low porosity. The increase in the number of structure defects, such as voids and cracks. Caused a reduction in dielectric strength.

Toma et al. [47] investigated the dielectric strength of APS- and HVOF-sprayed aluminium oxide coatings with layer thicknesses ranging from 100 µm to 240 µm. The average maximum value of the dielectric strength in the coatings was 34 MV/m, but thicker coatings indicated a decrease in the value. Dielectric strength measured on 120 µm thick HVOF aluminium oxide coating was 34 MV/m, and it decreased to 22 MV/m as the thickness increased to 220 µm. Toma et al. [24] measured also dielectric strength of S-HVOF coatings from high purity $\alpha$-$Al_2O_3$ (> 99.99%) powders used as feedstock material. The dielectric strength of suspension-sprayed coatings was found to be 19.5–26.8 MV/m for coating thicknesses ranging from 60 to 200 µm.

Kotlan et al. [64] analysed the effect of spray distance at 100 mm, 150 mm, and 200 mm on dielectric strength in APS aluminium oxide coatings. The dielectric strength of the coatings decreased when the spray distance was increased. At a distance of 100 mm the measured values for dielectric strength were 16.6 ± 1.8 MV/m.

Aluminium oxide coatings deposited on an aluminium substrate using the low pressure plasma spray technique (LPPS) have been reported to possess high density and low porosity of less than 1 vol.%. The 100 µm thick aluminium oxide coatings deposited with low pressure plasma spray (LPPS) can have a dielectric strength as high as 25–45 MV/m measured in an oil bath. The high dielectric strength of aluminium oxide coatings deposited by the LPPS technique is related to the coating structure produced with the process. The splat structure in the lamella of the coatings is formed of complex crystalline material in a dense amorphous matrix. Reproducible value in dielectric strength can be measured for LPPS coatings with a thickness of 20 µm or more. A similar decrease in dielectric strength was observed with LPPS coatings as seen in APS and HVOF coatings with an increase of coating thickness [65]

The gamma phase in a porous surface structure in a thermally sprayed coating increases sensitivity to moisture, which can cause impedance drift of the dielectric coating under humid conditions [24].

Aluminium oxide coatings of 500 um prepared by APS have been reported to have a dielectric breakdown strength of 16.6 ± 1.8 MV/m [64] , and also as high as 41.8

MV/m for high velocity oxygen fuel HVOF deposited coatings [66]. In comparison, for sintered high-aluminium oxide grades the AC dielectric breakdown strength is in the range of 10 to 15 MV/m (on a material thickness of 5 mm) [44]. The resistivity of sintered aluminium oxide varies between $10^{10}$ and $10^{12}$ Ωm and thermal conductivity from 14 to 30 W/(mK), both depending on the purity level of the sintered materials [67]. The dielectric breakdown of α-$Al_2O_3$ occurs by intrinsic electronic avalanche at lower temperatures, while at high temperatures, above 900–1000 ˚C, a steeper temperature dependence is observed which causes thermal breakdown to occur [44]

Kim et al. [68] studied dielectric properties and sealing impact before and after impregnation treatment on plasma-sprayed $Al_2O_3$–13%$TiO_2$ coatings with two commercial polymer sealants with the aim of improving the electrical insulation of the coatings. The studied samples consisted of a 5 mm low carbon steel substrate with a 100–120 μm thick bond coat of Ni-20.3Cr-13.6Mo-4.2Fe-2.9W on a 0.1–1 mm thick $Al_2O_3$–13%$TiO_2$ coating. The sealing materials were as follows, Metcoseal URS, a urethane-based sealant with a dielectric strength 10.0 MV/m and maximum service temperature up to 200 ºC, and Metcoseal ERS, an epoxy-based sealant with a dielectric strength of 17.6 MV/m and service temperature from -50 ºC to +150 ºC. The sealants were deposited both on as-sprayed and ground coating surfaces at room temperature after cooling the plasma spray deposited layer. The sealant materials were applied by brushing them on the samples and placing them into an oven for a chosen curing time. After the curing time, the samples were taken out to dry for 24 hours. Before testing the samples, they were ground to remove the sealant remaining on the surface. The penetration depth of the sealant was analysed by adding a small quantity of EpoDye fluorescent. DC puncture test apparatus according to ASTM standards was applied for testing the electrical insulation. Five points were tested from each coating sample (50 mm x 50 mm) using the step-by-step method. In the DC puncture test, voltage is increased until the dielectric breakdown voltage is reached at the point when leakage current in the sample is over 4 mA and the apparatus shuts off the power. The mechanism of dielectric breakdown mainly involved corona discharge with a partial thermal influence. A linear relation was observed with the increase of thickness to the decrease in dielectric strength with both as-sprayed and ground $Al_2O_3$–13%$TiO_2$ APS coatings. The average value of dielectric strength for the coatings in the thickness range was measured to be 20

MV/m. The improvement gained with Metcoseal URS in dielectric strength with the thicker coatings (> 300 μm) was not significant, but in the lower thickness range from 100 to 200 μm, the improvement was from 20 MV/m to 30 MV/m with the chosen curing parameters of 2 hours at 100 °C. The measured penetration depth of Metcoseal URS into the $Al_2O_3$–13%$TiO_2$ coating was approximately 70 μm. This was assumed to explain the insignificant improvement in dielectric strength with the thicker coatings. In the case of Metcoseal ERS, the improvement was significant: for coatings with a thickness of 200 μm the dielectric strength was improved to 35 MV/m. The measured penetration depth of Metcoseal ERS was about 250 μm. Metcoseal ERS also improved the bond strength from 50 kg/mm$^2$ to 400 kg/mm$^2$ for a coating thickness of 500 μm. It was also observed that both as-sprayed and ground samples possessed a very similar DBS, when considering the thickness loss in grinding.

### 5.3.2 Electrical properties of physical vapour deposited $Al_2O_3$ thin film coatings

Physical vapour deposition is a method to process materials on an atomic level, so it differs in many ways from thermal spray deposition. PVD coating in sputtering takes place in low pressure conditions, in a vacuum chamber typically at a pressure level of 0.1 to 10 Pa. The deposition rates achieved in reactive MF or RF sputtering of metal oxides coatings are much lower than those for APS or HVOF thermal spraying. This limits the practical maximum thickness of PVD coatings to the 10 μm level and sets specific requirements for the surface finish, such as polishing of the steel substrates. In PVD, particles ejected from the target during sputtering can collide with the gas atoms in the vacuum vessel before they enter the substrate. The same phenomenon occurs for ions; when entering the target they become neutralized and reflected, which is also true for ions which are formed at the target. Collisions cause changes in particle energy, in their momentum and direction, which has an influence on the structure and morphology of the forming coatings. The key parameters for this are the deposition pressure and substrate temperature, but the plasma parameters, level of ionization and kinetic energy of atoms during deposition are crucial in the formation of the film [26].

Sputtering forms denser films with less porosity in the film in comparison to thermal evaporation. In general, sputtering at low pressure is an energetic deposition process, and films tend to have high density, a relatively small grain size and compressive stress in the film. At higher pressure levels influenced by the thermalization of the plasma, films become more porous like thermally evaporated films and typically have tensile stress [69].

Physical vapour deposited coatings are also denser in comparison with thermally sprayed coatings, but voids and conductive dust particles in PVD films are more critical. Substrate anomalies, such as inclusions and grinding burrs, induce anomalies and roughness in the steel substrates, which can more easily cause electrical breakdown and current leakage in dielectric thin films due to their low thickness, typically between 1 μm and 10 μm.

#### 5.3.2.1 Growth and microstructure of sputter deposited $Al_2O_3$ thin films

Thornton [70], [71] described the growth mechanism of sputtered films with a structure zone model. In his study, about 25 μm thick coatings deposited from refractory metals and aluminium alloys were characterized. The coatings were deposited on glass and metal samples at two different geometries with post and hollow cathode sputtering techniques. Coatings were prepared at deposition rates between 1.7 nm/s and 3.3 nm/s. Surface topographies were investigated with fracture cross sections for coatings deposited at different argon pressures, substrate temperatures and conditions of plasma bombardment.

Thornton mapped the deposited microstructures into four zones as a function of substrate temperature in relation to the material's melting temperature and argon pressure, as presented in Figure 12. The model has proven to be useful to provide information on the influence of the deposition parameters on the microstructure of sputtered coatings. In zone 1, at an argon pressure of 0.13 Pa and when the substrate temperature is less than 0.1 of the melting temperature ($T/T_m<0.1$), the surface mobility of adatoms is low and the growth of the film is in the direction of the sputtered plasma flux into amorphous films and columnar structure with voids. The coatings have poor lateral strength and are porous. When the argon pressure is further increased, the adatom mobility is further reduced and the columnar growth

continues even at higher substrate temperatures, up to $T/T_m$ ratios of 0.3. Self-diffusion starts to grow in zone T at a low argon pressure level and a temperature ratio $T/T_m$ of between 0.1 and 0.3. The microstructure becomes more fibrous with sintering type coalescence of grain boundaries in the film growth. The lateral strength in the microstructure was improved in such coatings. In zone 2, as the temperature ratio further increases to 0.3–0.5, surface mobility and migration at the grain boundaries are further increased, enabling recrystallization of the coating. The growth of columnar grains throughout the thickness will occur as the surface recrystallization process forms faceted surface structures at a temperature ratio $T/T_m$ of 0.5–0.75. The tendency for a faceted structure is believed to be related to conditions of low energy deposition. In zone 3, when the temperature ratio $T/T_m$ becomes greater than 0.75, the grain tops in the microstructure become smoother and grooved boundaries are formed between the grains.

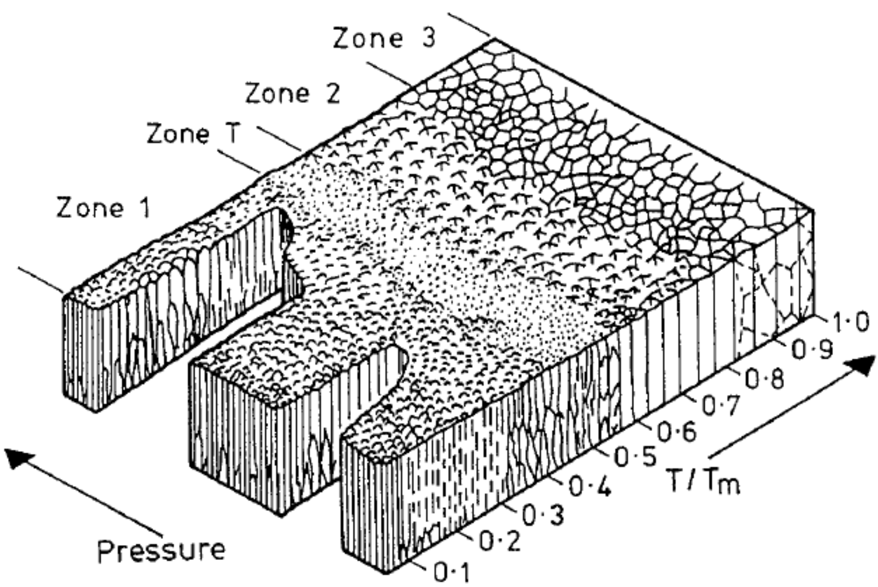


**Figure 12.** Thornton's zone diagram of film growth as a function of temperature $T/T_m$ and deposition pressure [70].

The influence of pressure on the coating structure causes the various zone features to appear at lower temperatures than the same zone at high pressure. In reactive

sputtering, the substrate temperature can be lower in cases where the depositing species in the plasma possess high kinetic energy to form a dense phase in the microstructure. The substrate temperature can be lowered when the flux of the depositing species can be controlled together with their kinetic energy.

In dual magnetron sputtered PVD films deposited at 550 °C, the aluminium oxide structure is referred to as pseudo $\gamma$-$Al_2O_3$, which is partly amorphous in structure [72]. The gamma phase is known to be highly hygroscopic in nature. Both factors, absorption and adsorption of moisture, will cause an increase of dielectric constant and loss factor in the coating [57].

Cremer et al. [30] investigated the microstructure of reactive magnetron sputtered aluminium oxide coatings deposited by the RF, DC and MF techniques in a temperature range from 100 °C to 600 °C. RF and DC sputtering were performed with a single magnetron and MF sputtering with two magnetrons in bipolar operation at 40 kHz by alternating the magnetrons in the plasma discharge as anode and cathode in sequence. The purpose of the study was to determine the growth parameters for crystalline aluminium oxide films which possess improved adhesion compared to amorphous films, and to investigate the effect of oxygen flow and substrate temperature on growth and the influence of the sputtering methods on the properties. The deposition parameters included a constant argon partial pressure of 0.35 Pa and substrate bias of -95 V. In reactive sputtering, the flow of oxygen was varied between 2 and 8 SCCM. The window for oxygen flow was chosen for each sputtering technique to avoid the deep drop in cathode voltage caused by target poisoning with aluminium oxide and reduction of the deposition rate during reactive sputtering.

The investigation by Cremer [30] showed that the process window in the deposition of crystalline aluminium oxide coatings was much narrower with DC sputtering than with MF or RF deposition.

The DC sputtered coatings deposited at a 2 SCCM flow rate also consisted of a mixture of aluminium and $\gamma$-$Al_2O_3$, and at a 3 SCCM flow rate, pure $\gamma$-$Al_2O_3$ was formed. Deposition at higher flow rates of 4 SCCM or above led to the formation of amorphous aluminium oxide. The films consisted of a structure with amorphous

powder formed at nucleation in the gas phase under sputtering conditions. The deposition rate in DC sputtering improved at first when the oxygen flow was increased to 3 SCCM, after which it started to decrease as the target became oxidized.

MF sputtering at 2 SCCM led to co-deposited layers of aluminium oxide with metallic aluminium. An increase of the oxygen flow rate to 3 SCCM resulted in the formation of pure γ-$Al_2O_3$ films. When the oxygen flow was further increased, crystallinity started to decrease.

In RF deposition at 525 °C with a 2 SCCM oxygen flow co-deposition of γ-$Al_2O_3$, a co-deposited, metallic aluminium was observed. Pure γ-$Al_2O_3$ was formed with RF as the oxygen flow was increased to 3 SCCM. When the flow rate was further increased, a significant decrease in crystallinity and deposition rate was observed. To find the effect of substrate temperature on crystallinity, RF sputtering was performed with 300 W power at 3 SCCM oxygen flow, and at substrate temperatures from 300 °C to 600 °C. Deposition at 300 °C resulted in the mixed formation of crystalline and amorphous aluminium oxide. When the substrate temperature was further increased to 450 °C, formation of pure crystalline γ-$Al_2O_3$ was observed. Crystallinity increased in the films when the substrate temperature was increased, but the process conditions did not lead to the formation of crystalline α-$Al_2O_3$ in the temperature range studied.

As general remarks on Cremer's [30] investigation, the deposition rate in DC sputtering was two times higher than in RF sputtering, even at half of the sputtering power. The deposition rate in MF sputtering was between these two. A decrease in both the deposition rate and crystallinity was observed at high oxygen flow rates. The effect was higher in DC and MF sputtering than in RF mode sputtering. None of the sputtering techniques led to the formation of crystalline α-$Al_2O_3$ with the chosen process parameters. The highest hardness of the aluminium oxide coatings was achieved with RF sputtering up to 25 GPa. The porosity of the coatings was not studied.

PVD aluminium oxide coatings are reported to be amorphous when deposited at low temperatures, whereas substrate temperatures above 400–500 °C lead to the formation of γ-$Al_2O_3$ [30], [32], [73] and to α-$Al_2O_3$ at substrate temperatures over

1000 °C. Amorphous layers deposited by PVD sputtering possess lower hardness than crystalline layers, but roughness and intrinsic compressive stress are typically higher in crystalline coatings. The high substrate temperature needed for the deposition of alpha phase aluminium oxide has limited the use of PVD deposition on steel substrates, especially in wear-resistant applications. The need for low temperature processing has created several new techniques to lower the substrate temperature required in deposition. The basic ideas behind these have been to increase plasma density and ionization to enhance reactive sputtering with pulsed operation together with substrate bias in the deposition to achieve crystallinity in the aluminium oxide phase [14], [32], [72], [73], [74], [75], [76], [77]. Enhancement in plasma ionization has also been achieved by feeding additional activation energy by RF coupling [78], [79], [80] and by increasing plasma density with high magnetic field confinement [13], [81]. Post-annealing of aluminium oxide films has also been tested in order to improve crystallinity [33], [82], [83]. Seed layers, such as $Cr_2O_3$ is one of the promising techniques is to guide the growth of crystalline aluminium oxide [84], [85]. The use of HiPIMS has also been studied to improve the microstructure and properties of coatings. The advantage of the HiPIMS process is increased ionization of the sputtered target species [34], [86].

Zywitzki et al. [32], [73] investigated reactively sputtered aluminium oxide coatings deposited by MF sputtering on X10CrAl24 steel substrates at substrate temperatures between 330 °C and 760 °C. MF sputtering consisted of a dual magnetron sputtering system (DMS) made up with two 500x1200 $mm^2$ planar targets connected to a bipolar pulse power. The discharge voltage of the targets was run with square wave shaped voltage pulses of 12 μm in length. The DMS was operated with a mean power of 16 kW. Substrates in the sputtering were kept at floating potential without bias voltage. The total pressure of the argon and oxygen mixture was kept at 0.1 Pa. Aluminium oxide coatings with a layer thickness between 4 μm and 6 μm were deposited at five different substrate temperatures of 330 °C, 480 °C, 560 °C, 690 °C and 760 °C. The microstructure of the aluminium oxide samples was investigated by XRD.

At a substrate temperature of 330 °C or less, the aluminium oxide layers were amorphous. Crystalline $\gamma$-$Al_2O_3$ was found at a substrate temperature of 480 °C. When the substrate temperature was further increased to 560 °C, textured $\gamma$-$Al_2O_3$

started to appear (zone T type films as described by Thornton [70]). With a further increase in temperature to 690°C and 760°C, textured γ-$Al_2O_3$ and α-$Al_2O_3$ mixtures started to form with 1 μm crystals in the microstructure.

The hardness measured in the amorphous films was 10 GPa, and it increased to 19 GPa in crystalline γ-$Al_2O_3$, and to 22 GPa in α-$Al_2O_3$. The crystalline films also possessed a high compressive stress, between 2 GPa and 9 GPa for γ-$Al_2O_3$, and between 12 GPa and 23 GPa for α-$Al_2O_3$, depending on the sputtering power used. It was observed that the substrate temperature and sputtering power had a major influence on the hardness and microstructure of the films.

Fiezke et al. [74] studied the reactive deposition of aluminium oxide with DMS in a similar way to Zywitzki. The targets were alternately operated as an anode or cathode at 50 kHz pulse frequency in the magnetron discharge. Pulse sequences of a few microseconds in length were used in the bipolar sputtering to prevent arcing and poisoning of the target with insulating aluminium oxide layers on the targets during the reactive sputtering. The operation point in the reactive DMS was set between the modes of metallic and reactive deposition in the transition range. The efficiency of plasma activation was improved typically by one order of magnitude with enhanced plasma density and ionization in DMS.

The 5 μm thick DMS aluminium oxide coatings deposited at 350 °C were amorphous, with the detection of a mixture of amorphous aluminium oxide and γ-$Al_2O_3$ at 450 °C, textured γ-$Al_2O_3$ at 550 °C, a mixture of γ-$Al_2O_3$ and α-$Al_2O_3$ at 650 °C and pure α-$Al_2O_3$ at 750 °C. The surface morphology of the coatings showed the lowest roughness on amorphous films of 25 nm. Roughness increased rapidly in a 60 nm thick mixture of amorphous and γ-$Al_2O_3$ film and reduced again in textured γ-$Al_2O_3$ of 30 nm. The full crystalline films showed the highest roughness in the 50:50 γ-$Al_2O_3$ and α-$Al_2O_3$ films of 70 nm, and in the pure α-$Al_2O_3$ of 85 nm. The hardness and crystallinity of the films increased with the deposition temperature. The amorphous films possessed a hardness of between 9 GPa and 10 GPa; in crystalline γ-$Al_2O_3$ it was 20GPa and in α-$Al_2O_3$ between 21 GPa and 22 GPa.

Schneider et al. [78], [79] studied the phase formation and mechanical properties of aluminium oxide coatings with ionized reactive sputtering (IMS). The coatings were

deposited onto 316 stainless steel films deposited on 100 silicon wafers. Power density was kept constant at 10 W/cm$^2$ on the magnetron targets. The 5 kW plasma generators in IMS were operated in a master-slave set-up with adjustable pulse frequency and duty cycle in the slave power supply set by the master power supply. The power supplies were operated at a pulse frequency of 150 kHz. Reactive sputtering of aluminium oxide was performed with IMS at a total pressure of 4 Pa in an argon mixture with 0.053 Pa partial pressure of oxygen. Films were grown in conventional sputtering, and in ionized sputtering mode with 1 kW inductively coupled RF power without bias voltage and with -70 V bias. The coatings were deposited by varying the ion current density and substrate temperature from 290 °C to 500 °C to study their effect on the microstructure of the films. The phase structure of the films was characterized by XRD. Films grown with conventional sputtering at an ion current density of 2.0 mA/cm$^2$ were amorphous. It was observed that the hardness of the films improved when the substrate temperature was increased, and bias voltage was used. Phase transformations were detected at lower substrate temperatures with higher ion currents, at densities more than 3.5 mA/cm$^2$. Metastable $\kappa$- and $\theta$-aluminium oxide phases were identified from films grown in ion current densities between 5.9 mA/cm$^2$ and 25.6 mA/cm$^2$, and at substrate temperature even as low as 430 °C. The films possessed a hardness of 22 $\pm$ 1 GPa. The $\alpha$-aluminium oxide phase was not detected in the films. It was also observed that at high ion flux densities, (> 7 mA/cm$^2$), the brittleness of the films was considerably increased.

Segda et al. [31] investigated RF magnetron sputtering with amorphous aluminium oxide thin films to optimize conditions for the growth of $Al_2O_3$ coatings. Coatings were sputtered with argon or an argon and oxygen mixture from a 100 mm aluminium oxide target (99.99%) with power densities of up to 6.37 W/cm$^2$.

Mirror polished stainless steel was used as substrate material in the study together with glass substrates for XRF characterization and carbon for RBS analysis. The aluminium oxide films were deposited at temperatures from 20 °C to 500 °C. The thickness of the coatings varied between 0.12 μm and 0.5 μm. The O:Al ratio was analysed from the films by RBS and XRF.

The sputtering rate was found to be in relation to the RF power used. The deposition rate of aluminium oxide changed from 0.11 μm to 0.79 μm/h when the RF power was increased from 125 W to 500 W, as other deposition parameters were kept the same, i.e. 1 Pa sputtering pressure in argon with a 2% $O_2$ mixture. The deposition rate reached maximum at an operating pressure of 0.5 Pa, and it started to decrease when the pressure was increased further.

Aluminium oxide coatings showed a denser and better quality when the deposition was started after evacuation at a pressure level of $2x10^{-4}$ Pa or lower compared to films when the deposition was started at a vacuum pressure of $10^{-3}$ Pa or higher. Coatings deposited at room temperature on glass substrates with an aluminium interlayer appeared to be denser and smoother, and of better quality without open porosity than those deposited onto heated substrates. SEM studies revealed that the microstructure of the coatings was columnar. The results for RF-sputtered aluminium oxide films on a heated stainless-steel substrate showed similar results in morphology, as reported by Vuoristo et al. [87]. RBS analysis of the aluminium oxide compositions of coatings deposited at a total pressure of 1 Pa with 2% and 5% oxygen addition showed respective O:Al ratios of $Al_2O_{3.40\pm0.03}$ and $Al_2O_{3.85\pm0.03}$ in the oxygen-rich films. Coatings deposited at a total pressure of 0.1 Pa with 2% oxygen addition were very close to the stoichiometric composition of aluminium oxide ($Al_2O_{3.01\pm0.03}$). An XRD study indicated that all the aluminium oxide films possessed an amorphous structure without crystallinity in the coating structure deposited at temperatures up to as much as 500 °C or when reheated after deposition. The density calculated for the RF magnetron sputtered films was $3.13 \pm 0.08$ g/cm$^3$.

Chiang et al. [88] investigated how the deposition parameters affected RF magnetron sputtering from aluminium targets to the microstructure of aluminium oxide deposited on copper substrates of 5x5 mm$^2$. Argon pressure was fixed at 1 Pa in the deposition, and the flow rate to 10 SCCM. RF power density was varied in three steps between 5 W/cm$^2$ and 15 W/cm$^2$, and the oxygen flow rate in four steps from 1 to 7 SCCM. When the deposition rate increased with increasing RF power it was observed that the oxygen content in the film decreased with increasing power density and oxygen flow rate, having a negative influence on the oxygen concentration in the films. This was explained by the fact that with a higher oxygen flow target, oxidation was also increased, which led to the formation of aluminium oxide on the

target, reducing the deposition rate. The ionization energy of oxygen molecules is also higher than that of argon atoms. The increase in oxygen flow rate at the same time will lower the argon partial pressure with the same total pressure, therefore decreasing the plasma density and level of ionization. The increase in neutral particles in the plasma will further lower the kinetic energy of the ions, as fewer ions possess sufficient energy to overcome the barrier to react with oxygen, and as a result will reduce the oxygen concentration in the film. The density of the coatings was improved with a lower oxygen flow of 3 SCCM and increase in RF power density from 5 $W/cm^2$ to 15 $W/cm^2$.

TEM measurements with a selected area diffraction pattern (SADP) indicated that the aluminium oxide films deposited at a power density 5$W/cm^2$ were amorphous, while diffraction rings were detected on films deposited at 15$W/cm^2$.

The crystallization at the increased RF power density was assumed to be caused by enhanced ionization which, under electron bombardment, can rearrange the particles on the depositing films. The films heated up under the bombardment, increasing the diffusivity of atoms in the surface and enhancing crystalline growth. As the oxygen flow rate was increased from 1 SCCM to 3 SCCM, crystallinity grew in the films, and it started to reduce at flow rates above 3 SCCM. When reaching maximum crystallinity in the films, different effects caused by oxygen flow were present. One of these was the formation of inclusions. Aluminium oxide films deposited at an oxygen flow of 3 SCCM had fewer inclusions than films deposited at 1 SCCM. In films which had an oxygen content close to stoichiometric aluminium oxide, nanocrystal formation was improved. An oxygen flow rate above 3 SCCM caused increased target poisoning and a reduction of plasma in the deposition. As a result of these effects, porosity grew in the microstructure and crystallinity was reduced in the aluminium oxide thin films.

Andersson et al. [84] studied the control of phase growth in aluminium oxide thin films to achieve α-A2O3 phase at a low deposition temperature of 500 °C. The aluminium oxide coatings were deposited on Si wafers in UHV conditions (base pressure $7\times10^{-7}$ Pa prior deposition) with reactive RF magnetron sputtering in an $Ar/O_2$ mixture at a constant RF power of 80 W. A 30 nm nucleation layer of $Cr_2O_3$ was deposited with pure argon at a pressure of 0.33 Pa and 300 °C substrate

temperature prior to deposition of the aluminium oxide coatings. All the aluminium oxide coatings were deposited at a constant 500 °C with substrates with floating bias. The total pressure of argon and oxygen mixture and the partial pressure of oxygen were the variables in the coating deposition runs. During sputtering, the partial pressures of $O_2$ and $H_2O$ were measured with a differentially pumped mass spectrometer. The crystalline phases in the aluminium oxide coatings were measured with grazing incidence X-ray diffraction (GIXRD) at an incident angle of 4°. The chemical composition of the coatings was measured by elastic recoil detection (ERDA) with a 35 MeV $Cl^{+7}$ ion beam at a 15° detection angle to the specimen surface. Measurement error in Al and O compositions was approximated to be ± 2 at.%.

The aluminium oxide depositions were investigated at two total pressure levels of 0.33 Pa and 0.67 Pa, and at four $O_2$ partial pressures between 7 mPa and 103 mPa. The increase in $O_2$ partial pressure from 7 mPa to 32 mPa at a total pressure of 0.33 Pa decreased the target voltage from -500 V to -300V. The change in reactive state of the target from metallic to oxidized reduced the deposition rate to less than one tenth. Hysteresis was not seen in the reactive sputtering with a combination of high 400 l/s pumping speed and small target size in the deposition. A phase change in the aluminium oxide grown at 0.33 Pa was observed in the GIXRD measurements when the $O_2$ partial pressure was increased from 7 mPa to 16 mPa. The respective change seen in the deposition rate was from 40% to 20% in reference to deposition in metallic mode. The coatings deposited at 7 mPa of oxygen correspond to $\gamma$-$Al_2O_3$. From the coatings deposited at an oxygen partial pressure of 16 mPa or more, the GIXRD diffraction pattern detected only $\alpha$-$Al_2O_3$ peaks. The phase change from $\gamma$-$Al_2O_3$ to $\alpha$-$Al_2O_3$ took place with a combination of low total pressure and sufficiently high partial pressure of oxygen without the need for bias voltage.

A study was also made of the influence of $10^{-4}$ Pa water background on the growth of the $\alpha$-$Al_2O_3$ films deposited at a total pressure of 0.33 Pa and with partial pressures of $O_2$ at 16 and 103 mPa. The GIXRD results of the films were like those for the films deposited in UHV conditions. The stoichiometry of the films was also close to aluminium oxide, and hydrogen (≤ 0.1 at. %) was not detected in the films by ERDA measurements.

The study demonstrated that the phase structure in aluminium oxide films can be influenced by controlling the kinetic energy of the sputtered species at low pressure deposition, and that low temperature growth of $\alpha$-$Al_2O_3$ is also possible with reactive sputtering.

At low temperature deposition, the effect of water becomes an important factor, being the main residual gas component at the base pressure level of the vacuum chamber. Wallin et al. [89] investigated the effects of residual water on the phase formation, composition and microstructure evolution of sputter-deposited aluminium oxide thin films. Depositions in the study were performed from the $Al_2O_3$ target (⌀ 50 mm and 99.99% purity) by RF magnetron sputtering in UHV conditions of base pressure below $3x10^{-6}$ Pa, and with 80 W constant power. The substrates were kept in floating potential during deposition. Substrate temperatures were kept at 500 °C during aluminium oxide deposition and at 300 °C during deposition of the nucleation $Cr_2O_3$ interlayers.

A surface profilometer was used to determine the thickness of the films. Conditions at different base pressure levels were simulated by adding deionized water into the vacuum chamber through a leak valve. A differentially pumped residual gas analyser (RGA) was used to determine the water content in the vacuum chamber. The microstructure of the films was studied by TEM, and the phase content by XRD. The elemental composition of the films was analysed by ERDA, and hydrogen content by Si-detector with an 18 μm Al range foil.

The deposition time for all samples was kept the same, at eight hours. Six different variants were deposited with combinations of partial pressure of $H_2O$ at UHV and at 1 mPa, total sputtering pressure at 0.33 Pa and 2 Pa with a 30 nm $Cr_2O_3$ layer and without. The large changes in the deposition conditions were observed to cause corresponding large changes in the deposition rate and film thicknesses.

To summarize, a 1 mPa partial pressure of $H_2O$ reduced the deposition rate to 20% level when compared to the deposition rate at the same total pressure level without $H_2O$ addition. It was also observed that the target voltage was also slightly lower at 1 mPa partial pressure of $H_2O$ than at UHV partial pressure of $H_2O$, which indicated changes in the target and discharge conditions. The measured hydrogen content with

all the coating films was low, below 1 at.%. The aluminium oxide films grown on a 30 nm chromia nucleation interlayer at UHV partial pressure of $H_2O$ and at a total pressure of 0.33 Pa consisted predominantly of the α-aluminium oxide phase. The low thickness of the films deposited at 1 mPa partial pressure of $H_2O$ and otherwise in the same conditions complicated the XRD measurement due to the low thickness, but peaks for both α- and γ-aluminium oxide were detected. The addition of 1 mPa water caused a change from pure α-aluminium oxide to a film containing a mixture of α and γ phases. In films deposited at 2 Pa total pressure or without a $Cr_2O_3$ interlayer only the metastable γ phase was formed, and in XRD measurements there was no correlation found between residual water and phase formation in the film. This was in line with the results of Schneider et al. [90] in their study of the effects of residual water on amorphous films. They observed that the films grown at the highest partial pressure of $H_2O$ contained crystalline γ-aluminium oxide and the films deposited at lower partial pressure were amorphous when deposition conditions were otherwise the same. Residual water at 1 mPa prevented the growth of columnar α-aluminium oxide and caused growth of a small-grained microstructure followed by a gradual increase of γ-aluminium oxide in the content. When considering the large effect caused by water at 1 mPa background pressure in the phase content, it was concluded that the critical upper limit for water background pressure is between $10^{-4}$ Pa and $10^{-3}$ Pa, under which growth of the pure α-$Al_2O_3$ exists.

Lin et al. [86] studied the deposition of aluminium oxide coatings deposited in reactive deep oscillation magnetron sputtering (DOMS) mode by HiPIMS. In DOMS, the micro pulses are generated with high oscillation inside 966 µs modulation pulses. Each modulation pulse consists of 23 oscillatory micro pulses with an on and off time of 2 µs and 40 µs in the pulse train. An evaluation of the process stability was performed by measuring the micro arc counts at the target with different on and off time combinations in the micro pulses. Practically arc-free depositions were achieved at the 130 A peak target current with combinations of a short on time ($< 4$ µs) and long off time ($> 40$ µs). Control of reactive sputtering was achieved using a remote penning plasma emission monitoring sensor which controlled the oxygen partial pressure in the deposition.

The influence of different oxygen partial pressures in the transition region on the deposition rate, microstructure, optical and mechanical properties of the aluminium oxide coatings were the main subjects of the study. Coatings were deposited at a total pressure of between 0.29 Pa and 0.31 Pa with a constant argon flow of 80 SCCM, and at substrate temperatures from 250 °C to 300 °C. Substrates were in floating bias mode in the deposition runs.

The deposition rate in metallic mode sputtering with pure argon was about 9 µm/h with 1 kW power on the target. The films exhibited a dense structure, and no columnar grain growth was detected by SEM. The deposition rate measured in reactive sputtering was 0.25 µm/h in fully poisoned mode with an oxygen flow of 30 SCCM, and with 1 kW power on the target. The morphology of the aluminium oxide film showed a dense, glassy-like film microstructure. The deposition rate was improved by adjusting the closed loop control with a partial pressure of oxygen around 14.3 mPa in the transition region. All the coatings deposited in the transition region at low temperature were stoichiometric aluminium oxide and amorphous in microstructure. The amorphous aluminium oxide coatings possessed high hardness of between 14 GPa and 15 GPa and optical transparency in visible light.

#### 5.3.2.2 Resistivity of sputter deposited $Al_2O_3$ thin films

Mäntylä et al. [91] investigated the dielectric insulation and thermal stability in 5 µm thick RF-sputtered aluminium oxide coatings on an oxygen-free high conductive copper (OFHC) substrate. The coatings were deposited from high purity aluminium oxide (99.99 %) at a deposition rate of 0.33 µm/h, and a power density of 7.9 $W/cm^2$ power on a 100 mm target. The depositions were performed at a substrate temperature of 477 ± 25 °C, and at an argon pressure of 0.13Pa. The microstructure of the films was studied with by SEM (Jeol JSM-U3) and XRD (Jeol JDX-7X). The open porosity of the coatings was studied by electrochemical polarization with $H_2SO_4$ solution. The measurements revealed that the coatings were not fully electrically insulating in the solution. The DC resistivity of the films was $10^{13}$ Ωm, measured at room temperature with the accuracy of the measurement range. At an elevated temperature of 550 °C, the resistivity decreased to $10^9$ Ωm.

Vuoristo et al. [92], [87] studied the microstructure and electrical insulation of amorphous $Al_2O_3$ coatings deposited on copper substrate. In the sputtering conditions, the influence of substrate temperature and pressure with sputtering gas composition and type of discharge was investigated. The aluminium oxide coatings were deposited from a high purity aluminium oxide target (99.99 %) by RF magnetron sputtering, and a from pure aluminium target (99.5 %) by reactive DC magnetron sputtering with the target oxidized in compound mode. Prior to deposition at 500 °C substrate temperature and in an argon pressure of 0.67 Pa, the samples were etched with argon for 10 min at 3.3 Pa and -700 V bias, followed by DC sputtering of a titanium or chromium interlayer from 1 μm to 2 μm. The deposition of $Al_2O_3$ layer was started at first with a metallic aluminium bond layer. Without any bond layer, the $Al_2O_3$ had poor adhesion on the copper substrate. The structural and composition studies were carried out by SEM using a Phillips SEM 515, by XRD on a Siemens Diffrac 500, and by RBS with 1–2 MeV helium ions on a 2.5 MV van de Graaff accelerator. The density of the aluminium oxide coatings was determined from the thickness, surface area and weight gain of the aluminium oxide layer.

The deposition rate in RF magnetron sputtering from the aluminium oxide target varied from 1.6 μm/h to 4.6 μm/h when the argon pressure was increased from 0.4 Pa to 2 Pa. The explanation for the increase in the deposition rate was the increase of ionization and thermalization in the plasma at higher argon pressures, leading to the formation of coatings of a less dense structure at the highest sputtering pressures. Structurally, the densest coatings were obtained when sputtering was performed in reactive sputtering with oxygen onto unheated substrates or sputtering at low pressures.

The stoichiometry of the aluminium oxide coatings was observed to be strongly influenced by the sputtering technique and parameters used. Coatings deposited with RF sputtering with pure argon were deficient in oxygen content (O:Al ratio of 1.35). It was observed that heating of the substrate reduced the oxygen deficiency with increased chemical activity in the growing film (O:Al ratio of 1.42). Adding oxygen as a partial pressure resulted in coatings with the correct compound stoichiometry (O:Al ratio between 1.47–1.51) when deposited from the $Al_2O_3$ target. Reactive

magnetron sputtering of the aluminium target in DC or RF discharges produced aluminium oxide coatings with an excess of oxygen (O:Al ratio between 1.8–1.9).

The resistivity of aluminium oxide samples was measured between room temperature and 600 ºC. However, the value for resistivity could not be measured reliably with the gold contact electrodes deposited by RF sputtering on thin aluminium oxide films of 2–4 μm due to shorts circuits often found in the films. Therefore, separate gold contacts were used for measuring the resistivity of the aluminium oxide coatings. The resistivity at room temperature was in the range of $10^{14}$ Ωm measured in films of 3 μm, and it remained relatively high, on the level of about $2x10^{13}$ Ωm, up to 250 °C. Thicker aluminium oxide coatings of 23 μm with RF-puttered gold contact indicated a nonlinear change in resistivity with temperature. In the first heating cycle, the resistivity remained relatively stable, and at room temperature it was about $10^{11}$ Ωm. When the temperature was increased, resistivity decreased to $10^{10}$ Ωm at 100 ºC, after which it started to increase again to $6x10^{11}$ Ωm at 300 ºC. At higher temperatures, resistivity started to decrease again and was measured to be $10^{7}$ Ωm at 600 ºC. When heated for the second time, resistivity measured at room temperature was about $10^{13}$ Ωm, with a linear decrease in resistivity being observed over the whole temperature range. Such behaviour was assumed to be caused by the moisture in the film.

#### 5.3.2.3 Relative permittivity of sputter deposited $Al_2O_3$ thin films

Segda et al. [31] also studied the electrical properties of RF magnetron sputtered aluminium oxide films for use as a dielectric layer for capacitors. The tan δ loss factor measured at 1 kHz decreased as the O:Al ratio was increased. It was observed that tan δ goes through a minimum of $0.3x10^{-2}$ at the point where the ratio is between $1.6 < O:Al < 1.8$ for 0.15 μm aluminium oxide films. The dielectric constant showed that RF-sputtered aluminium oxide films, measured by RBS, were relatively insensitive to changes in stoichiometry, whereas for and $Al_2O_{3.02}$ film, the relative permittivity $\varepsilon_r$ was 8.5 ± 0.2, and for $Al_2O_{3.30}$ film $\varepsilon_r$ was 8.45 ± 0.2.

#### 5.3.2.4 Dielectric strength of sputter deposited $Al_2O_3$ thin films

In Mäntylä's study [91] dielectric strength of 5 µm thick RF-sputtered aluminium oxide coatings varied between 50 MV/m and 200 MV/m with a relatively large scatter between the results measured at room temperature in open air. The deposition of gold counter electrodes of 38.5 $mm^2$ in size revealed defects in the films which caused short circuits in several samples. A fibrous but dense microstructure was observed on the coatings in SEM studies, like zone T described in Thornton's structure zone model [70]. XRD studies revealed the amorphous structure of the coatings. The coatings did not show detectable changes in the microstructure after ten times repeated heating of the samples from room temperature to 600 ºC. Good adherence of the aluminium oxide layer to the substrate during the thermal cycling was preserved with the use of titanium and chromium interlayers. Spalling of the aluminium oxide coating was observed without interlayers.

The dielectric strength measured by Vuoristo [92] for the non-reactive RF magnetron sputtered aluminium oxide coatings of 8.7 µm was about 40 MV/m and relatively unchanged up to a temperature range of 400–500 ºC. The dielectric strength decreased at 600 °C but was still in the range of 10 MV/m. Reactively RF-sputtered coatings of 3.8 µm showed similar dielectric strength up to 400 °C and for DC sputtered coatings of 2.5 µm, it was half of the value measured with the RF-sputtered coatings.

Segda in his study [31] reported that the dielectric breakdown strength of RF magnetron sputtered aluminium oxide films of 0.15 µm reached its maximum value of 300 MV/m at the point where the ratio of oxygen and aluminium is between $1.6 < O:Al < 1.8$. Breakdown strength varied strongly depending on temperature, and it was approximately half of the value at 200 ºC of the room temperature value measured for films of 0.5 µm.

Carreri et.al. [77] studied aluminium oxide films deposited with bipolar reactive sputtering. The concept consisted of an AC power supply with fast arc handling and limited current output for investigation. The average AC power used in the sputtering system was 4–6 kW at a fixed 38.5 kHz repetition rate of 500 V bipolar

pulsing with a pulse length of 12.7 μm. The aluminium oxide films were deposited using large area, double rotatable cathodes (h=500mm, d= 150 mm). Sputtering was performed at a constant 1 Pa pressure in 200 SCCM argon flow with adjustable oxygen flow up to 35 SCCM. The substrate temperature was between 77 °C and 150 ºC during deposition (depending on the power used between 4 kW and 6 kW).

The substrate materials used in the study were glass, silicon and stainless steel. The relation of deposition rate to power and plasma emission intensity in the deposition was measured. The deposition rate was the highest for processes operating with high plasma emission intensity (PEI) close to the metallic mode. The highest measured deposition rate was 3.8 μm/h at 6 kW power and 40% PEI. The dielectric breakdown strength was highest for the films with 30% PEI. Films around 2–3 μm reached values of 1500 MV/m in the best samples (30% PEI at 5 kW power). Transparent and stoichiometric films with a chemical composition of aluminium oxide were obtained in deposition in a high oxygen flow and at 20% PEI. Still transparent but sub-stoichiometric films were obtained at 30% PEI. Coatings became under-stoichiometric and very dark at 40% PEI due to the concentration of metal in the film structure. Other factors, such as defect density, started to be considered as more important for the insulating property when it was detected that the under-stoichiometric films possessed better electrical insulation than the stoichiometric films. The microstructure and morphology of the films produced at different PEI were studied by SEM. Arcing was found to be highest in deposition at 20% PEI and lowest at 30% PEI. The arc counts increased in relation to a fixed PEI when the average power was increased. Deposition conditions with the lowest arcing led to the best microstructures, which possessed low defect densities and good insulation.

## 5.4 Summary of dielectric coatings applicable for electrical insulation of hard carbon sensors

Aluminium oxide is among the most employed ceramics in the coating industry since it exhibits good dielectric properties, high hardness, and high melting point, while still being cost-effective. Consequently, it is also a commonly used ceramic material for thermal spray coating solutions, where the main applications are electrical insulation and wear protection.

APS is the most important industrial spray process to manufacture aluminium oxide coatings, but HVOF is also used. This is why these two techniques were chosen for the study of aluminium oxide coatings for electrical insulation of hard carbon thin film sensors.

For the study APS $Al_2O_3$-30%MgO and $Al_2O_3$-3%$TiO_2$ coatings were chosen as reference in comparision with APS and HVOF $Al_2O_3$ coatings and S-HVOF $Al_2O_3$ coatings were chosen in comparison with HVOF coatings. The coatings were prepared from as state of art commercial feedstock materials by the suppliers.

The literature review in 5.3.1 showed that the resistivity requirement of $10^8$ Ωm over a temperature range of -10 °C to +100 °C under ambient air conditions of 20% RH is fulfilled with both APS and HVOF aluminium oxide coatings, but at high humidity conditions resistivity can drop as low as $10^5$–$10^6$ Ωm. Both APS and HVOF aluminium oxide coatings also fulfil the requirement in the thickness range of 40–200 μm for the breakdown voltage of the insulating layer of up to 200 VDC.

The selection of the technique either thermal spray or PVD depends on the application. PVD thin films are chosen for the applications with tight tolerances such as tribological contacts or with temperature sensitive materials.

One of the critical factors with APS and HVOF may become with low enough deposition temperature (preferably below 250 °C) needed with some steel substrates without affecting the hardness and tempering.

From the PVD techniques, RF sputtering of aluminium oxide was chosen to the study for two reasons. First, it has a wide process window for reactive sputtering of aluminium oxide and second, the deposition can be done at low temperature. As a drawback RF sputtering has a low deposition rate.

The literature review in 5.3.2 showed that the microstructure of RF-sputtered aluminium oxide is amorphous when deposited at temperatures below 250 °C. The resistivity of the films fulfils the requirement of $10^8$ Ωm over a temperature range of -10 °C to +100 °C under ambient air conditions of 20% RH. More critical is the dielectric breakdown strength (DBS) around 40 MV/m reported for RF-sputtered films. This sets the minimum thickness requirement of 5 μm for the coatings when operated at voltage level up to 200 VDC.

# 6 MATERIALS AND METHODS

The following chapter provides information of the substrate and coating materials used in the study, the sample preparation procedures, test equipment, and the characterization methods employed to study the APS, HVOF and S-HVOF aluminium oxide coatings and APS aluminium oxide-based coatings.

## 6.1 Substrate materials for $Al_2O_3$ coatings

The thermal spray coatings were deposited on cantilever steel beams made of low alloyed structural steel 1.0038 S235JR–EN10162 with a cold rolled surface finish ($R_z$~7.0μm). Figure 13 shows the dimensions of the steel plate (150x20x2 $mm^3$) and the aluminium oxide coating area (30x20 $mm^2$) on it. The deposited contact electrode of Ti6Al4V (10x10 $mm^2$) with a nominal thickness of 250 nm can be seen on top and in the centre of the aluminium oxide layer.

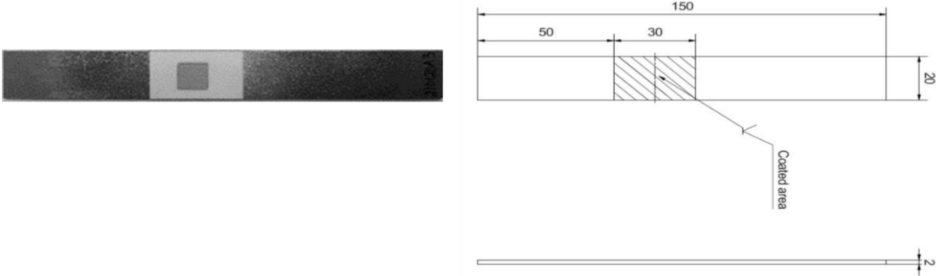


**Figure 13.** Cantilever beam of S235JR deposited with a thermal spray aluminium oxide layer (30x20 $mm^2$) and a test electrode of Ti6Al4V (10x10$mm^2$) on top of the layer.

The RF-sputtered aluminium oxide coatings were deposited on THYRODUR 2842 – 90MnCrV8 tool steel substrate discs (Ø22mm x 5.6 mm) having been surface polished to $R_a$ max. 0.05 μm, as shown in Figure 14. The square patterned contact electrode layer formed of 1x1 $mm^2$, and 3x3 $mm^2$ contact pads with a nominal coating thickness of 100nm deposited on RF-sputtered aluminium oxide coatings of

90MnCrV8 disks. The patterned Ti6Al4V contact matrix on the samples was used for testing the defect density of the pads with a short circuit.

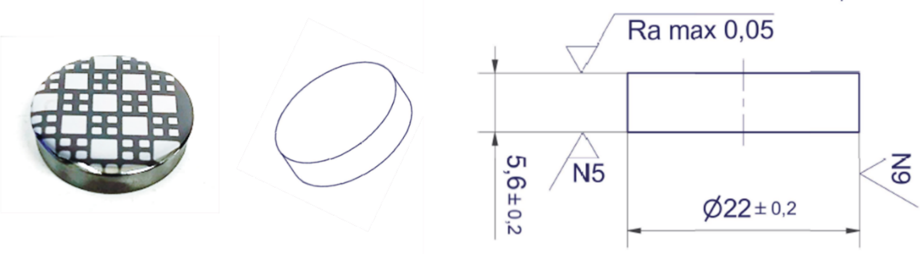


**Figure 14.** Test disc of THYRODUR 2842 – 90MnCrV8. With PVD aluminium oxide coating and patterned Ti6Al4V contact pad layer deposited on the disc on the left.

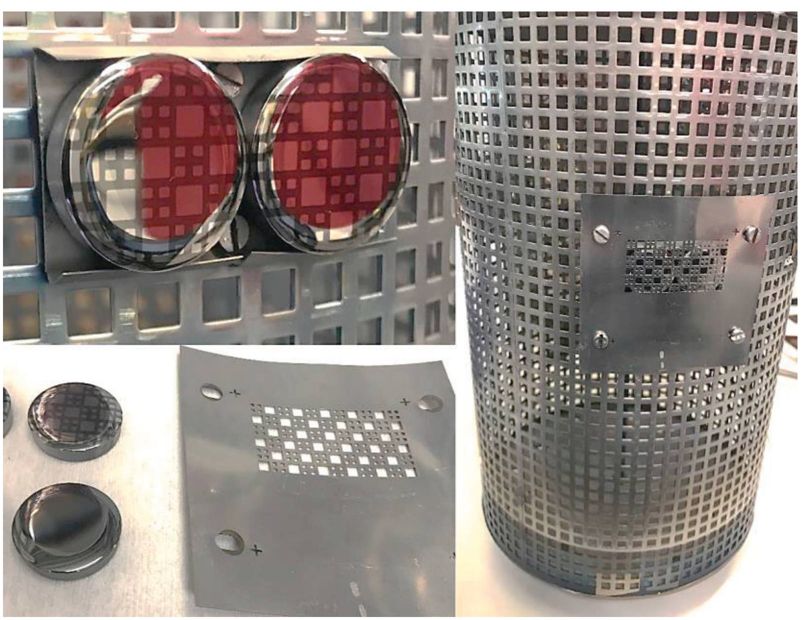

**Figure 15.** Top left: Disc samples patterned with Ti6Al4V contact pad layer. Bottom left: Samples with the stencil mask are shown. Right: Fixturing of the stencil mask on the disc samples for patterning of the contact pads.

The contact electrode pads of Ti6Al4V were deposited by filtered cathodic vacuum arc at deposition rate of 0.3 μm/h) at low temperature, below 100 °C. Patterning of coatings was performed with mechanical stencils. The principle of patterning is shown in Figure 15.

## 6.2 Deposition of $Al_2O_3$ based coatings

For this study the APS and HVOF thermal spray aluminium oxide based coatings were deposited at laboratories in Tampere University. Fraunhofer-institute IWS provided the S-HVOF thermal spray coatings, and Oerlikon Metco APS aluminium oxide coatings together with the sealant material for the study. The PVD aluminium oxide coatings were deposited at Oerlikon Balzers Coating Finland by RF sputtering on a DVCS A vacuum coater.

The thermal spray coatings in the study consisted of APS- and HVOF-deposited aluminium oxide coatings and for comparison, APS-deposited aluminium oxide based $Al_2O_3$-30%MgO and $Al_2O_3$-3%$TiO_2$ coatings. The thickness range of the coatings varied from 15 μm thick S-HVOF aluminium oxide coatings up to 290 μm thick APS aluminium oxide coatings.

The PVD aluminium oxide coatings were deposited by RF sputtering from a pure aluminium target in an $O_2$/Ar partial pressure. The thickness range of the coatings varied from 1 μm up to 9 μm.

### 6.2.1 APS and HVOF thermal spray of $Al_2O_3$ based coatings

The data of the thermal spray process parameters and feedstock materials used in the study are listed in Table 2. The pure aluminium oxide coatings deposited by APS and HVOF thermal spray were compared to the APS-deposited $Al_2O_3$-30%MgO and $Al_2O_3$-3%$TiO_2$ coatings. The aluminium oxide coatings deposited by S-HVOF from two experimentally-developed suspensions, A with sub micrometre sized (< 1 μm) aluminium oxide particles and B with micrometre sized particles, were compared to standard APS and HVOF aluminium oxide coatings. Later in the study the coatings are referred to by their sample codes.

Samples 21C001 +, 21C003 +, and 21C005 + marked with a sealant, shown in Table 2, were treated with a solvent-free, two component resin solution S106-049 provided by Oerlikon Metco to reduce the open porosity of the thermally sprayed coatings, and to study the influence on the dielectric properties in humid conditions.

**Table 2.** APS and HVOF thermal spray deposited aluminium oxide samples from the study.

| Sample Code | Process | Spray Gun | Fuel Gas | Composition | Particle size [µm] | Thickness [µm] | Source |
|---|---|---|---|---|---|---|---|
| AlO1_70 | HVOF | HVOF TopGun | Ethylene | $Al_2O_3$ | 5-20 | 70 | TAU |
| AlO1_40 | HVOF | HVOF TopGun | Ethylene | $Al_2O_3$ | 5-20 | 40 | TAU |
| AlO5_70 | APS | Pro Plasma | $Ar/H_2$ | $Al_2O_3$ 99.5% | 15-45 | 70 | TAU |
| AlO5_200 | APS | Pro Plasma | $Ar/H_2$ | $Al_2O_3$ 99.5% | 15-45 | 200 | TAU |
| AlO27_70 | APS | Pro Plasma | $Ar/H_2$ | $Al_2O_3$-30% MgO | 22.5-45 | 70 | TAU |
| AlO27_200 | APS | Pro Plasma | $Ar/H_2$ | $Al_2O_3$-30% MgO | 22.5-45 | 200 | TAU |
| 200073TC01 | S-HVOF | HVOF TopGun | Ethylene | $Al_2O_3$ 99.9% | < 1 | 20 | FhG IWS |
| 200075TC01 | S-HVOF | HVOF TopGun | Ethylene | $Al_2O_3$ 99.9% | < 1 | 50 | FhG IWS |
| 200076TC01 | S-HVOF | HVOF TopGun | Ethylene | $Al_2O_3$ 99.9% | < 1 | 80 | FhG IWS |
| 200077TC01 | S-HVOF | HVOF TopGun | Ethylene | $Al_2O_3$ 99.9% | < 1 | 200 | FhG IWS |
| 210016TC01 | S-HVOF | HVOF TopGun | Ethylene | $Al_2O_3$ 99.9% | < 1 | 200 | FhG IWS |
| 210012TC01 | S-HVOF | HVOF TopGun | Ethylene | $Al_2O_3$ 99.8% | µm sized | 15 | FhG IWS |
| 210013TC01 | S-HVOF | HVOF TopGun | Ethylene | $Al_2O_3$ 99.8% | µm sized | 40 | FhG IWS |
| 210014TC01 | S-HVOF | HVOF TopGun | Ethylene | $Al_2O_3$ 99.8% | µm sized | 70 | FhG IWS |
| 210015TC01 | S-HVOF | HVOF TopGun | Ethylene | $Al_2O_3$ 99.8% | µm sized | 200 | FhG IWS |
| 21C0001 | APS | Metco APS | Ar | $Al_2O_3$ 99.8% | 5-45 | 280 | Metco |
| 21C0001+ sealer | APS | Metco APS | Ar | $Al_2O_3$ 99.5% | 5-45 | 280 | Metco |
| 21C0002 | APS | Metco APS | $Ar/H_2$ | $Al_2O_3$ 99.5% | 5-45 | 242 | Metco |
| 21C0003 | APS | Metco APS | $Ar/H_2$ | $Al_2O_3$ 99.5% | 5-45 | 255 | Metco |
| 21C0003 + sealer | APS | Metco APS | $Ar/H_2$ | $Al_2O_3$ 99.5% | 5-45 | 255 | Metco |
| 21C0004 | APS | Metco APS | $Ar/H_2$ | $Al_2O_3$ 99.5% | 5-45 | 293 | Metco |
| 21C0005 | APS | Metco APS | $Ar/H_2$ | $Al_2O_3$-3% $TiO_2$ | 5-45 | 264 | Metco |
| 21C0005 + sealer | APS | Metco APS | $Ar/H_2$ | $Al_2O_3$-3% $TiO_2$ | 5-45 | 264 | Metco |

### 6.2.2 PVD deposition of $Al_2O_3$ coatings by reactive RF sputtering

The PVD coatings were deposited by reactive RF sputtering of a MeiVac MAK 2 source having an aluminium target of 2 inches in diameter, shown in Figure 16. The source was connected to a SEREN IPS AT3 matching network and MC2 matching network controller with the SEREN IPS R301 radio frequency power supply shown in Figure 17. The depositions were carried out from an aluminium target of 99.5 % purity at 300 W RF power in a DC probe voltage control mode of 400 to 500 volts. The background pressure was kept at $7 \times 10^{-3}$ mbar measured with a hot cathode vacuum gauge and at 70 SCCM argon flow before starting reactive sputtering of the

aluminium oxide coating in $O_2$/Ar partial pressure. The constant gas flow of argon and oxygen was adjusted with MKS G-series mass flow controllers.

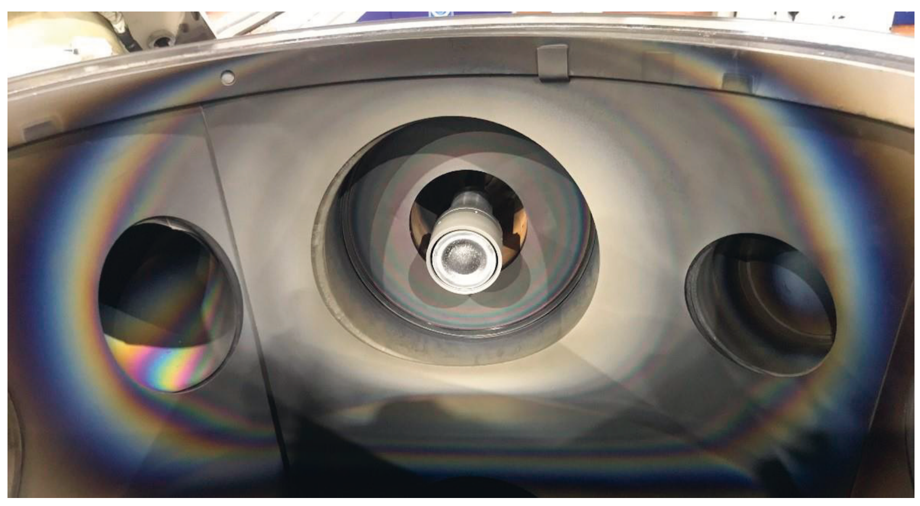

**Figure 16.** MeiVac MAK 2 sputter source with a two-inch aluminium target.

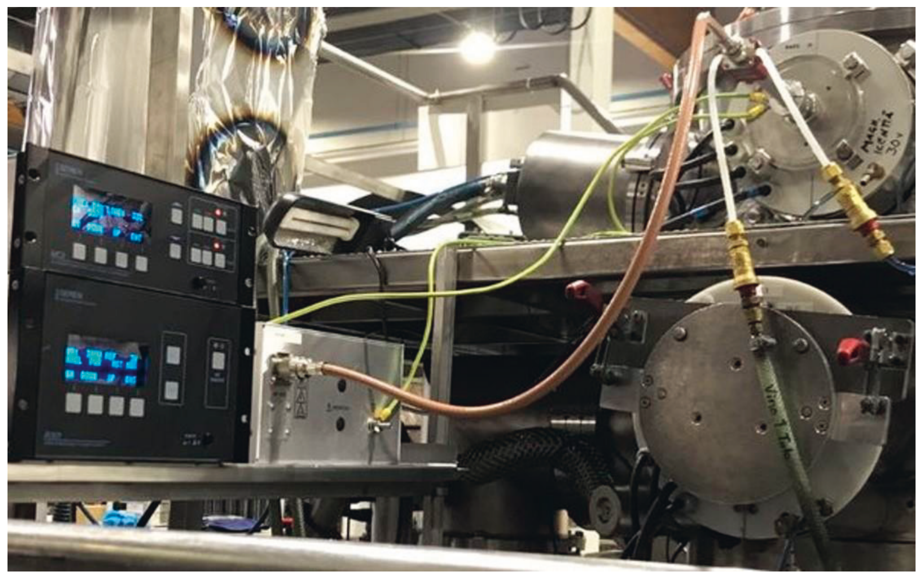

**Figure 17.** MeiVac MAK 2 sputter connection to SEREN IPS R301 RF power supply with SEREN IPS AT3 automatic matching network and MC2 matching network controller.

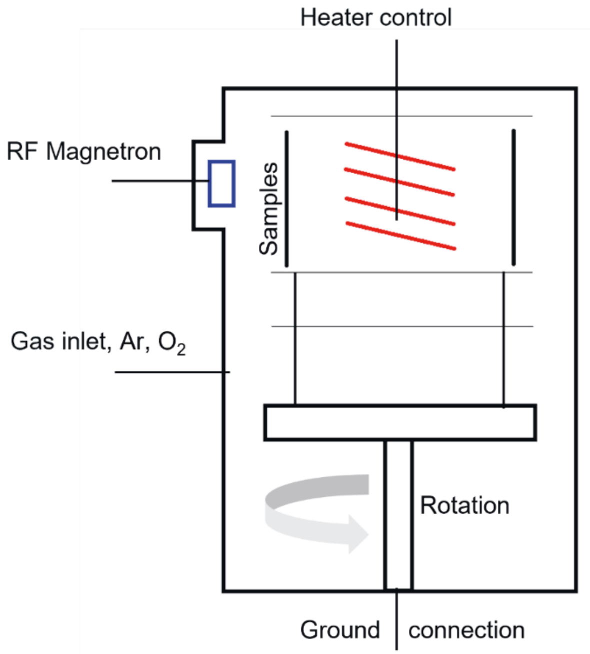


**Figure 18.** RF-sputter deposition set-up in the vacuum chamber.

Figure 18 shows the deposition set-up in the vacuum chamber. The substrate disc samples of 90MnCrV8 were placed on a cylindrical sample holder in the centre of the vacuum chamber at a distance of 85 mm between the target and the substrates in the holder. The depositions were carried out from room temperature up to a maximum substrate temperature of 250 °C, which is still acceptable in the coating system.

For the deposition at elevated temperature, a heater setup and a sample holder, shown in Figure 19, were designed and built in the centre of the rotating manipulator. The temperature during the aluminium oxide deposition was controlled by a thermocouple located in the centre of the heater coil. The relation of the heater temperature to the substrate temperature was measured from the surface temperature with an Omega IR sensor probe. Calibration of the substrate temperature in relation to the heater temperature is shown in Figure 20.

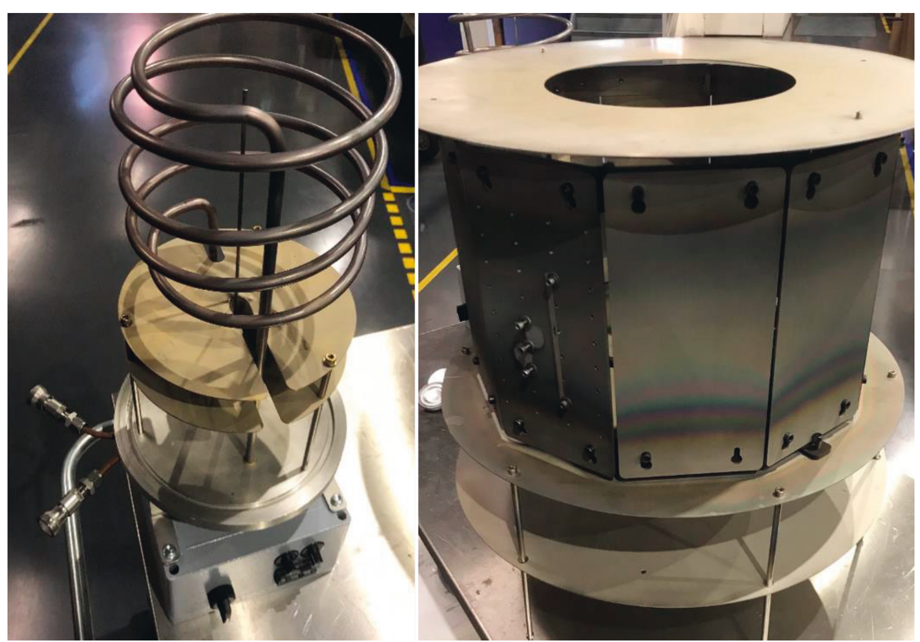

**Figure 19.** Heater with control set-up (left) and sample holder (right).

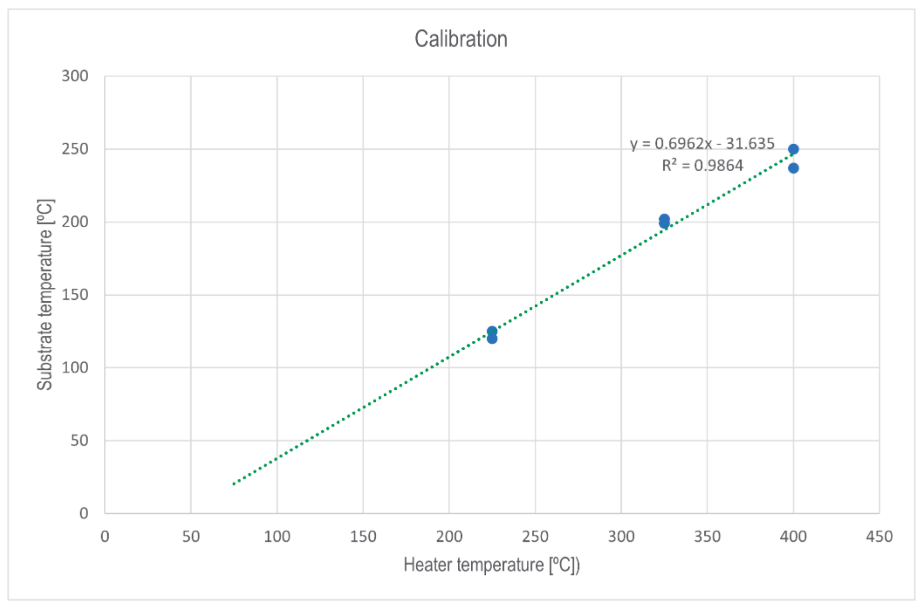


**Figure 20.** Calibration of substrate temperature with Omega IR sensor probe to heater temperature measured with a thermocouple.

The small size of the aluminium target makes adjustment of the operating point of the DC probe voltage relatively simple with low hysteresis between the metallic and reactive modes of RF sputtering. Figure 21 shows the hysteresis of the deposition set-up from metallic to reactive mode and back at 300 W RF sputtering as a function of the $O_2$/Ar ratio at a temperature of 200 °C. The deposition of the aluminium oxide coatings was performed in DC probe voltage control mode between 350 and 500 volts.

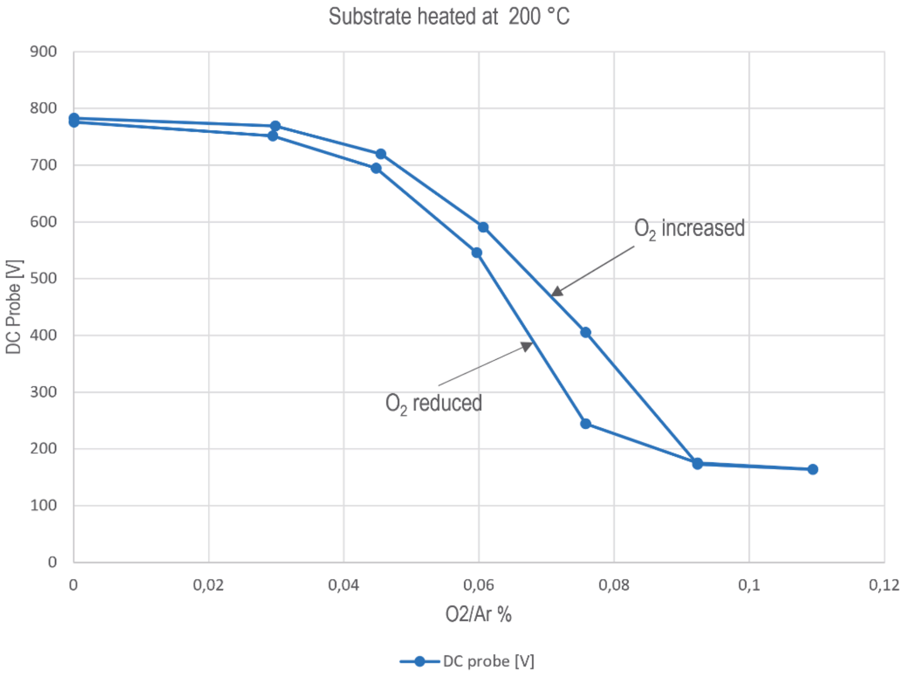


**Figure 21.** Hysteresis in reactive RF sputtering of aluminium oxide coating at 200 °C.

### 6.2.3 RF-sputtered aluminium oxide coatings

The PVD aluminium oxide coatings deposited by RF sputtering are summarized in Table 3. The depositions were carried out at three base pressures of 3 µbar, 6 µbar and 12 µbar measured with a capacitance manometer. The source target operation was run in DC probe voltage control mode between a voltage of 350 to 500. The deposition temperature was varied from room temperature (RT) without heating up

the sample to a maximum substrate temperature of 250 °C. The conditions with 300 W RF operating power resulted in aluminium oxide coating deposition rates of around 0.3 μm/h. The code names of the aluminium oxide coatings are used when the samples are referred to later in the study.

**Table 3.** PVD aluminium oxide coatings deposited by RF sputtering.

| Sample Code | Pressure [μbar] | Ar flow [sccm] | O2 flow [sccm] | DC probe voltage | Deposition temp. [°C] | Coating thickness [μm] | Deposition rate [μm/h] |
|---|---|---|---|---|---|---|---|
| 120721A1 | 12 | 68 | 6 | 500 | no heating | 0.58 | 0.32 |
| 040821A1 | 12 | 66 | 6 | | 125 | 0.85 | 0.30 |
| 050821A1 | 12 | 67 | 5 | 400 | 200 | 1.30 | 0.22 |
| 060821A1 | 6 | 67 | 6 | 540 | 250 | 0.89 | 0.30 |
| 140921A1 | 12 | 68 | 5 | 500 | 250 | 1.50 | 0.26 |
| 160921A1 | 12 | 67 | 5 | 360 | 250 | 1.40 | 0.18 |
| 240921A1 | 12 | 31 | 3.5 | 400 | 250 | 1.12 | 0.20 |
| 270921A1 | 6 | 14 | 3 | 400 | 250 | 0.54 | 0.11 |
| 280921A1 | 3 | 14 | 2.5 | 520 | 250 | 1.19 | 0.21 |
| 290921A1 | 3 | 68 | 4 | 560 | 250 | 0.61 | 0.27 |
| 251112A1 | 12 | 65 | 8 | 450 | no heating | 1.26 | 0.28 |
| 261121A1 | 12 | 30 | 5 | 660 | no heating | 1.73 | 0.25 |
| 221221A1 | 6 | 30 | 4 | 440 | no heating | 1.58 | 0.27 |
| 231221A2 | 6 | 65 | 6.5 | 500 | no heating | 1.77 | 0.32 |
| 301221A1 | 12 | 65 | 5.5 | 370 | no heating | 8.79 | 0.82 |

## 6.3 Test methods of electrically insulating coatings

To study the dielectric properties of different aluminium oxide coatings, PVD test electrodes of Ti6Al4V were deposited on thermal spray and PVD aluminium oxide coatings: images are shown in Figures 13 and 14. The layer thickness of the electrodes was chosen depending on the roughness of the substrate and the aluminium oxide layer. The nominal thickness varied from 250 nm on thermal spray coatings to 100 nm on PVD coatings. The electrical continuity and coverage of the electrode coatings on HVOF and APS aluminium oxide coatings was controlled by a two-point measurement of the electrode sheet resistance, shown in Figure 22. The roughness parameters of the aluminium oxide coatings were measured with a Dektak XT profilometer. Thickness measurements of APS and HVOF aluminium oxide coatings were performed optically with a Leica DM 2500M metallurgical microscope and of PVD coatings with a profilometer and SEM.

The APS and HVOF with Ti6Al4V thin film electrode layer were characterized by scanning electron microscope (SEM) Jeol IT-500 equipped with an energy dispersive spectroscopy (EDS) analyser. Structure of S-HVOF aluminium oxide coatings were characterized by SEM Jeol JSM-6610. The PVD aluminium oxide coatings were characterized by SEM Zeiss Supra 40VP. The roughness and thickness of the coatings were measured with a Dektak XT profilometer. The phase structure of the crystallinity of the PVD aluminium oxide coatings were also studied with XRD Bruker D8 Advance.

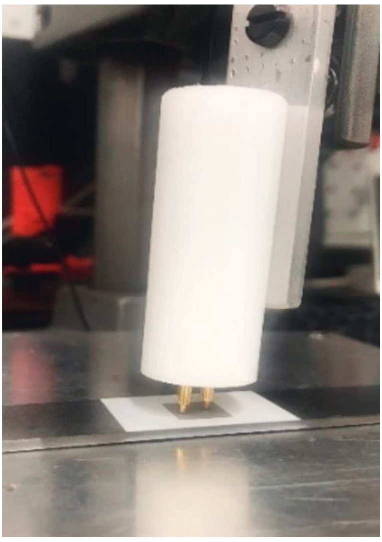

**Figure 22.** Two-point measurement of sheet resistance of Ti6Al4V contact electrode on HVOF- and APS-deposited aluminium oxide coatings.

The dielectric properties and resistivity of the aluminium oxide coatings were studied using direct current measurement in a voltage range between 10 to 200 VDC. The measurements were performed both on a Peltier cooling element in a temperature range between +5 °C and 50 °C in ambient air conditions and in a Vötsch climatic test cabinet VCL 4003 in a temperature range from -10 °C to +90 °C, and in 10% RH to 80%RH relative humidity. All the measurements of the thermal spray coatings were performed on the samples as-deposited without any post-treatment prior to the deposition of Ti6Al4V electrodes.

The relative dielectric coefficient of aluminium oxide coatings was determined by the capacitance measurement at 1kHz with Amprobe LCR 55 meter. Two-point probe resistance measurement was used to determine the conductivity of the Ti6Al4V contact pads deposited as a counter electrode on the aluminium oxide layer.

The thermistor sensitivity of the piezoresistive carbon thin films deposited on aluminium oxide layers was performed in a Vötsch climatic test cabinet to determine the beta value of the sensors. A bend test in 6.3.3 was designed to measure the strain and fracture toughness and to determine the gauge factor of the hard carbon thin films on the aluminium oxide dielectric layers. The sensitivity of the measured beta value and gauge factor of the carbon sensor layers deposited on the aluminium oxide coatings were compared to the reference sensors deposited on a polyimide substrate.

### 6.3.1 Leakage current measurement of electrically insulating coatings

Leakage current measurement of the aluminium oxide layers was performed with the direct current measurement set-up shown in Figure 23. The current is measured as a voltage Um over the 100 kΩ shunt resistor connected between a programmable voltage source and the test specimen. The electrical contact to the test specimen is formed via a spring-loaded contact to the titanium electrode. The voltage Um over the shunt resistor is measured with an Agilent 3497A data logger.

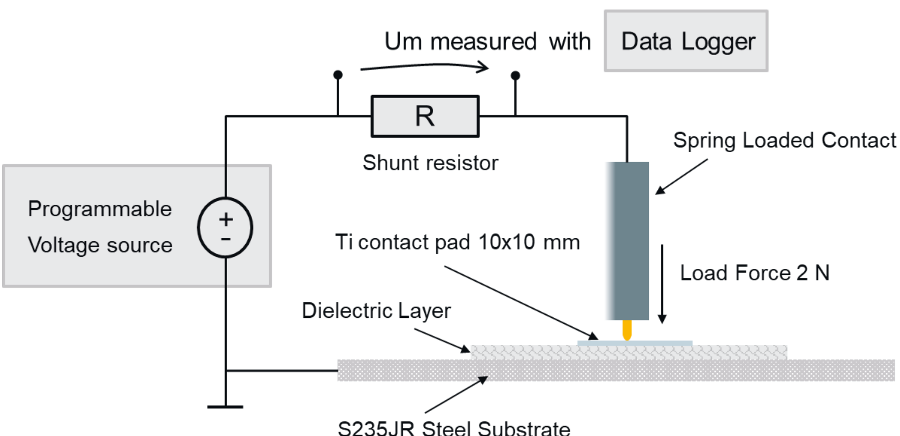


**Figure 23.** Principle of leakage current measurement of aluminium oxide dielectric layers.

Firstly, in the measurement procedure the voltage source is ramped up in 10 VDC steps to 200 VDC high end voltage. For each step during the ramp-up phase the voltage is kept for 15 s to let the polarization current stabilize. The specimen is kept for 30 minutes at the high voltage level to measure and record the direct current. The measurement procedure is repeated three times for each specimen with 30 min waiting time between the sequences. With this measurement set-up, the direct current of the aluminium oxide layers can be measured up to a $10^{13}$ Ω resistance level.

The leakage current measurement provides information on the long-term stability and space charge behaviour of the aluminium oxide dielectric layers in variable ambient conditions.

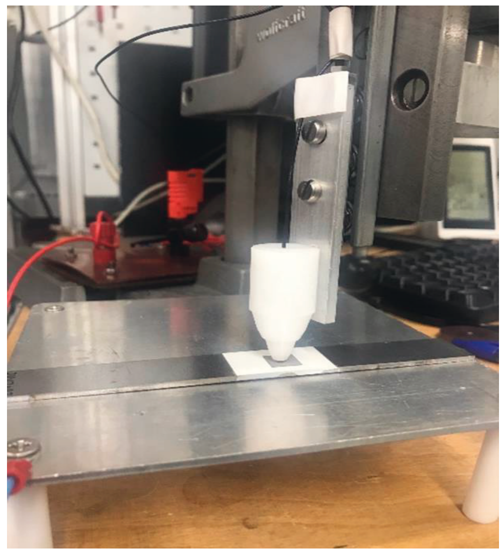

**Figure 24.** Direct current measurement of cantilever beam test specimen.

### 6.3.2 Capacitance measurement of electrically insulating coatings

The capacitances of the test specimen were measured at room temperature in ambient air conditions and at temperatures from 5 ºC to 50 ºC set with a Peltier element. The capacitance measurements were performed with a bridge-connected Amprobe LCR55A capacitance tester at 1 kHz measurement frequency.

An RC model with parallel resistance R was used to estimate the error in the measured capacitance $C_m$ to the real capacitance $C_r$ at angular frequency $\omega = 2\pi x10^3$ Hz with the following formula (2):

$$C_m = \sqrt{C_r^2 + \frac{1}{R^2\omega^2}} \tag{2}$$

Relative permittivity is calculated as ratio $\varepsilon_r = C_m/C_o$ from measured capacitance $C_m$ and geometrical capacitance $C_o$ of the specimen in vacuum.

In the case of space charge polarization, the RC model is not satisfactory to describe dielectric losses which are time dependent. For the total permittivity $\varepsilon^*_r$, space charge polarization must be included with the following formula (3):

$$\varepsilon_r^* = \varepsilon_r - j\left(\varepsilon_r' + \frac{1}{\omega\rho}\right) \tag{3}$$

where $\varepsilon_r'$ is the time-dependent term caused by dissipation during polarization, and the second term inside the parenthesis is the resistivity $\rho$ of the dielectric film.

### 6.3.3 Strain measurement of electrically insulating coatings performed with hard carbon thin film sensor

The fracture toughness and adhesion of the aluminium oxide coating on the S235JR cantilever beam is tested indirectly by bending the beam with force P, causing a deflection $w(x)$ to the free end of the beam at point C. Strain $\varepsilon$ caused by a known deflection and force is measured as a resistance change in the embedded hard carbon film deposited on the aluminium oxide coating at a distance of L/2, as shown in Figure 25.

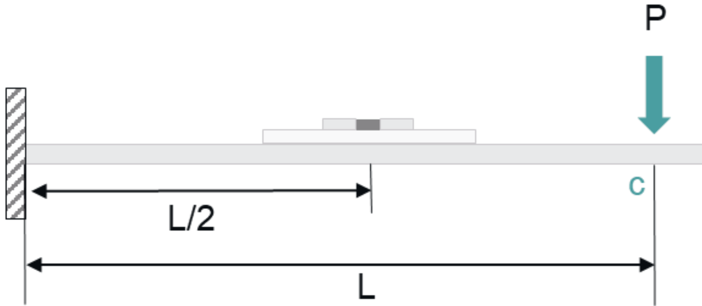


**Figure 25.** Strain measurement with piezoresistive carbon thin film.

Strain ε of the cantilever beam at distance x and at height z = d/2 (at the top surface of the cantilever beam) caused by force P at point C for an isotropic linear material (using Hooke's law σ = E ε) is calculated with formula (4):

$$\varepsilon = -z\frac{P(L-x)}{EI}\,, \tag{4}$$

where E is the elastic modulus and $I = wd^3/12$ is the second moment of area of the cantilever beam, where w is the width of the beam and d is the thickness of the beam. The bend test set-up for the strain measurement is shown in Figure 26.

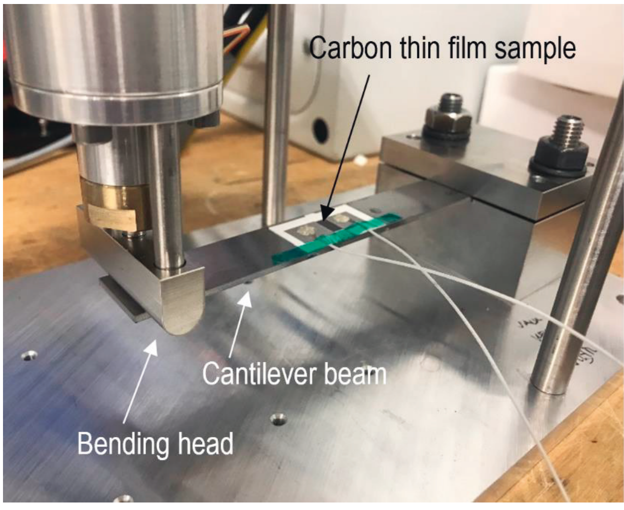


**Figure 26.** Bend test set-up for strain measurement of cantilever beam samples.

In the test procedure, the bending head moves first on the sample surface and is held in position for 30 seconds. Next, the bending head moves 1 mm downwards at a speed of 0.05 mm/s, causing a 1mm deflection of the cantilever beam at point C and is held in position for 30 seconds. After this, the bending head moves back 1 mm upwards to start again. The sequence is repeated as many times as needed for testing the material fatigue and fracture toughness of the embedded layer structure.

The dimensions Lxbxh of the beam are 120x20x2 in mm. In the test set-up, force P of 5 N causes a 1 mm deflection $\omega_c$ at point C and about a 0.01% strain at point L/2 in the location of the embedded sensor. The test was also performed also with 2 mm and 3 mm deflections.

The gauge factor, GF, of the carbon thin film is related the relative change $\Delta R/R$ of the resistance to strain $\varepsilon$, as shown in formula (5):

$$GF = \frac{\Delta R/R}{\varepsilon} \tag{5}$$

The gauge factor is characteristic of the sensor material used and nearly constant in the elastic region of the stress-strain relation. When cyclic testing is performed with a constant deflection, the gauge factor of the carbon thin film is used as a sensitive indicator for any nonlinear change in the film caused by fracture or fatigue in the dielectric layer.

# 7 RESULTS AND DISCUSSION

In the following chapter the general findings of experimental results are presented at first in chapter 7.1 and then discussed more in detail in chapters 7.2-7.6.

## 7.1 General discussion of the experimental results

The feasibility of aluminium oxide coatings for electrical insulation of thin film hard carbon sensors was studied first by measuring the surface properties of as-deposited insulating layers with measurements of the roughness parameters and layer thicknesses. The sheet resistance of the Ti6Al4V thin film contact pads deposited on the insulating coatings was measured and the structure and conformity of the films were characterized by SEM and EDS.

The dielectric properties of the thermal spray insulating layers were compared by leakage current measurements performed in ambient air conditions and on a Peltier element at temperatures of +5 ºC and +55 ºC, as shown in Figure 27. The resistivity values measured at 20 ºC and 20% RH were between $10^{10}$–$10^{11}$ Ωm and were very similar for both APS and HVOF aluminium oxide coatings. The influence of humidity on the dielectric properties was further studied with HVOF coatings in a Vötsch climatic cabinet by varying the relative humidity between 20% RH and 80% RH at different temperatures. The results showed a clear decrease in resistivity of the thermal spray aluminium oxide coatings measured at a high level of humidity and in dew point conditions.

Possibilities to improve the resistivity of thermal spray coatings were studied with $Al_2O_3$ and $Al_2O_3$-3%$TiO_2$ APS coatings impregnated with a novel, solvent-free two-component resin solution of S106-049 sealant. The electrical resistance of the APS coatings was compared to the impregnated coatings in cyclic change of relative humidity from 40% RH to 80% RH and back to 40% RH at a temperature of 40 ºC. The results indicated a clear improvement in insulation resistance gained with the

sealant compared to the APS insulating layers. The impregnated APS coatings had an insulation resistance of over $1.2 \times 10^8$ **Ω** after exposure to a relative humidity of 80% RH and measured at temperatures ranging from -10 ºC to + 30 ºC.

The dielectric properties of S-HVOF coatings deposited from two suspensions of sub-micrometre-sized aluminium oxide feedstock material A and from micrometre-sized feedstock material B, were compared to a 40 µm HVOF aluminium oxide coating. The measured mean roughness depth of the HVOF and S-HVOF coatings possessed the same average $R_z$ value of around 9 µm while the rougher APS coatings had average Rz value of 17.5 µm as comparison. The resistivity of the S-HVOF coatings was slightly higher, at $\sim 10^{12}$ Ωm, with coatings deposited from suspension A than with coatings deposited from suspension B, which had a resistivity of $\sim 10^{11}$ Ωm, very similar to the 40 µm HVOF coating. Higher resistivity measured in S-HVOF coatings of suspension A is most probably related to smaller particle size of suspension A forming a denser microstructure. All the S-HVOF samples were measured in dry conditions of below 20% RH.

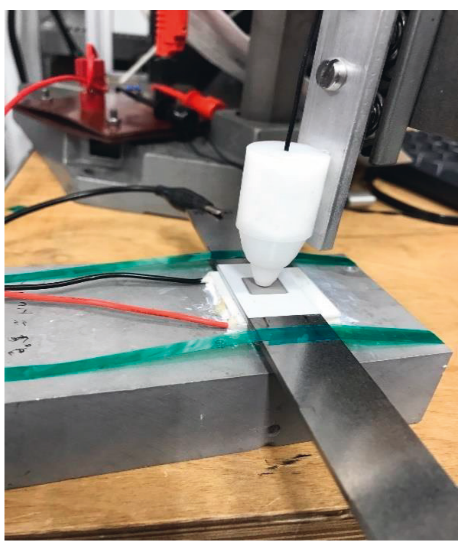

**Figure 27.** Aluminium oxide samples placed on a Peltier cooling element for leakage current and capacitance measurement at temperatures between +5 and +50 ºC.

The piezoresistive properties of the hard carbon sensor element were studied with the APS and HVOF thermal spray coatings. The beta value of the hard carbon thin film sensor elements, acting as a NTC thermistor, was successfully measured in a climatic cabinet at temperatures ranging from -10 °C to +70 °C for all the thermal spray samples. The average beta value of the thermal spray samples was 1070 with a standard deviation of ± 15. The measured beta value was higher for all of the thermal spray samples than the beta value of 1030 measured on a polyimide substrate. The gauge factor of the carbon sensors was also successfully measured from the same thermal spray samples in the bend test with a 1 mm cantilever beam deflection. The average gauge factor of the samples was 5.83, with a standard deviation ± 0.46 influenced by the high surface roughness of the thermal spray samples. The value of the gauge factor on the aluminium oxide insulating layers was three times higher than the value measured for a commercial metal foil strain gauge, LY21-3/120 on the polyimide substrate in the bending test measured under the same conditions.

The mechanical fatigue resistance of an APS aluminium oxide coating of 200 µm was studied indirectly in a cyclic 3 mm bending of the cantilever beam with a hard carbon sensor on the APS layer. The gauge factor of the sensing element deposited on the APS layer was measured during a 24-day long test period for the detection of potential fracture in the layers. The average gauge factor was 5.6 with a standard deviation of ± 0.12 during the measurement of fatigue resistance. No drift was observed in the gauge factor during the cyclic fatigue testing. The optical imaging of the top layers did not reveal defects in the coatings caused by fatigue; the visual outlook of the sample was intact.

For the study RF-sputtered aluminium oxide coatings were deposited at argon pressure levels of 3 µbar, 6 µbar and 12 µbar and at temperatures of 20–250 °C with an oxygen/argon flow ratio ranging between 5% and 20%. The properties of the RF-sputtered aluminium oxide coatings were studied using SEM, EDS and XRD. The coatings deposited at higher argon pressures of 6 µbar and 12 µbar had a columnar layer structure, while the samples deposited at 3 µbar showed dense and less columnar structure. The resistivity measured from the PVD aluminium oxide films was between $4x10^{9}$–$10^{12}$ Ωm. The films suffered from dust particles and pinholes, causing a high defect density in the films. A relatively high DBS of 38 MV/m was estimated for 1 to 2 µm thick films and 22.8 MV/m for the 8.8 µm thick

film from the leakage current measurements. The measured $R_z$ roughness of the ~1 μm thick coatings varied between 0.06 μm and 0.16 μm, depending on the coating thickness and deposition parameters. Leakage current with the RF-sputtered samples in consecutive measurement runs was observed to decrease faster than with thermal spray coatings under high humidity conditions.

## 7.2 Electrical insulation of HVOF- and APS-deposited $Al_2O_3$ coatings

The thermal spray coatings shown in Figure 28 were deposited on S235JR cantilever beams at Tampere University to study the insulating resistance with direct current measurement. The HVOF- and APS-deposited aluminium oxide coatings were compared to magnesium aluminate spinel coatings with thicknesses of 70 μm and 200 μm.

| Sample code | AlO1_70 | AlO5_70 | AlO5_200 | AlO27_70 | AlO27_200 |
|---|---|---|---|---|---|
| Coating type | Alumina | Alumina | Alumina | Spinel | Spinel |
| Method | HVOF | APS | APS | APS | APS |
| Powder | $Al_2O_3$ | $Al_2O_3$ | $Al_2O_3$ | $Al_2O_3$-30%MgO | $Al_2O_3$-30%MgO |
| Thickness | 70 μm | 70 μm | 200 μm | 70 μm | 200 μm |

**Figure 28.** HVOF- and APS-deposited insulating coatings on S235JR cantilever beams.

The roughness parameters shown in Figure 29 are averages of three measurements of each sample measured with a Dektak XT profilometer with a sweep length of 1.5 mm. The HVOF aluminium oxide coating of 70 μm had the lowest roughness values: $R_a$ 1.6 and $R_z$ 9.18. This was only half of the roughness of the APS aluminium oxide and spinel coatings that were deposited from feedstock materials of bulkier particle size, listed Table 2. The APS coatings had nearly the same roughness values for both 70 μm and 200 μm thicknesses. The values of peak and valley roughness were symmetrical with all the coatings. The measured roughness values $R_a$ 0.04 and $R_z$ 0.29 of the polyimide film serve as a reference for the resistance measurement of the contact electrodes.

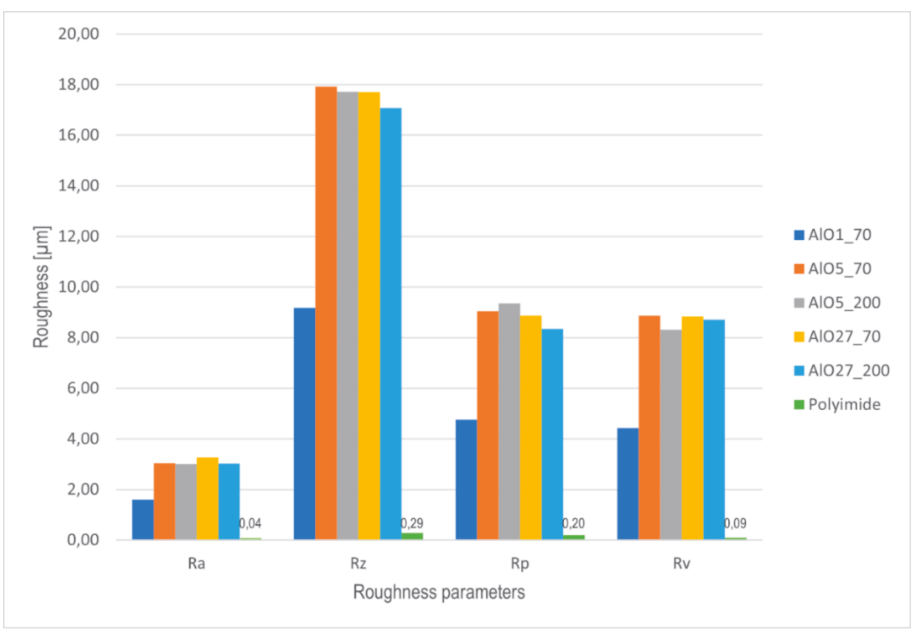


**Figure 29.** Measured average roughness ($R_a$), mean roughness depth ($R_z$), maximum peak ($R_p$) and maximum valley roughness ($R_v$) of HVOF- and APS-deposited aluminium oxide and spinel coatings with comparison to polyimide as reference substrate.

### 7.2.1 Structure of Ti6Al4V contact electrodes deposited on HVOF and APS insulating layers

Ti6Al4V contact electrodes with a nominal thickness of 250 nm and surface area of 10x10 $mm^2$ were deposited by filtered cathodic vacuum arc at a deposition rate of 0.3 µm/h on HVOF and APS thermal spray coatings of S235JR cantilever beams, as shown in Figure 30. Two-point contact measurements were performed to study the sheet resistance of the contact electrodes. The resistances measured at room temperature and at 20% RH are shown in Figure 31. With the lowest roughness, the Al01_70 coating also possesses the lowest electrode sheet resistance 52 ± 2 Ω of the coatings. The influence of surface roughness can be seen when compared to the reference sample, a 100 nm Ti6Al4V coating having a sheet resistance of 12.8 Ω on a polyimide substrate with mean roughness depth $R_z$ of 0.29 µm.

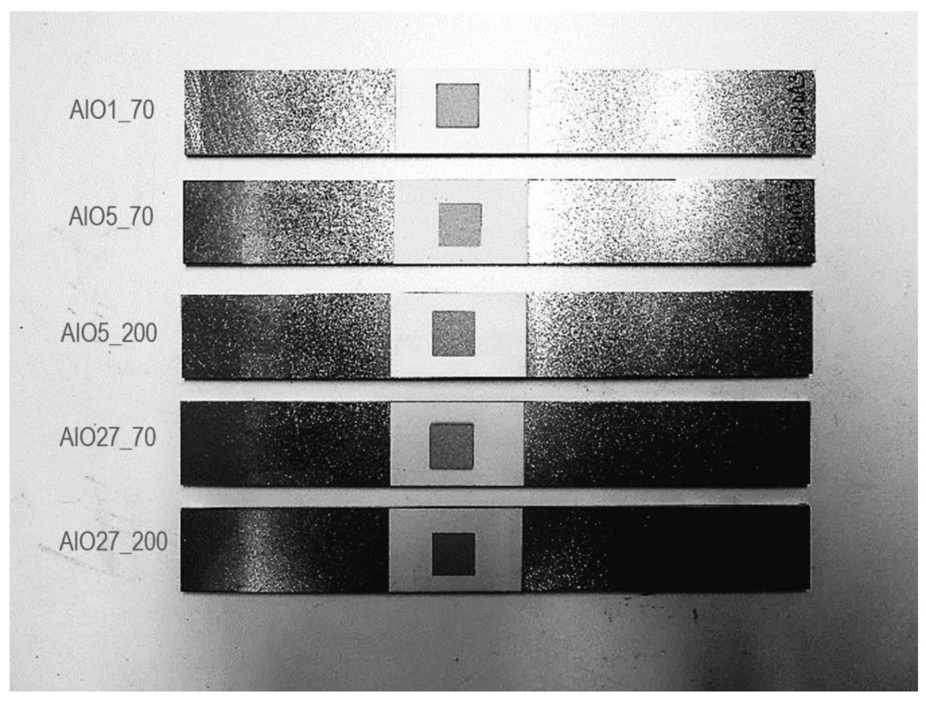


**Figure 30.** Ti6Al4V contact electrodes of 10x10 mm$^2$ deposited on HVOF and APS test samples.

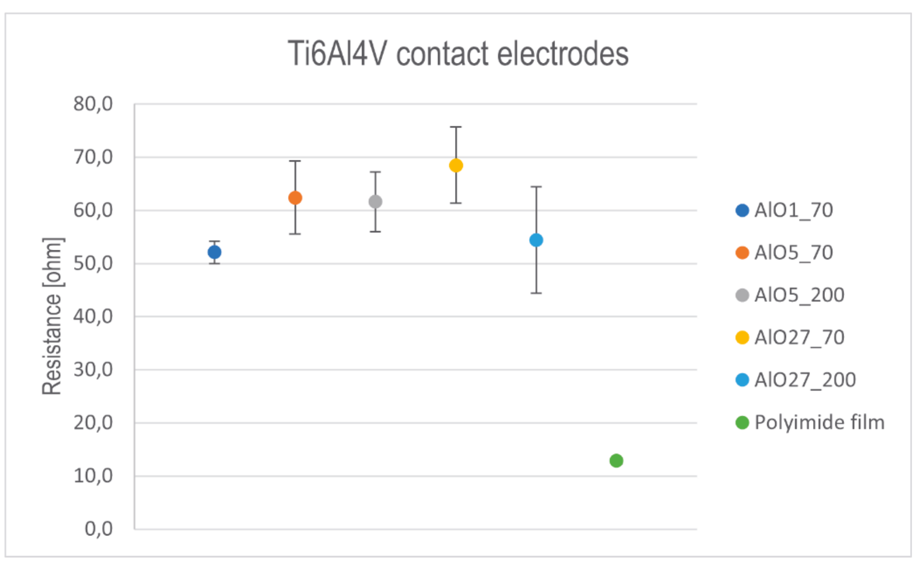


**Figure 31.** Sheet resistances of contact electrodes on HVOF- and APS-deposited samples.

The coverage and continuity of the Ti6Al4V film deposited on the HVOF AlO1_70 sample were studied by SEM Jeol IT-500 equipped with Jeol EDS-analyser. Figure 32 depicts the surface roughness from the top of the coated surface and Figure 33 depicts the coverage of the Ti6Al4V layer on the HVOF aluminium oxide from a sample cross-section. The good conformity of the Ti6Al4V layer can be seen in Figure 34 even on the complex roughness of the AlO1_70 coating. The smooth surface coverage of the Ti6Al4V layer can be seen in Figure 35 as the "white-looking" top layer on the cracked surface of the bent AlO1_70 sample.

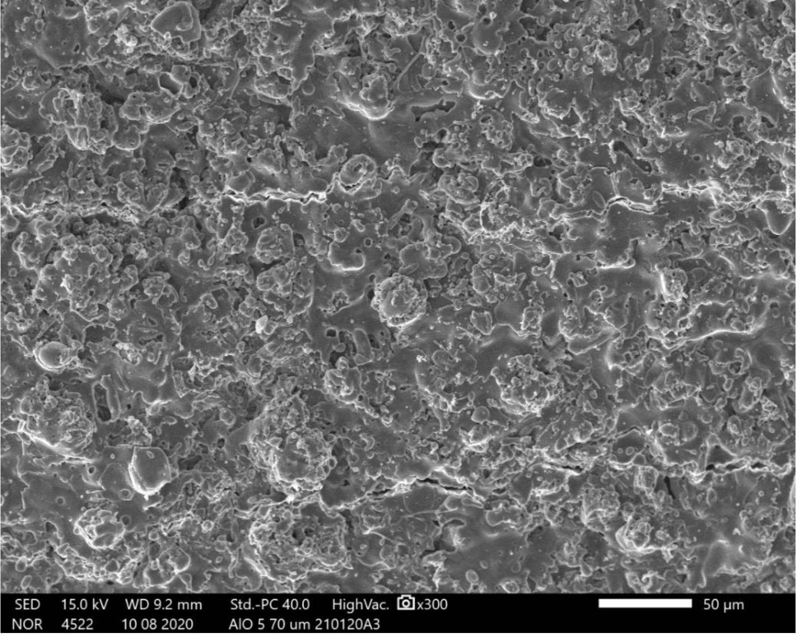


**Figure 32.** SEM image of HVOF-deposited AlO1_70 surface with Ti6Al4V contact electrode layer on top of the rough coating surface.

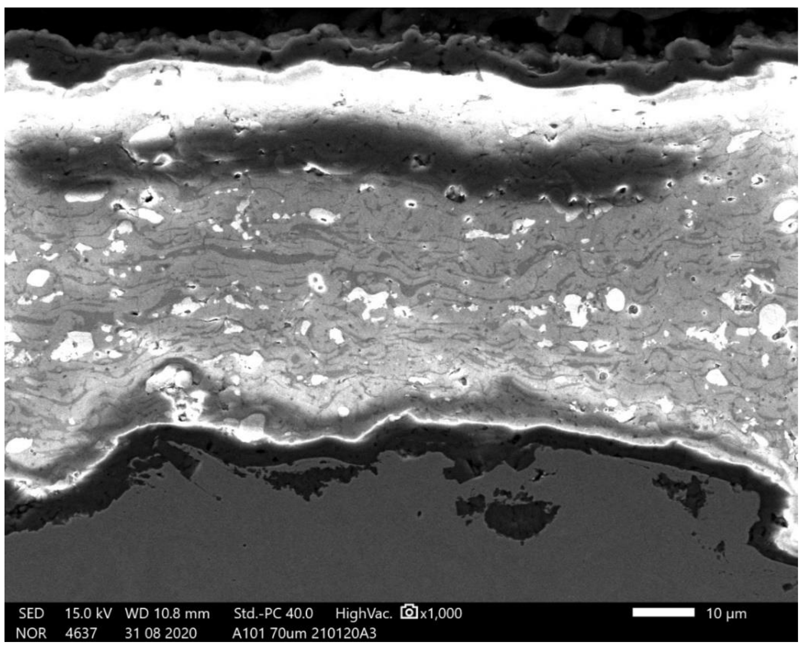


**Figure 33.** Cross-section of cantilever beam sample with HVOF-deposited AlO1_70 aluminium oxide insulation layer and Ti6Al4V electrode layer on top.

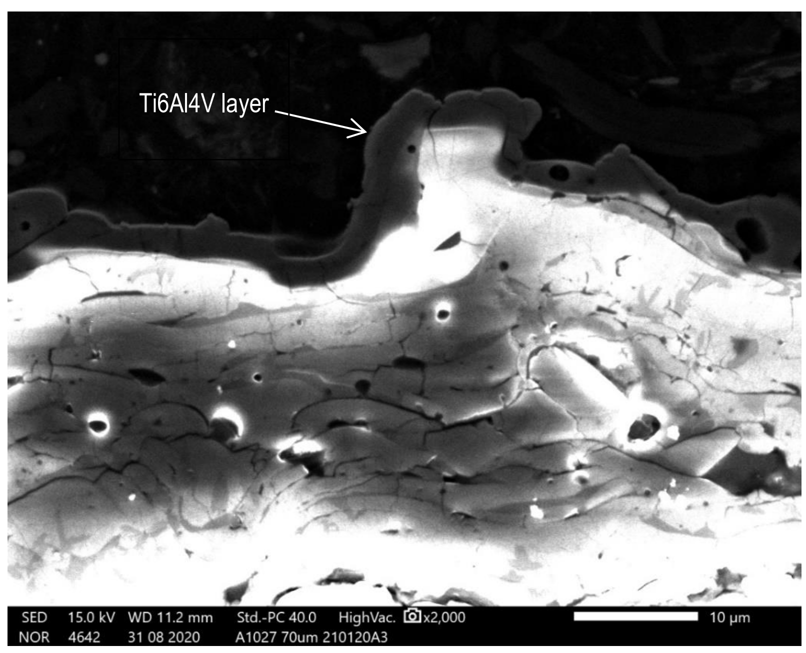


**Figure 34.** Cross-section of Ti6Al4V layer on top of HVOF-deposited AlO1_70 sample.

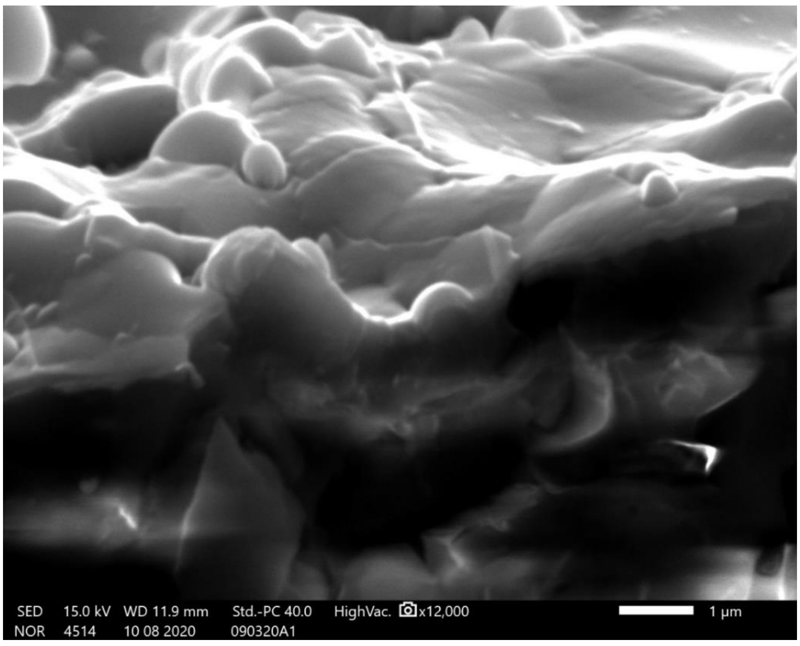


**Figure 35.** Slant view of Ti6Al4V layer on HVOF-deposited aluminium oxide.

The AlO1_70 sample was further studied by EDS elemental mapping of the surface layer. Mapping with 10 μm scale shows the locations of the K-lines of the elements found from SEM image IMG1 of the sample. Titanium K-lines are visually detectable in Figure 36 as a marker of the Ti6Al4V top layer. The EDS analysis shown in Figure 37 confirms the existence of titanium with the K- and L-lines in the sample. The highest intensities in the EDS are from the aluminium and oxygen $K_{\alpha}$-lines of the 70 μm aluminium oxide layer.

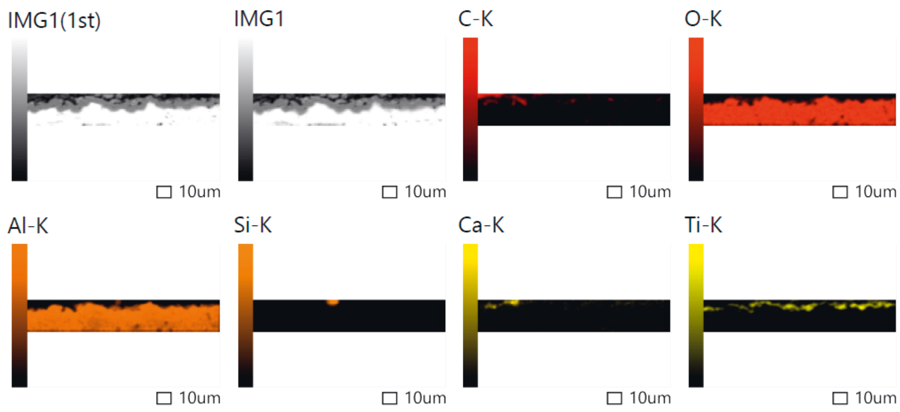


**Figure 36.** EDS mapping from a cross-section of HVOF-deposited AlO1_70 sample with Ti6Al4V top layer.

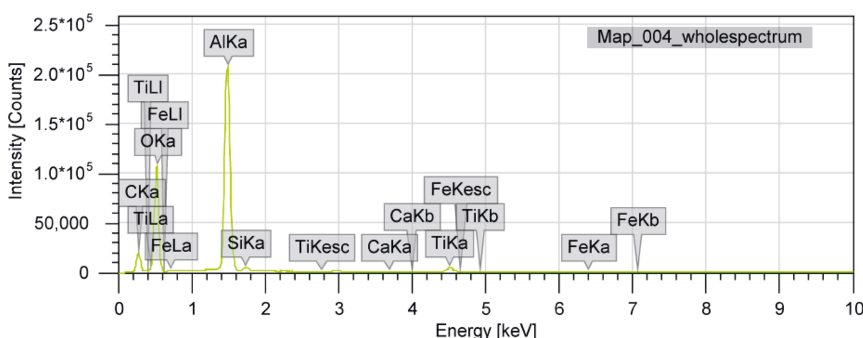


**Figure 37.** EDS analysis from a cross-section of HVOF-deposited AlO1_70 sample with Ti6Al4V top layer.

### 7.2.2 Dielectric properties of HVOF- and APS-deposited thermal spray coatings

The direct current measurement described in Chapter 6.3.1 was performed at a room temperature of 21 °C and 20% RH for each of the samples: AlO1_70, AlO5_70, Al05_200, AlO27_70 and AlO27_200 up to a voltage level of 200 VDC. The test run was started by ramping up the voltage in 10 VDC steps with a hold time of 15 s on each level, resulting in a total ramp up time of 300 s to reach the 200 VDC test voltage level. The voltage was kept at this level for a period of 30 minutes. Between each test run there was half an hour waiting time before starting up the next step run to avoid potential influence of space charge polarisation on the measurement. The test run was repeated three times and the direct current through the insulation coatings was calculated from the data logged voltage over the shunt resistor. With all the thermal spray insulating materials, each consecutive run showed a reduction in the leakage current similarly to the AlO1_70 sample shown in Figure 38.

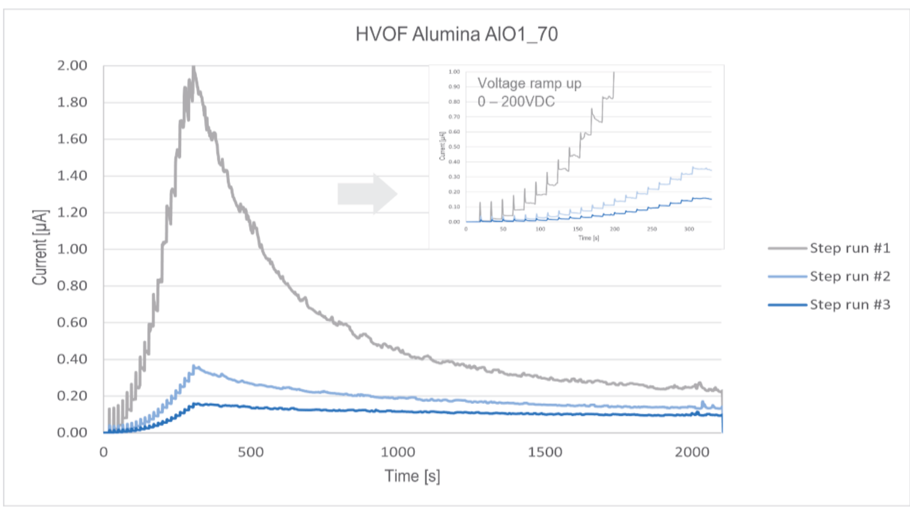


**Figure 38.** Leakage current of AlO1_70 sample in three consecutive measurement step runs.

The current of the insulating layers caused by dielectric polarization was visible at low voltage levels as the serrated-like current peaks seen in the charge current at each voltage step change during the voltage ramp-up from 0 to 200 VDC level. During the first step run, the peaks were visible up to the 100 VDC level but above this the current was masked by some additional source of leakage which was dominant at

high voltage levels above 100 VDC. The maximum leakage current was seen just after the voltage level of 200 VDC was reached. Within the measurement period of 30 minutes at 200 VDC, the leakage current decayed by a factor of 2–10, depending on the insulating material. This indicated that leakage current cannot be considered as a pure resistive component and that there is also an effect of some kind of long-term space charge polarization causing a drift in the resistance. A similar current drift was seen with all the tested samples. The first assumption was that the drift was caused by some change in the conductivity of the dielectric layer between the electrode and the cantilever beam. Figure 39 shows the direct current measured after the third consecutive step run of insulation coatings. It was characteristic that the thicker 200 µm coatings of AlO5 and AlO27 had a higher leakage current than the 70 µm layers. During the third step run, there was still a drift of 30–40% in the direct current on all insulation layers. Even though the steady state condition of the direct current was not achieved, the 70 µm AlO1, AlO5 and AlO27 samples already showed a relatively low drift in the current during the measurement period.

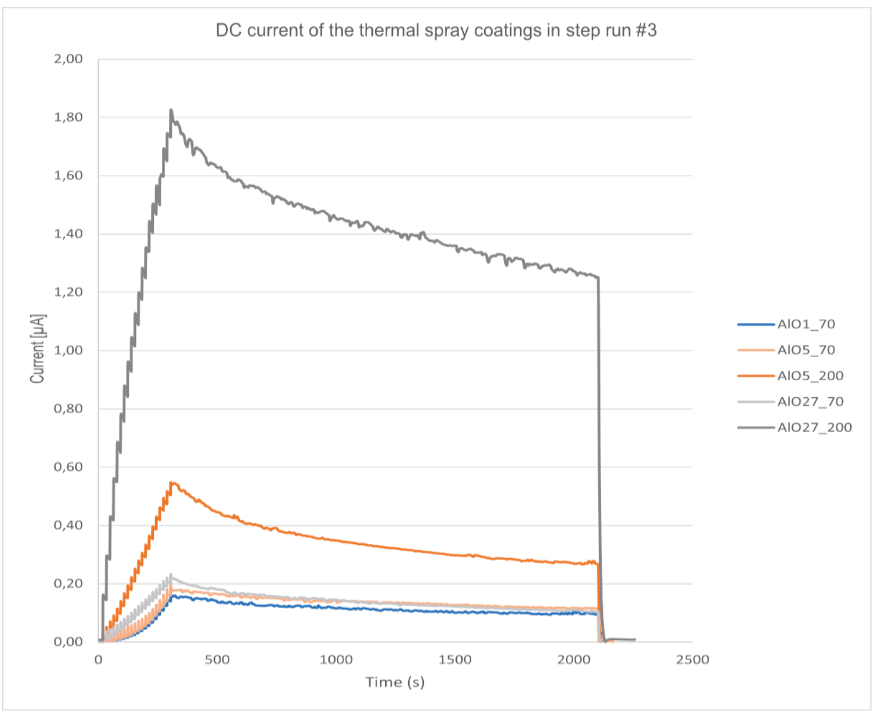


**Figure 39.** Leakage current of HVOF- and APS-deposited electrical insulation layers measured at a voltage level of 20 VDC.

The fourth test run was performed to compare the resistivities of the materials at the 20 VDC level and in ambient air conditions of 21 °C and 20% RH. The resistivity was calculated using the formula $\varrho = RxA/d$, where R is the measured electrical resistance of the coating calculated from the integrated average of the current over a 30 min measurement period at 20 VDC, A is the electrode area of 10x10 $mm^2$ and d is the thickness of the coating, either 70 µm or 200 µm.

The current peaks at charging the AlO1_70 sample were clearly visible in the two consecutive 10 and 20 VDC step responses of the test run, as shown in Figure 40. The linear regression trendline of the direct current in the 30 min measurement period gave an estimate for the current drift of $dI/dt = -1x10^{-12}$ A/s. The calculated leakage current, $2.2x10^{-9}$ A at the end of the 30 min period gave an estimate for the resistivity $\varrho = 9.1x10^{9}$ **Ω**m of the AlO1_70 sample under measurement conditions of 20.8 °C and 20% RH.

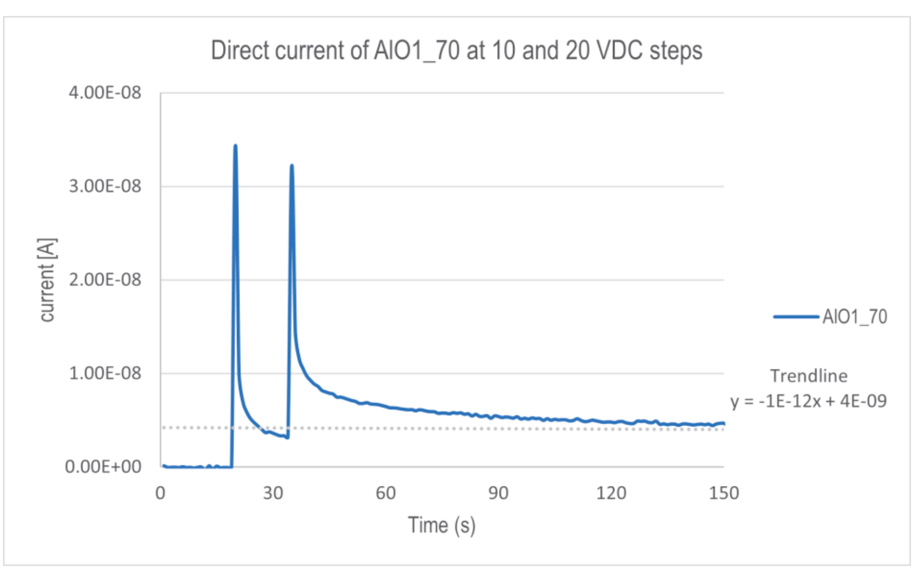


**Figure 40.** Leakage current of HVOF electrical insulation layer AlO1_70 in 10 and 20 VDC steps.

For comparison, the resistivities of the insulation layers were calculated from a 30 min average of the direct current measurements at 20 VDC performed at 21 °C and 20% RH. The results are shown in Figure 41. The resistivity of 70 µm AlO1_70 and AlO5_70 coatings was on the same level of $1 \times 10^{10}$ Ωm. The 200 µm AlO5 and AlO27 coatings possessed two decades lower resistivity but there was also much more current drift present, which can be seen from the values of the standard deviations in Figure 41. The lowest values for resistivity in relation to thickness were measured for the AlO27 spinel coatings.

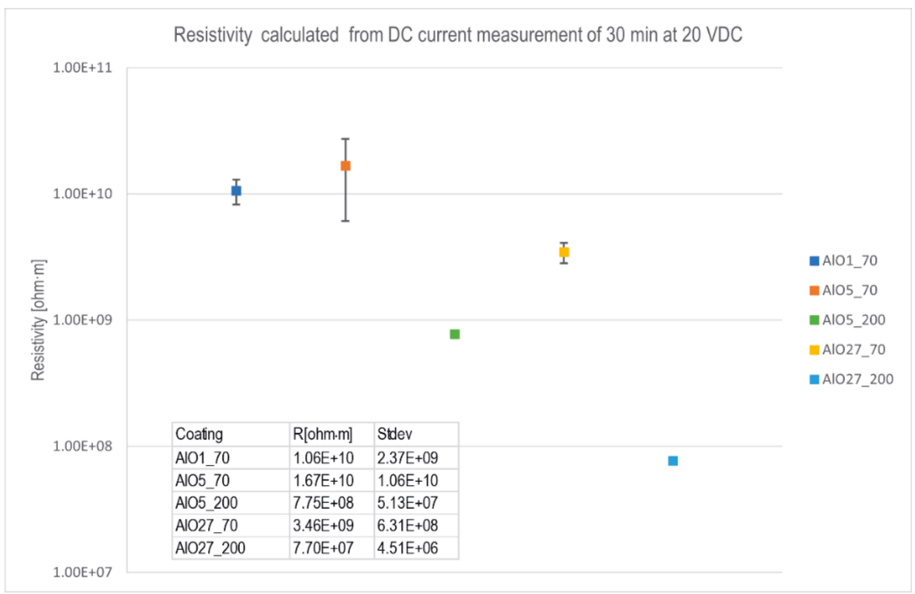


| Coating | R[ohm·m] | Stdev |
|---|---|---|
| AlO1_70 | 1.06E+10 | 2.37E+09 |
| AlO5_70 | 1.67E+10 | 1.06E+10 |
| AlO5_200 | 7.75E+08 | 5.13E+07 |
| AlO27_70 | 3.46E+09 | 6.31E+08 |
| AlO27_200 | 7.70E+07 | 4.51E+06 |

**Figure 41.** Resistivity of HVOF- and APS-deposited electrical insulation layers calculated from 30 min average of leakage current measurements at 20 VDC.

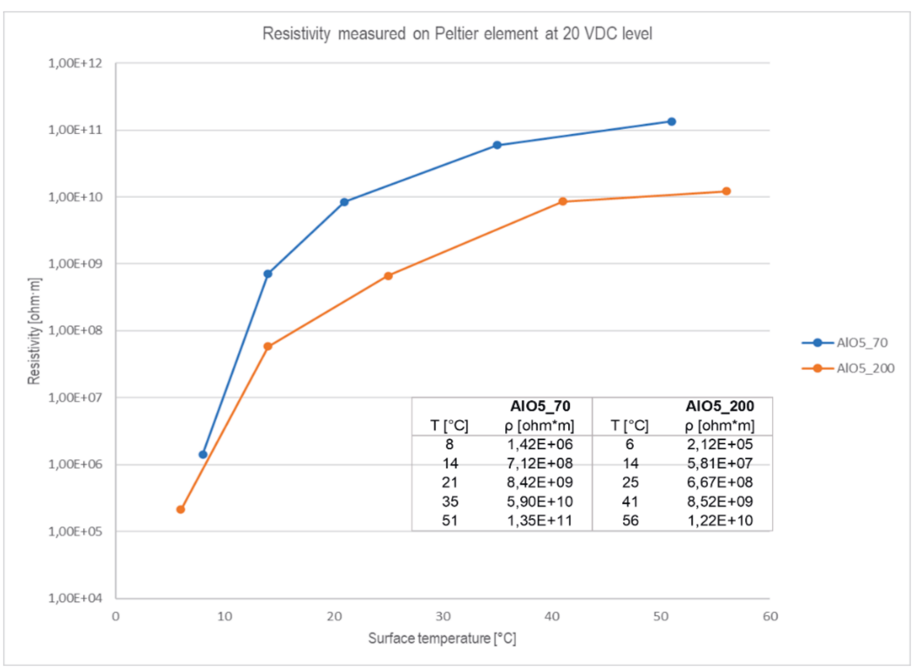


**Figure 42.** Resistivity of AlO5_70 and AlO5_200 samples measured on Peltier element in temperature range +5 °C to +55 °C.

The first assumption was that the drift in the leakage current was caused by absorption of water in the porous laminar structure of the thermal spray coatings. Therefore, the direct current measurements were repeated with two coating thicknesses of AlO5_70 and AlO5_200 on a Peltier heating element, which enabled the adjustment of the surface temperatures of +5 °C – +55 °C under ambient air conditions of 21 °C and 20% RH. The measurement set-up is shown in Figure 27. The experiment was performed by first cooling the AlO5 samples to below +10 °C and then, after temperature stabilization, slowly heating up to + 55 °C. Resistivity increased by five decades similarly in both AlO5_70 and AlO5_200 insulation layers during the temperature change from +5 °C to +55 °C.

The capacitances of the thermal spray coatings were measured between the Ti6Al4V electrode and the cantilever beam with an Amprobe LCR55A. Table 4 summarizes the measured capacitance values and relative permittivity of the coatings at 21 °C and 20% RH. The relative permittivity $\varepsilon_r$ was calculated from the ratio $C_m/C_o$, where $C_m$ is the measured value of capacitance, $C_o = \varepsilon_o \cdot A/d$ is the geometrical capacitance

of the sample at vacuum permittivity $\varepsilon_o$, A is the electrode area 10x10 $mm^2$ and d is the coating layer thickness. The values of relative permittivity were higher than the values found from the literature for sintered aluminium oxide [44].

**Table 4.** Capacitance and relative permittivity of thermal spray electrical insulation layers measured at 21 °C and 20% RH.

| Coating | Capacitance [pF] | Relative permittivity $\varepsilon_r$ at 1kHz |
|---|---|---|
| AlO1_70 | 196 | 15.5 |
| AlO5_70 | 189 | 14.9 |
| AlO5_200 | 92 | 20.8 |
| AlO27_70 | 201 | 15.9 |
| AlO27_200 | 99 | 22.4 |

The measurements were repeated on a Peltier element. The samples were first cooled to below +10 °C in ambient air conditions, then after stabilization of the surface temperature they were slowly heated up to + 50 °C over a period of 10 minutes. Figure 43 shows the change in capacitance measured as a function of temperature. Increase capacitance was seen with all the thermal spray insulation layers at temperatures below +15 °C. This was assumed to be caused by condensed humidity, as in the resistivity changes of APS AlO5 samples shown in Figure 42. The change in capacitance was compared to a PVD aluminium oxide coating of 5 μm in thickness deposited on 90MnCrV8 disc sample of 22 mm in diameter. The PVD_AlO3_5 aluminium oxide coating used as a reference (see Figure 43) possessed a nearly constant value of capacitance of between1.37-1.40 nF over the temperature range of +5 °C to +55 °C.

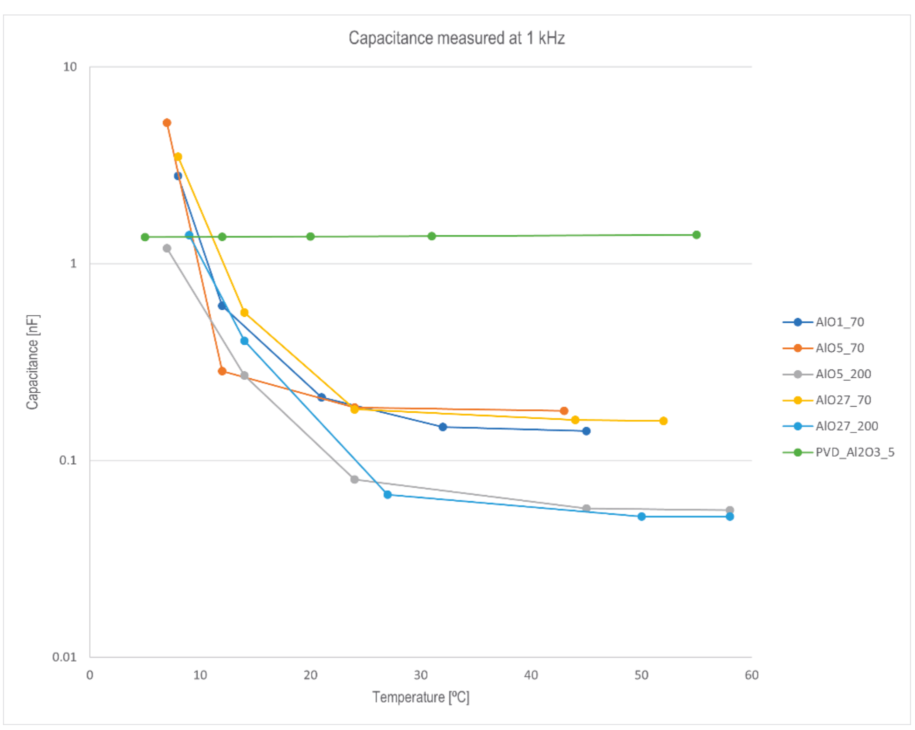


**Figure 43.** Capacitance of thermal spray coatings measured with an Amprobe LCR55A on a Peltier element as a function of substrate temperature in ambient air conditions of 21 °C and 20% RH.

The effect of the change in impedance according to formula (2) on capacitance $C_m$ measured with Amprobe LCR55A can be seen in Figure 43. The parallel impedance is temperature-sensitive according to formula (3), caused by the dissipation of space charge polarization. The value of capacitance was considered closer to the real value $C_r$ at the high end of the temperature range where the leakage current is the lowest. Table 5 lists the measured capacitance and calculated relative permittivity of the thermal spray samples at +50 °C, i.e. the high end of the temperature range. The capacitances were reduced when compared to the values measured at room temperature due to the decrease in leakage current and parallel impedance. Accordingly, the reduction of relative permittivity strongly indicates changes in the dielectric layer related to space charge polarization caused by humidity.

**Table 5.** Capacitance and relative permittivity of thermal spray coatings at +50 °C.

| Coating | Capacitance [pF] | Relative permittivity $\varepsilon_r$ at 1kHz |
|---|---|---|
| AlO1_70 | 141 | 11.2 |
| AlO5_70 | 179 | 14.2 |
| AlO5_200 | 56 | 12.7 |
| AlO27_70 | 159 | 12.6 |
| AlO27_200 | 52 | 11.8 |
| PVD_Al2O3_5 | 1401 | 7.9 |

The values of relative permittivity at +50 °C of the thermal spray coatings were closer to the values reported for sintered aluminium oxide [44]. The thermal spray coatings possessed a higher relative permittivity value than the reference PVD aluminium oxide. The reason is the nearly constant and much lower leakage current in PVD aluminium oxide over the measured temperature range than with the thermal spray coatings. The APS-deposited coatings possessed the highest values of relative permittivity, which is assumed to be related to the porosity and roughness of the coatings. It was seen with all the thermal spray coatings in direct current measurements that the drift in the leakage current was related to the electric field. This according to formula (3), is related to the imaginary part $\varepsilon_r'$ of complex permittivity $\varepsilon_r^*$ with some originating from the space charge polarization. Further studies were conducted with HVOF-deposited aluminium oxide layers.

### 7.2.3 Leakage current in HVOF-deposited $Al_2O_3$ coatings

The HVOF-deposited AlO1_70 coating possessed the lowest surface roughness of the thermal spray coatings and the quickest settling of the leakage current of the thermal spray coatings tested, as shown in Figure 39. The performance of AlO1_70 was further compared to the 40 µm AlO1_40 coating in the three consecutive 200 VDC step runs but the reduction of thickness did not bring further improvement compared to AlO1_70. Therefore, AlO1_70 was selected for further studies.

The first assumption for the reason for the drift in the leakage current was the space charge polarization caused by adsorbed water. Therefore, the direct current measurement was repeated with a second set of AlO1_70 coatings. The cantilever

beam samples were cleaned using the same procedure in an ultrasonic isopropanol bath and dried with pressurized air, but this time kept in a dry cabinet at 35 °C and 5% RH for 4 days before the deposition of the Ti6Al4V electrode and direct current measurement. Figure 44 indicates the decrease in the leakage current gained with the second set of samples in the direct current measurement at 200 VDC as a comparison to the first test shown in Figure 38. The reduction in the direct current is by factor of 20 in the first step run, and in the consecutive step runs 2 and 3, the decrease is smaller than with the first experiments, shown in Figure 38.

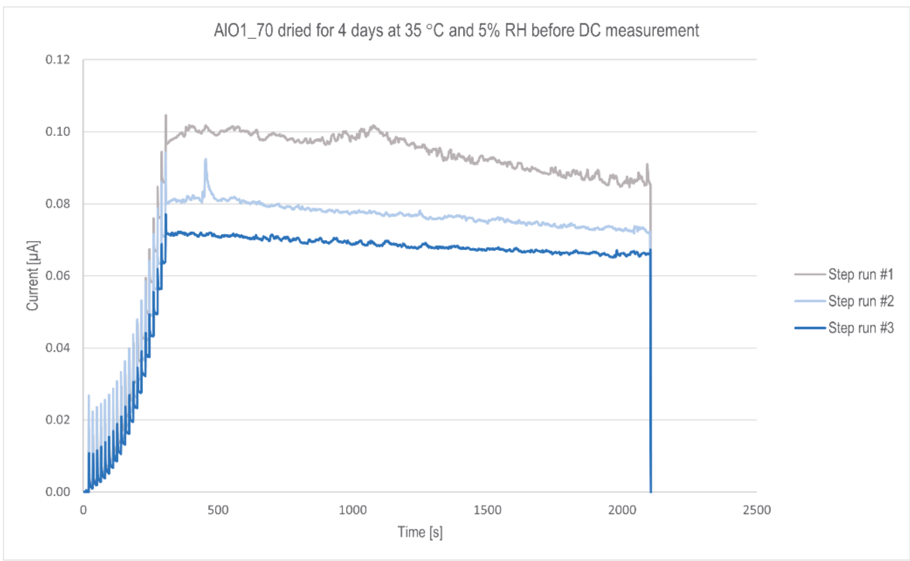


**Figure 44.** AlO1_70 sample kept for 4 days at 35 °C and 5% RH before leakage current measurement at 200 VDC.

The experiment indicated that drying had altered the sample more than the low temperature processing of the sample at $1x10^{-5}$ mbar vacuum during the deposition of Ti6Al4V electrodes.

**Figure 45.** AlO1_70 sample exposed for 3h at 20 °C and 50% RH before leakage current measurement at 200 VDC.

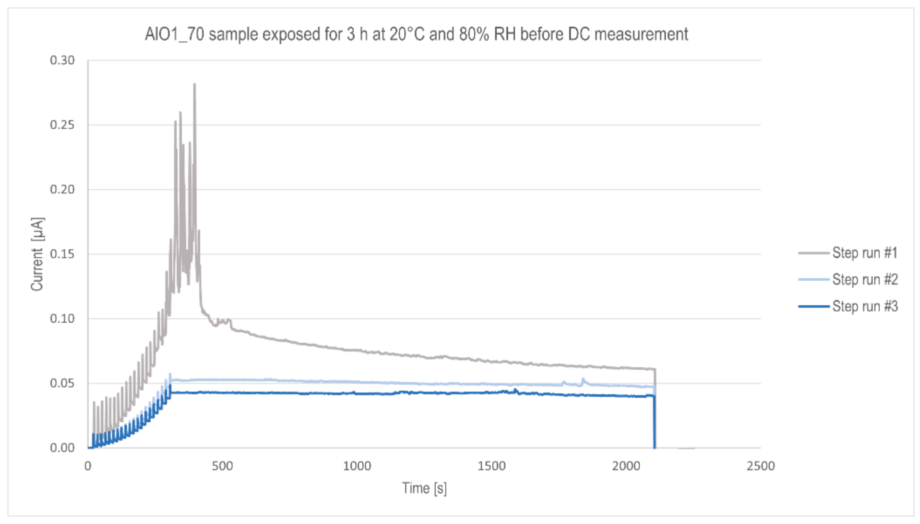


**Figure 46.** AlO1_70 sample exposed for 3h at 20 °C and 80% RH before leakage current measurement at 200 VDC.

The study was continued by exposing the dried sample for 3 hours under different temperature and humidity conditions in a climatic cabinet before direct current measurement. The measurements were repeated at a room temperature of 20 °C and 20% RH. The exposure at 20 °C and 50% RH for 3 hours did not increase the leakage current in the sample, as shown in Figure 45, when compared to the sample kept at dry conditions for 4 days shown in Figure 44. The first real change was seen with the second exposure at 20 °C and 80% RH, see Figure 46. The instability in the leakage current at the beginning of the 200 VDC level is assumed to be caused by condensed water on the surface of the sample, which after evaporation led to a more stable drift in the leakage current. The study was continued with the third exposure at an elevated temperature of 40 °C and 80% RH, shown in Figure 47. The leakage current increased by a factor of 6 when compared to the initial state of the sample shown in Figure 44, but it was factor 3 lower than the current in AlO1_70 sample of the first experiment shown in Figure 38.

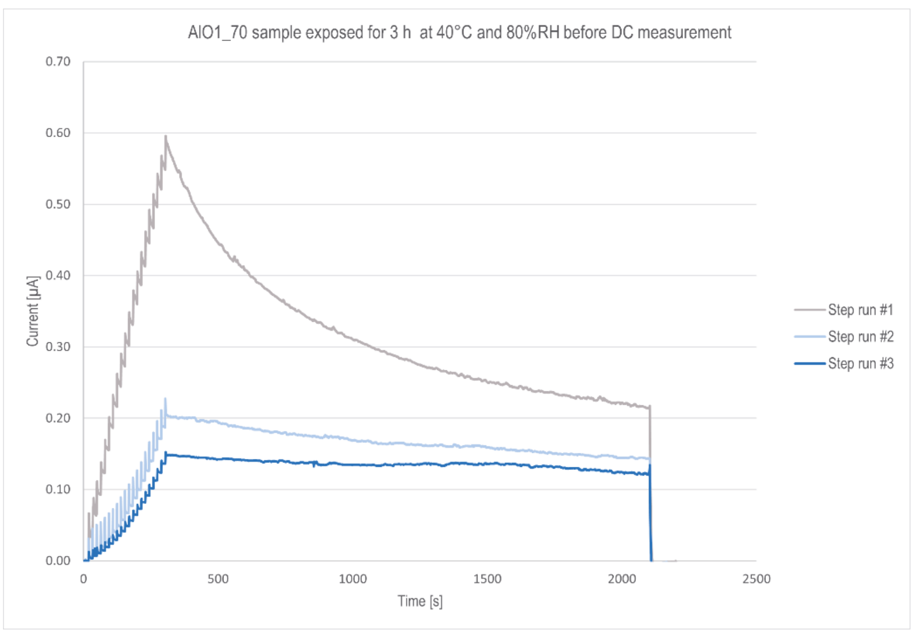


**Figure 47.** AlO1_70 sample exposed for 3h at 40 °C and 80% RH before leakage current measurement at 200 VDC.

The results depicted in Figures 45–47 indicate a clear correlation in leakage current of the samples exposed to humidity at elevated temperature, but the level of the measured leakage current was only one third of the current measured for the first set of AlO1_70 samples, as shown in Figure 38.

The exposure was repeated three more times with the same sample at a temperature of 40 °C and 80% RH for three hours to study the current drift. This time the direct current measurement was performed by reversing the 200 VDC voltage polarity after every period of 5 min to study the influence of polarization and the symmetry in the charge transfer under reversed conditions with the HVOF aluminium oxide layer. Figure 48 depicts the leakage currents after the second (grey line) and the third (blue line) exposure treatment. Because of the cumulative exposures, the direct current reached 3 μA at the 200 VDC level, which is a factor of 1.5 higher when compared to the first AlO1_70 step run shown in Figure 38. Interestingly, the current symmetry was more on the positive polarity and the polarization current was stronger at + 200 VDC than at reversed polarity. The phenomenon was present during the first four to five reversed cycles but after the asymmetry was more levelled out. The asymmetry is presumably influenced by the humidity profile in the aluminium oxide layer. The drift in the leakage current had different time constants, depending on the voltage polarity. During the cycle of positive polarity the drift in leakage current was much higher and water was more effectively removed from the dielectric layer, seen in reduction of the leakage current compared with the situation at reversed polarity. Reversing polarity forced the water to move back and forth in the dielectric layer, which increases the space charge polarization time seen in the envelope of the direct current level. During 5 minutes at +200 VDC polarity, the leakage current was reduced to half of the peak value, but the current envelope was reduced to half only after 60 minutes.

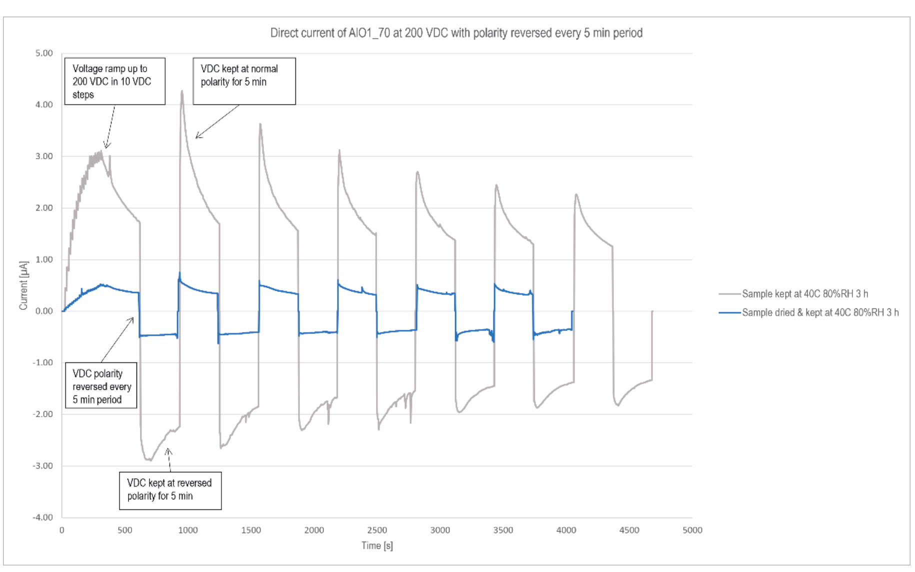


**Figure 48.** Leakage current at 200 VDC of AlO1_70 sample measured when voltage polarity was reversed at 5 min intervals.

The AlO1_70 sample was dried for 66 hours at +35 °C and 5% RH before the third exposure of 3 hours at +40 °C and 80% RH. The measured direct current in Figure 48 was more constant on a level of 0.4 µA and symmetric at reversed polarity but no significant decay was seen in the leakage current envelope. The nearly constant and high level of leakage current indicated the material had become more conductive. The optical study of the sample afterwards revealed the reason as corrosion spots in the white aluminium oxide layer, which can be seen in Figure 49. Anodic corrosion in the mild steel substrate had caused diffusion of iron oxides into the aluminium oxide layer influencing the change in resistivity.

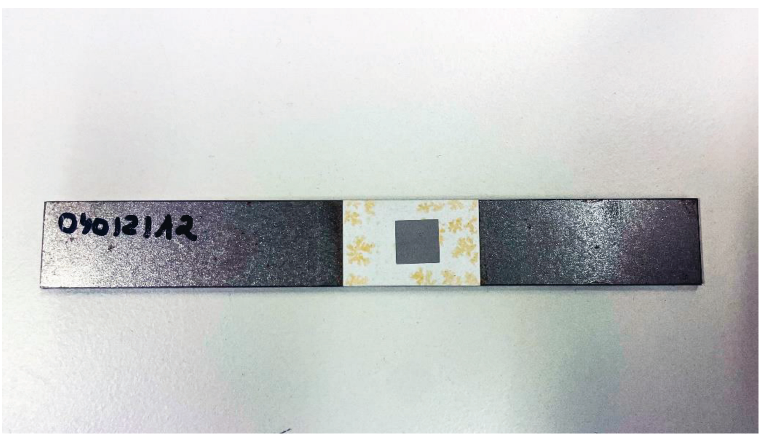

**Figure 49.** HVOF AlO1_70 sample after three exposures to conditions of 40 °C and 80% RH.

The study was continued with a new AlO1_70 sample from the batch which was kept at first for 4 days and then additional 66 hours in the dry cabinet at 35 °C temperature and 5% RH before performing direct current measurement at 200 VDC polarity, reversed after every 5 minutes. The charge current peaks shown in Figure 50 during the voltage ramp-up to 200 VDC are clearly visible. At 200 VDC level leakage current was very constant in the sample. Resistivity calculated from the leakage current of the AlO1_70 insulating layer was $9.3 \times 10^{10}$ Ω measured after the voltage ramp-up to 200 VDC. The space charge polarization was much faster after the voltage polarity was reversed than the earlier sample exposed to humidity.

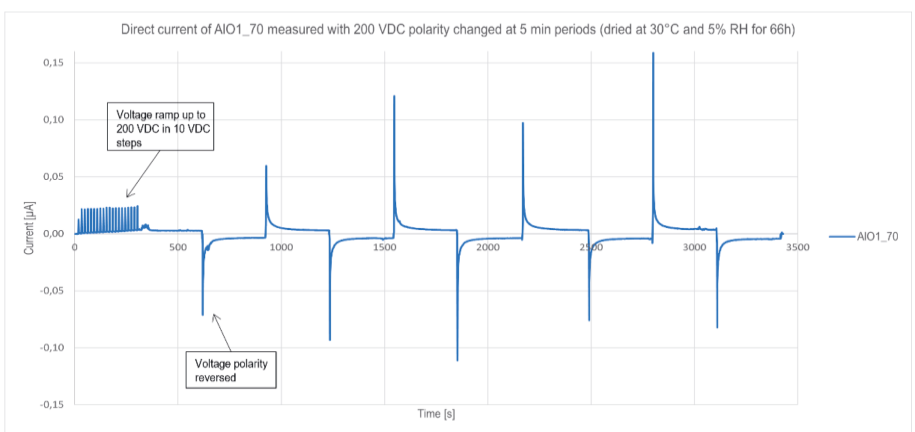


**Figure 50.** Leakage current measured of the dried AlO1_70 sample at 200 VDC when polarity was reversed at 5 min intervals.

The measurements of the first set of HVOF AlO1_70 samples performed at 21 °C and 20% RH showed a higher level of leakage current than the AlO1_70 sample, shown in Figure 47, exposed at 3 hours in 80% RH humidity. Therefore the test was repeated with a new sample AlO1_70 from the first set of samples. The direct current measurement at 200 VDC shown in Figure 51 was performed at 21.5 °C and 40.4% RH; otherwise all the handling of the samples was the same. The time difference between the measurements was a year. The result indicated that the level of leakage current had reduced to one quarter when compared to the first measurement with the AlO1_70 sample, as shown in Figure 38.

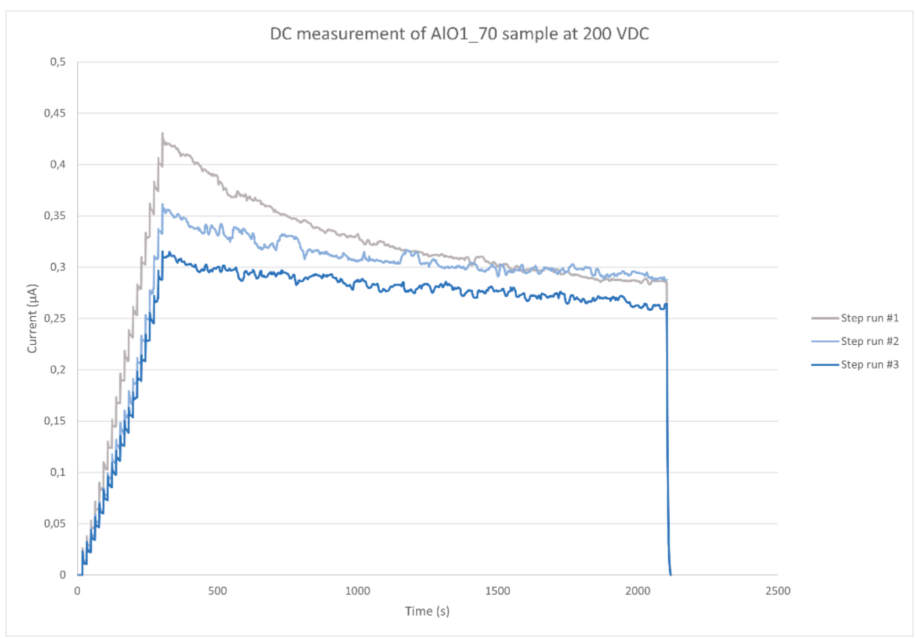


**Figure 51.** Leakage current measurement at 200 VDC of the second AlO1_70 sample at 21.5 °C and 40% RH.

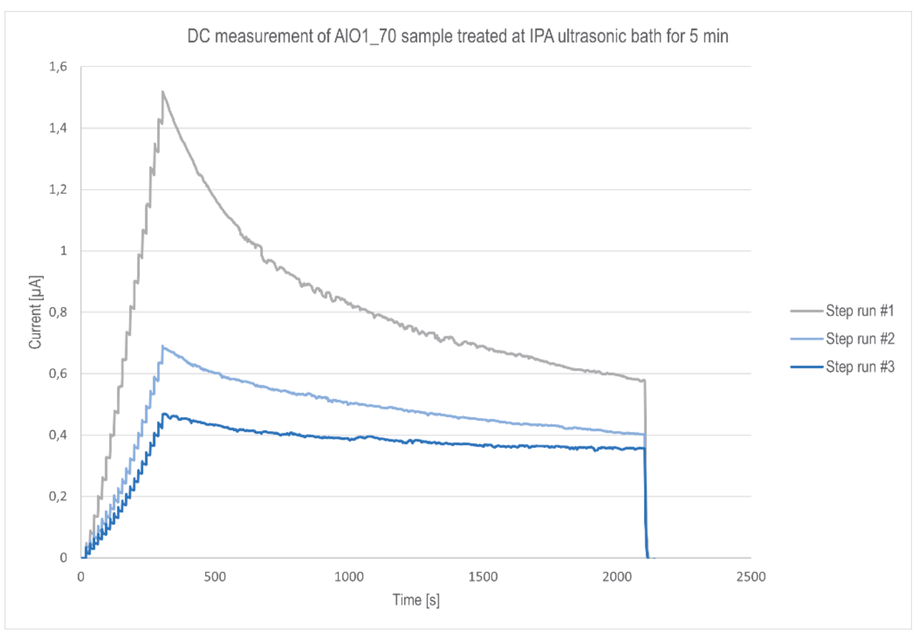


**Figure 52.** Leakage current measurement at 200 VDC of the second AlO1_70 sample measured at 21 °C and 46% RH after treatment in an IPA ultrasonic bath for 5 min.

It was presumed from the study that something had evaporated from the sample causing the reduction in the level of leakage current. For the purpose the handling of the AlO1_70 sample was repeated in an isopropyl alcohol (IPA) ultrasonic bath for 5 minutes, dried with pressurized air and placed in a vacuum at $1x10^{-5}$ mbar for 2 hours before repeating the direct current measurement. The idea was to simulate the handling of the AlO1_70 sample of the first experiment. The step runs seen in Figure 52 of the direct current measurement performed at 21.7 °C and 46% RH were very similar to the first experiment with AlO1_70, shown in Figure 38. From the result, it was concluded that there had been adsorption of IPA in the first AlO1_70 aluminium oxide sample which did not evaporate during drying with pressurized air nor during exposure in vacuum.

## 7.3 Influence of sealant resin on electrical resistance of APS $Al_2O_3$ coatings measured in humid conditions.

The APS coatings deposited by Oerlikon Metco from the feedstock materials of Metco Amdry 6060 and Metco 101NS on theS235JR cantilever beam were compared to earlier studied AlO5_70 and AlO5_200 coatings. The electrical resistance of the coatings, shown in Figure 53, was studied both from as-deposited from the feedstock materials without post-treatment and as impregnated with a solvent-free, two-component resin solution S106-049 sealant.

| Cantilever beam samples | Sample code | Thermally sprayed coating | Powder | Thickness (µm) | Sealant |
|---|---|---|---|---|---|
| | 21C0003 + sealer | $Al_2O_3$ | Amdry 6060 | 255 | S106-049 |
| | 21C0003 | $Al_2O_3$ | Amdry 6060 | 255 | |
| | 21C0005 + sealer | $Al_2O_3$+ 3%$TiO_2$ | Metco 101NS | 264 | S106-049 |
| | 21C0005 | $Al_2O_3$+ 3%$TiO_2$ | Metco 101NS | 264 | |

**Figure 53.** APS samples impregnated with two-component sealant for the study of dielectric properties.

The standard cleaning procedure of 5 min ultrasonic cleaning in isopropanol and drying with pressurized air was performed on the samples before the deposition of the Ti6Al4V contact electrodes.

The earlier leakage current measurements for APS AlO5 coatings were performed on a Peltier-element between +5 °C and +55 °C, and under the ambient air conditions of 21 °C and 20% RH. The measurements with the 21C0003 and 21C005 coating variants were performed in a Vötsch VCL 4003 climatic test cabinet to enable simultaneous control of temperature and humidity under the measurement conditions, and the possibility to measure several samples at the same time. The simultaneous measurement of the coatings was performed using the resistance measurement function of an Agilent 3497A data logger, which has a maximum measurement range of up to $1.2x10^8$ Ω. The substrate temperature was measured with a type K thermocouple pair fixed on the cantilever beam surface of 21C005 + sealant sample with Kapton tape, as shown in Figure 54.

The resistance measurements were performed with contact wiring of nickel-plated 26 AWG copper and PTFE-shielded leads glued on the electrodes and the cantilever beam steel substrates with Chemtronics CW2400 conductive epoxy, as shown in Figures 54 and 58. Curing of the glue at 100 °C for 30 min also acted as a drying process for the APS samples.

**Figure 54.** Placing of APS samples in resistance measurement with type K thermoelement in Vötsch VCL 4003 climatic test cabinet.

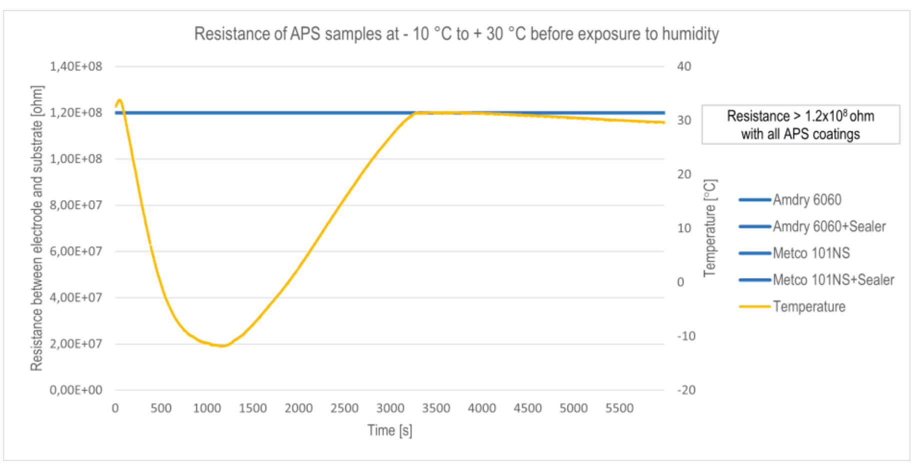


**Figure 55.** Electrical resistance of APS samples measured between - 10 °C and + 30° C before exposure to humidity.

Before exposure to humidity, the resistances of the 21C0003 and 21C0005 samples were measured in a temperature cycle from -10 °C to +30 °C. The yellow line in Figure 55 indicates the surface temperature on the cantilever beam during the measurement period. As expected, all the APS samples possessed resistance values above the measurement range of $1.2 \times 10^8$ Ω.

The study was continued with the humidity test shown in Figure 56. During the temperature ramp-up from +21.7 °C (RT) to +40 °C in the climatic chamber, the APS Amdry 6060 and Metco 101NS samples excluding sealant responded with a fast decrease in electrical resistance while the substrate temperature was below the dew point temperature of 35.9 °C. The influence of condensed water on the reduction in electrical resistance was three orders of magnitude measured for the unsealed APS coatings. A similar reduction in resistance had already been seen with the AlO5 samples, see Figure 42. When the substrate temperature of 40 °C was reached at 80% RH, the electrical resistance of Amdry 6060 on 21C0003 stabilized to a level of $3.3 \times 10^7$ Ω and that of Metco 101NS on 21C0005 to a level of $2.7 \times 10^7$ Ω. In the next step, the relative humidity was reduced to 40%, which caused a rapid increase over the detection level of $1.2 \times 10^8$ Ω in resistance. The decrease in electrical resistance was reversible when the humidity was raised back to 80% RH. The electrical resistance of both samples, Amdry 6060 with sealant on 21C0003 and Metco 101NS

with sealant on 21C0005 were over the level of 1.2x10⁸ Ω in all humidity conditions during the measurement.

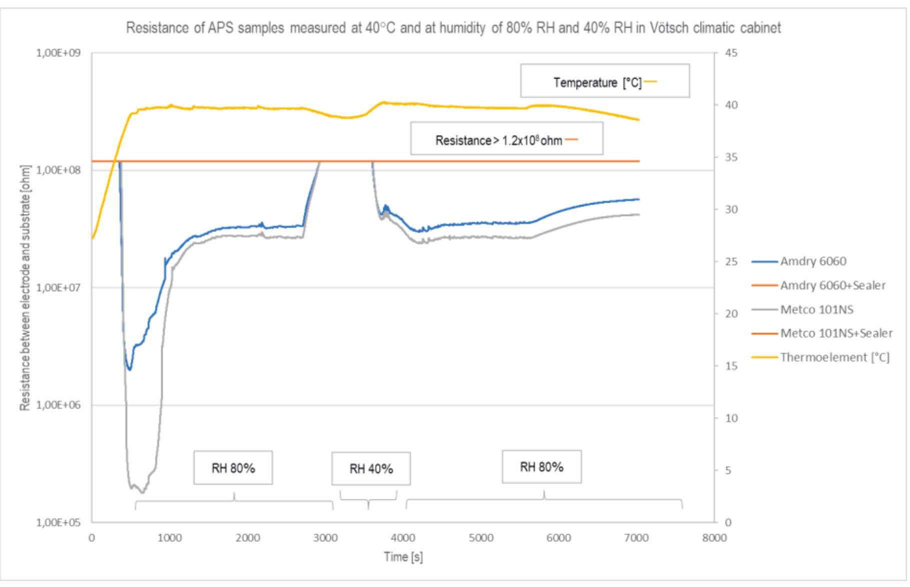


**Figure 56.** Electrical resistance of APS coatings at 40 °C in a cyclic change of humidity from 80% RH to 40% RH and back to 80% RH.

The samples were left overnight in a closed climatic chamber with the power switched off under conditions of an absolute humidity of 40.88 g/m$^3$ in the chamber. The measurement was continued after twelve hours, first by cooling the samples to -10 °C and then heating them up to +30 °C without ventilation in the chamber. During the cooling cycle, the decrease in electrical resistance was two orders of magnitude to a level of 1x10$^6$ Ω but returned to a level of 3.1x10$^7$ Ω with the Amdry 6060 sample and to a level of 2.2x10$^7$ Ω with Metco 101NS, as shown in Figure 57. The resistance level at 30 °C shown in Figure 56 was very similar to the values earlier measured with samples exposed in conditions of 40 °C and 80% RH. The resistance levels indicated a conductivity change in the coatings, which was considered as the start of anodic corrosion. Resistance values of the samples 21C20003 and 21C20005 with the sealant were over the detection limit and were unaffected by the temperature and humidity conditions.

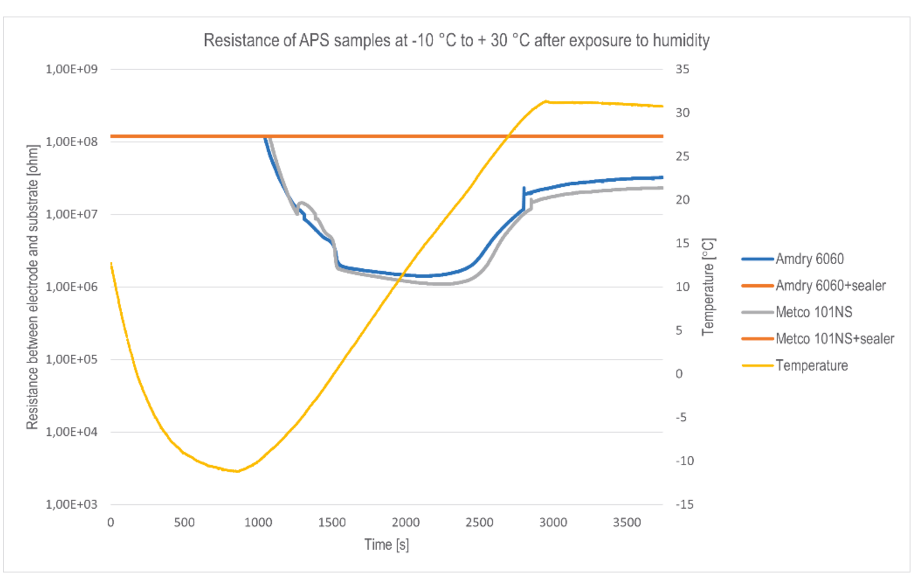


**Figure 57.** Electrical resistance of APS samples measured between -10 °C and +30 °C after exposure to 80% RH.

Visual inspection of the samples revealed that the corrosion process had started with the unsealed APS samples. Red iron oxide spots are clearly visible on the white Amdry 6060 aluminium oxide layer of sample 21C20003 in Figure 58. The samples with the S106-049 sealant were intact and without corrosion spots.

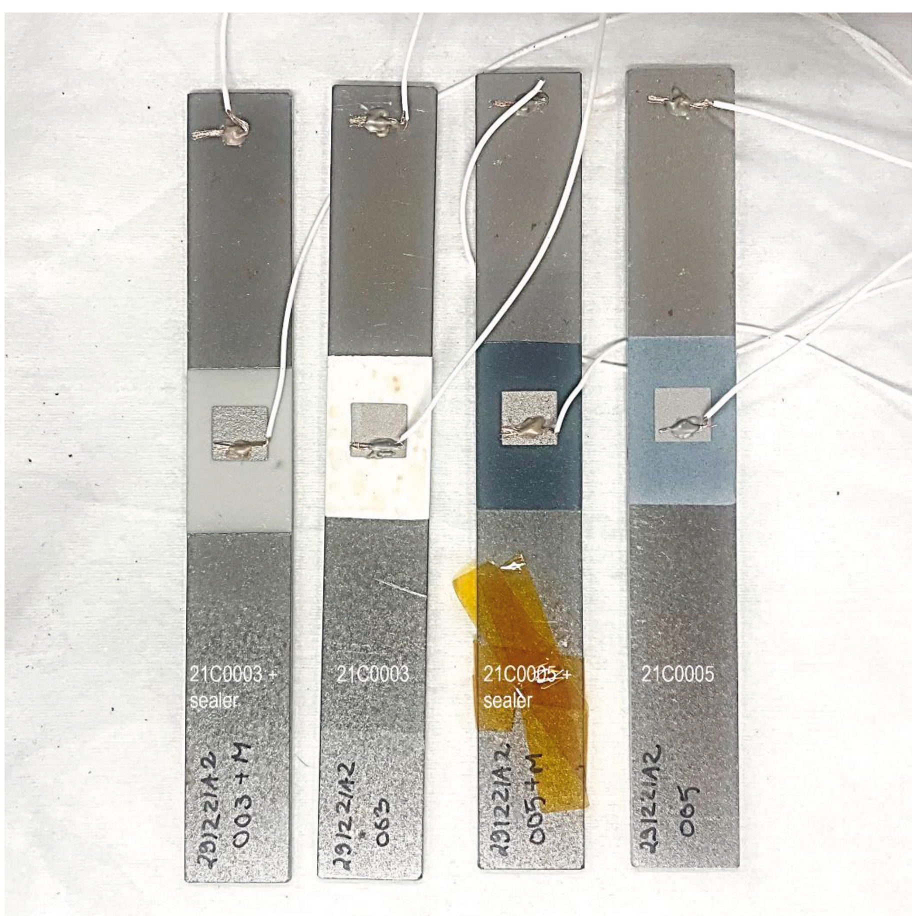


**Figure 58.** APS insulating samples on S235JR cantilever beam after the study of exposure to humidity.

## 7.4 Electrical insulation of S-HVOF-deposited $Al_2O_3$ coatings

The suspension-HVOF coatings (S-HVOF) shown in Figure 60 were deposited by Fraunhofer IWS on S235JR cantilever beams to study the electrical insulating resistance of the coatings with direct current measurement, seen in Table 2. The coatings were prepared from two experimental water suspensions, marked A and B. The feedstock material in suspension A consisted of sub-micrometre-sized particles of a high purity aluminium oxide > 99.9%. In suspension B, the feedstock material

consisted of micrometre-sized aluminium oxide particles with a purity of approx. 99.8 %. Deposition was carried out with a TopGun HVOF burner with ethene as fuel. The coatings were prepared with four nominal thickness ranges of 15–20 µm, 40–50 µm, 70–80 µm and 210–220 µm listed in Table 2. The samples with their measured coating thickness are shown in Figure 59.

| Sample | Code | Suspension | Measured thickness [µm] |
|---|---|---|---|
| | 210012TC | Suspension B<br>- µm particle size<br>- $Al_2O_3$ purity ca. 99.8% | 11.7 ± 2.5 |
| | 210013TC | | 47.0 ± 2.4 |
| | 210014TC | | 76.0 ± 4.1 |
| | 210015TC | | 214.7 ± 9.5 |
| | 210016TC | Suspension A<br>- sub-µm particle size<br>- $Al_2O_3$ purity > 99.9% | 221.7 ± 9.2 |
| | 200073TC | | 18.7 ± 2.5 |
| | 200075TC | | 54.3 ± 2.5 |
| | 200076TC | | 75.3 ± 4.2 |
| | 200077TC | | 211.3 ± 4.2 |

**Figure 59.** Suspension-HVOF coatings on S235JR cantilever beam samples for study of electrical insulation resistance with direct current measurement.

The roughness parameters of the S-HVOF coatings shown in Figure 60 and listed in Table 2 are an average of three consecutive measurements of each sample measured with a Dektak XT profilometer with a sweep length of 1.5 mm. The $R_z$ roughness of the coatings deposited from both suspensions A and B was on the same level, between 8 to 10 µm, as with the HVOF AlO1_70 and AlO1_40 samples but clearly smoother, half of the roughness of the APS coatings shown in Figure 29. A comparison between the suspensions showed that the coatings deposited from suspension B were smoother, except at a very thin coating thickness of 11.7 µm on sample 210012TC, shown in Figure 61. The results indicated that grit blasting of the substrate has a major effect on surface roughness with thin coatings. The comparison of values for peak and valley roughness in all the S-HVOF coatings indicated a slightly higher average peak roughness.

The S-HVOF coatings deposited from both suspensions were characterized by a dense microstructure. The cross-section images of the S-HVOF coatings prepared

from both suspensions were very similar in SEM. Thick 200 µm coatings of 210015TC and 210016TC were deposited with a NiCr bond coat to improve the adhesion of the aluminium oxide coating layer. A cross-section of 220 µm thick aluminium oxide sample 210016TC with a NiCr bond coat is shown in Figure 62. Isolated microcracks were observed in the layers deposited from suspension A. An SEM cross-section image of sample 200076TC deposited from suspension A revealed microcracks in the microstructure of the aluminium oxide layer, as shown in Figure 64.

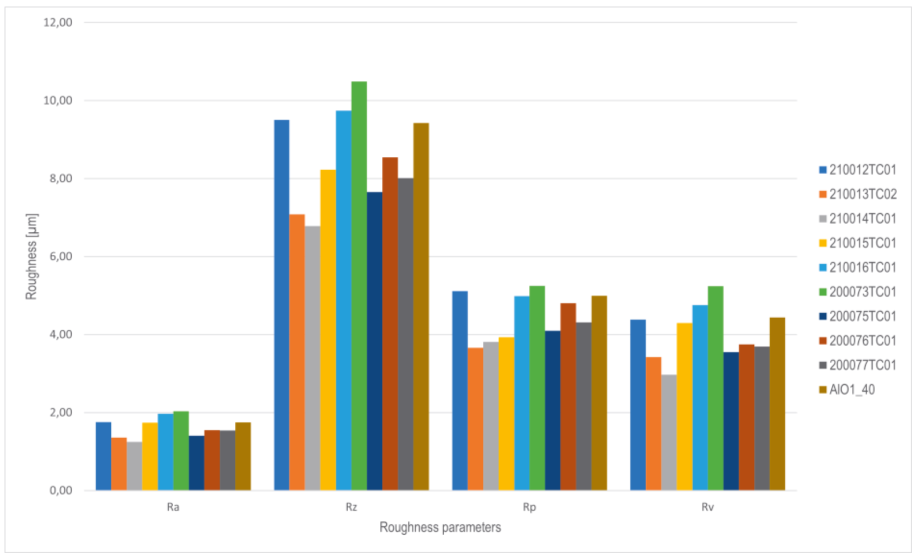


**Figure 60.** Measured average roughness ($R_a$), mean roughness depth ($R_z$), maximum peak ($R_p$) and maximum valley roughness ($R_v$) of S-HVOF coating samples in comparison to 40 µm HVOF AlO1_40 as a reference sample.

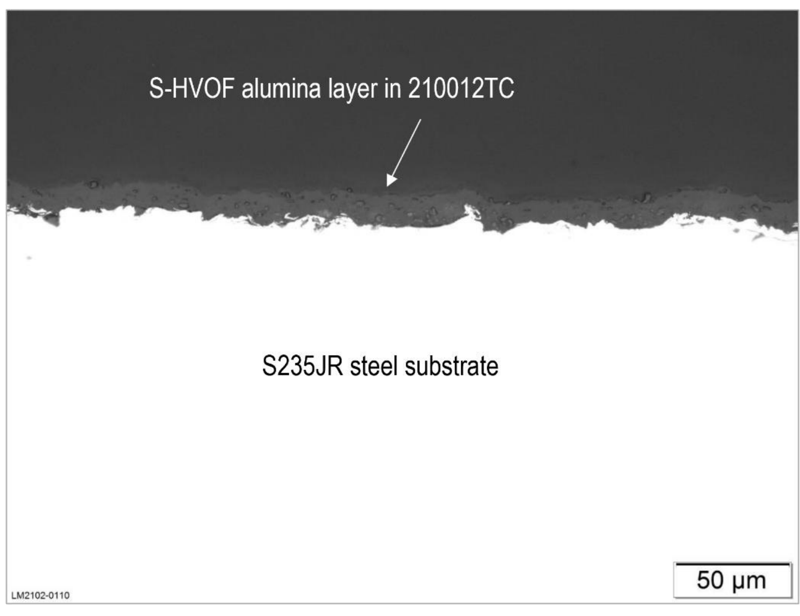


**Figure 61.** Optical cross section image of 12 µm thick S-HVOF aluminium oxide layer of 210012TC sample deposited from suspension B.

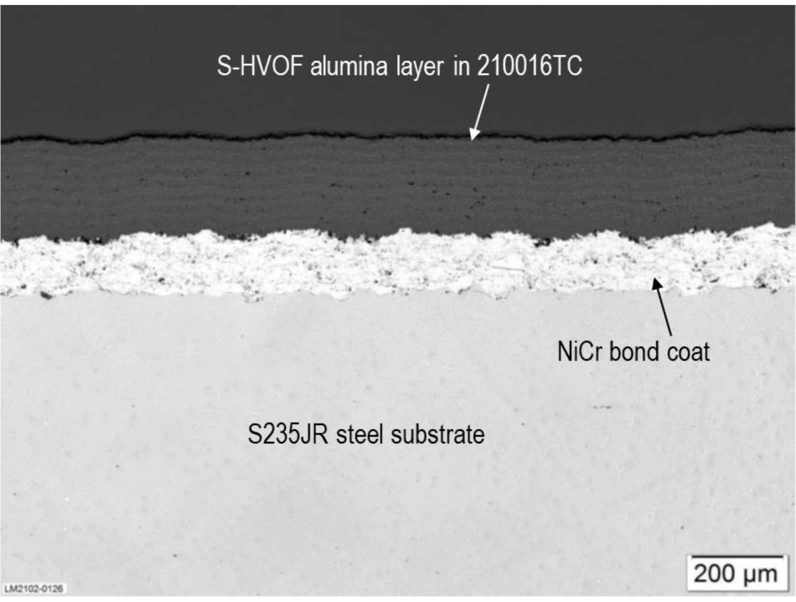


**Figure 62.** Optical cross section image of 220 µm S-HVOF aluminium oxide layer of 210016TC sample deposited from suspension A with NiCr bond coat.

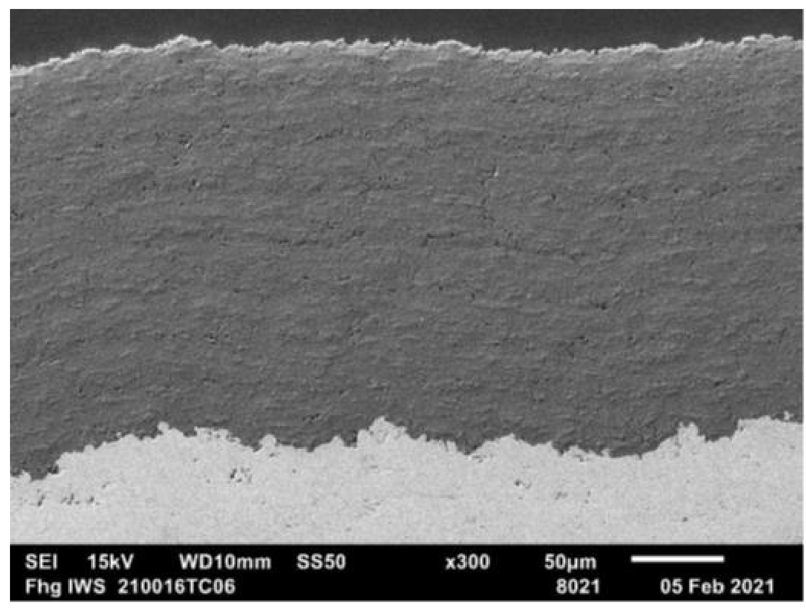


**Figure 63.** SEM cross section image of 220 µm S-HVOF aluminium oxide layer of 210016TC deposited from suspension A.

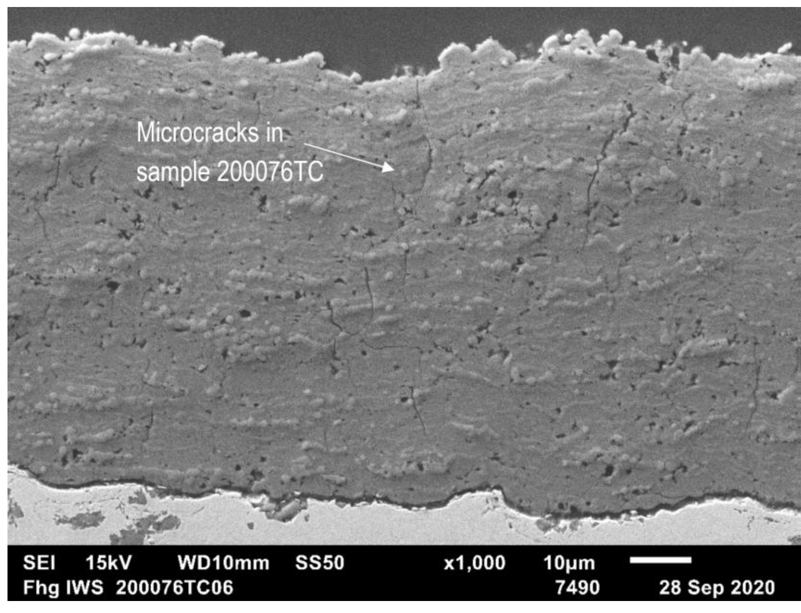


**Figure 64.** SEM cross-section image of 75 µm S-HVOF aluminium oxide layer of 200076TC deposited from suspension A.

### 7.4.1 Structure of Ti6Al4V contact electrodes deposited on S-HVOF $Al_2O_3$ insulating layers

Ti6Al4V contact electrodes with a nominal thickness of 250 nm and surface area of 10x10 $mm^2$ were deposited with a filtered cathodic vacuum arc at a deposition rate of 0.3 µm/h on S-HVOF thermal spray coatings on S235JR cantilever beam substrates. The average values of five consecutive resistance measurements performed as a two-point measurement of each sample are shown in Figure 65. The standard deviation σ of average resistances was ± 1.59 Ω including all the S-HVOF coatings. The samples deposited from suspension B had a lower average sheet resistance due to the lower surface roughness of the aluminium oxide layers than coatings deposited from suspension A. The average sheet resistance was 30 Ω for the samples deposited from suspension B. This was on the same level as the contact electrodes deposited on the 40 µm HVOF AlO1_40 layer used as a reference. The average sheet resistance of 44.7 Ω was measured for the coatings deposited from suspension A.

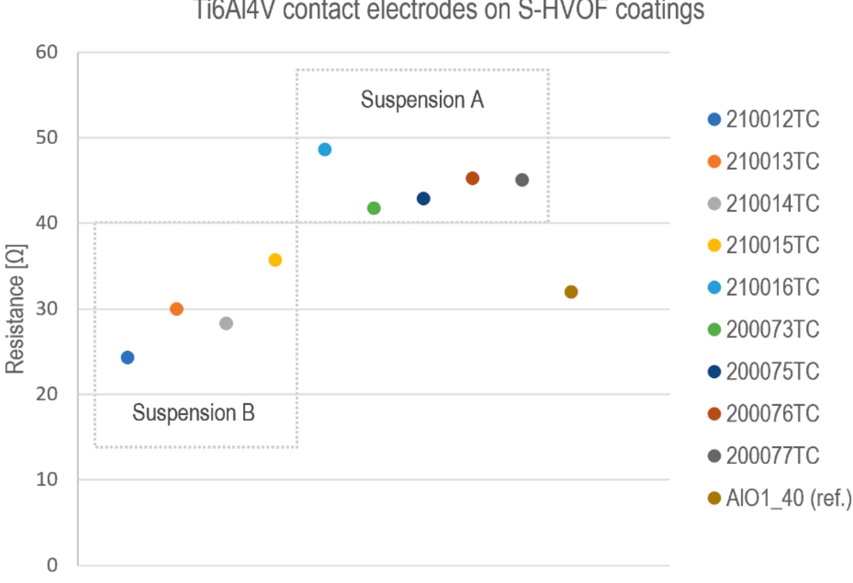


**Figure 65.** Sheet resistance of Ti6Al4V contact electrodes measured from S-HVOF aluminium oxide samples deposited from feedstock suspensions A and B.

### 7.4.2 Dielectric properties of S-HVOF-deposited $Al_2O_3$ layers

The S-HVOF samples were screened by ohmic measurement with a Wavetek 15XL multimeter (range up to 2000 MΩ) before the relative permittivity was determined from the measured capacitances with an Amprobe LCR55A. The measurement data of the samples is collected in Table 6.

Samples 210012TC and 200073TC possessed a very low value of resistance measured between the Ti6Al4V electrode and the S235JR cantilever beam. They also had the lowest thickness of the coatings, ≤ 20 µm. The thickness proved to be critical for electrical isolation with PVD deposited Ti6Al4V electrodes on the S-HVOF coatings on the steel substrate.

The relative permittivity of S-HVOF coatings was between 9 and 11, measured from the samples in the thickness range of 40 to 80 µm. This increased to 13–14 with the thicker coatings of 200 µm. The thickness dependence of permittivity is assumed to be caused by the planar geometry of the sample on the cantilever beam and the porous structure of the thermal spray coating with adsorbed water in the structure.

**Table 6.** Dielectric properties of S-HVOF coatings deposited from suspensions A and B

| Coating | Suspension | Nominal layer thickness [µm] | Resistance of electrode to substrate | Capacitance [pF] | Relative permittivity $\varepsilon_r$ at 1 kHz |
|---|---|---|---|---|---|
| 210012TC | B | 15 | 13 Ω | n.a. | |
| 210013TC | | 40 | >2000 MΩ | 216 | 9.8 |
| 210014TC | | 70 | >2000 MΩ | 134 | 10.6 |
| 210015TC | | 200 | >2000 MΩ | 61 | 13.8 |
| 210016TC | A | 200 | >2000 MΩ | 61 | 13.8 |
| 200073TC | | 20 | 8.6 kΩ | n.a. | |
| 200075TC | | 50 | >2000 MΩ | 177 | 10.0 |
| 200076TC | | 80 | >2000 MΩ | 126 | 11.4 |
| 200077TC | | 200 | >2000 MΩ | 60 | 13.6 |
| AlO1_40 (ref. HVOF) | | 40 | >2000 MΩ | 217 | 9.8 |

### 7.4.3 Leakage current in S-HVOF-deposited $Al_2O_3$ coatings

Leakage current measurements of the S-HVOF samples were performed at a voltage level of 200 VDC, as shown in Table 6. The samples were kept for 24 hours in a dry cabinet at 35 °C temperature and 5% relative humidity prior to measurement. Measurements were performed at 20 °C ambient temperature and at a relative humidity which varied from 6.4% RH to 20.1% RH. Three consecutive 30 min step runs were accomplished for every sample. The charge current peaks of the direct current measurements during the ramp-up phase to 200 VDC were clearly visible.

The level of leakage current was found to be very low with all the S-HVOF thermal spray aluminium oxide coatings prepared from both suspensions A and B. The leakage current measured from the samples was already very close to the noise voltage level of the measurement set-up. Therefore, resistivity was calculated as an average of the three consecutive 30 min direct current step runs of each sample performed at 200 VDC. The average resistivity for the 50 μm sample 200075TC deposited from suspension A was $9.2 \times 10^{12}$ Ωm with a standard deviation σ of $\pm 1.8 \times 10^{12}$ Ωm in measurement conditions of 19.7 °C and 6.4% RH, as shown in Figure 66. In comparison, the 40 μm AlO1_40 HVOF reference sample shown in Figure 67 possessed a resistivity of $3.5 \times 10^{11}$ Ωm with a standard deviation σ of $\pm 1.3 \times 10^{10}$ Ωm measured under similar conditions of 20.4 °C and 9.1% RH. The leakage current in samples deposited from suspension B was very similar to that of the measured HVOF reference. The 200 μm sample 210015TC shown in Figure 68 deposited from suspension B possessed a resistivity of $3.0 \times 10^{11}$ Ωm with a standard deviation σ of $6.5 \times 10^{9}$ Ωm under measurement conditions of 19.9 °C and 9.5% RH.

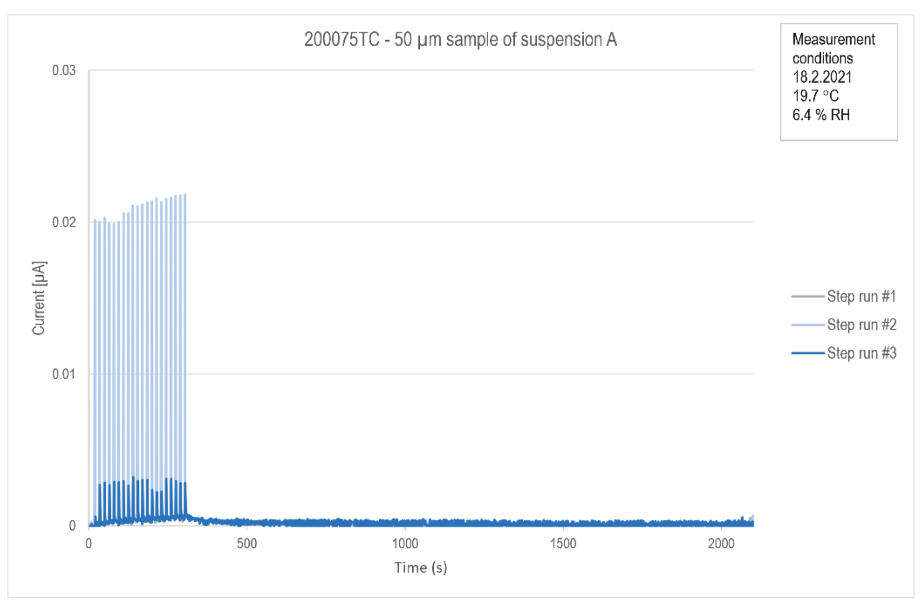


**Figure 66.** Leakage current measurement of 50 µm S-HVOF aluminium oxide sample 200075TC deposited from suspension A.

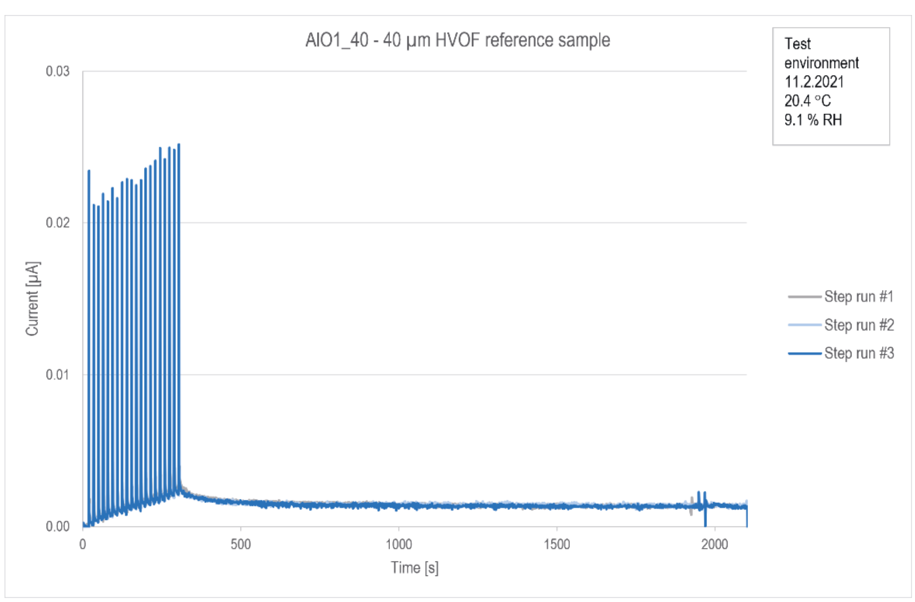


**Figure 67.** Leakage current measurement of 40 µm HVOF aluminium oxide reference sample AlO1_40.

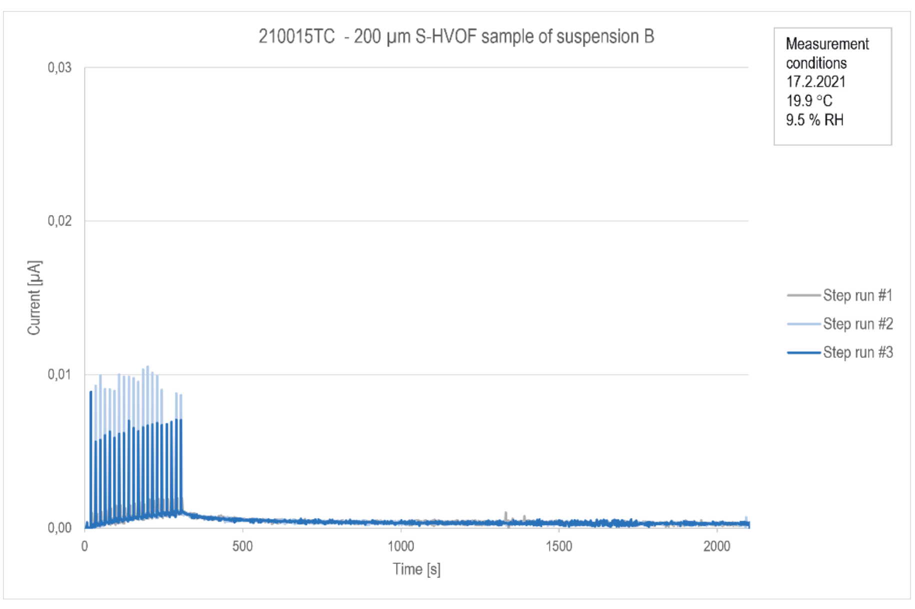


**Figure 68.** Leakage current measurement of 200 µm S-HVOF aluminium oxide sample 210015TC deposited from suspension B.

The overall resistivity of $2.0 \times 10^{11}$ Ωm of the S-HVOF coatings deposited from suspension B was lower than the resistivity of $2.9 \times 10^{12}$ Ωm of the coatings deposited from suspension A. Table 7 summarizes the resistivity data of the S-HVOF samples calculated from the leakage current measurements performed.

**Table 7.** Average resistivity of S-HVOF coatings calculated from leakage current measurements.

| Sample code | Suspension | Nominal layer thickness [µm] | Average resistivity [Ω·m] | Standard deviation [Ω] |
|---|---|---|---|---|
| 210013TC | B | 40 | $2.3 \times 10^{11}$ | $6.0 \times 10^{10}$ |
| 210014TC | | 70 | $7.7 \times 10^{10}$ | $2.3 \times 10^{10}$ |
| 210015TC | | 200 | $3.0 \times 10^{11}$ | $6.5 \times 10^{9}$ |
| 210016TC | A | 200 | $8.2 \times 10^{10}$ | $4.1 \times 10^{9}$ |
| 200075TC | | 50 | $9.2 \times 10^{12}$ | $1.8 \times 10^{12}$ |
| 200076TC | | 80 | $2.5 \times 10^{12}$ | $1.4 \times 10^{12}$ |
| 200077TC | | 200 | $4.8 \times 10^{10}$ | $3.4 \times 10^{9}$ |
| AlO1_40 (ref. HVOF) | | 40 | $3.5 \times 10^{11}$ | $1.3 \times 10^{10}$ |

Humidity had a strong effect on the measured resistivity of the S-HVOF coatings. The general trend with the decrease in resistivity at elevated humidity is seen in Figure 69, where the resistivity of S-HVOF coatings is depicted as a function of relative humidity in the measurement. The humidity caused a drift in the leakage current with the consecutive step runs and was clearly visible in the 70 μm sample 210014TC measured at 20.3 °C and 18.4% RH, as shown in Figure 70.

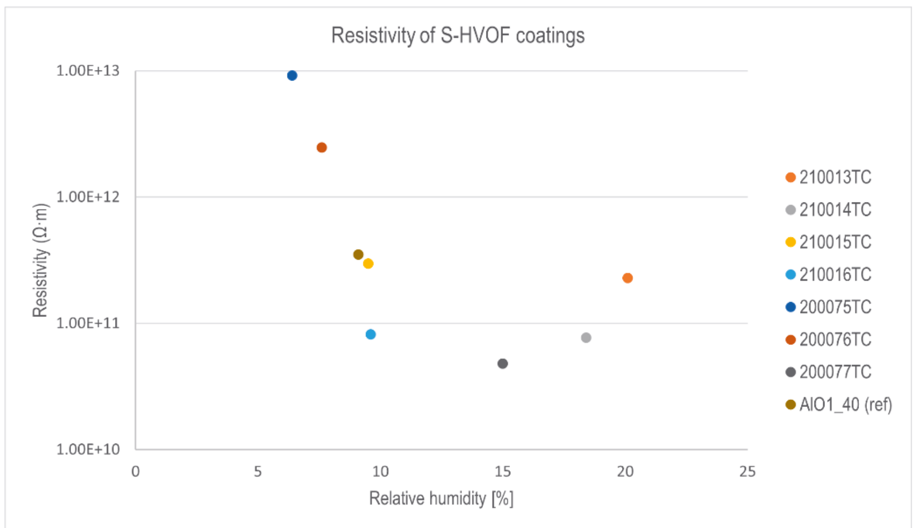


**Figure 69.** Resistivity of S-HVOF coatings measured under different humidity conditions.

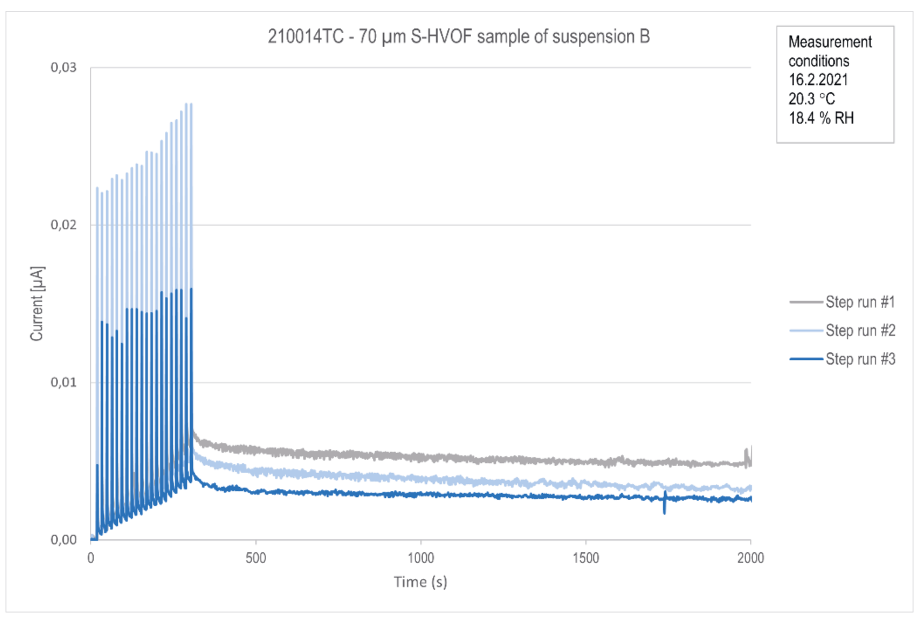


**Figure 70.** Leakage current of 70 µm S-HVOF aluminium oxide coating in three consecutive direct current measurements performed at 20.3 °C and 18.4% RH.

In the measurements of S-HVOF coatings deposited from both suspensions A and B showed lower leakage current and faster decrease compared to HVOF coatings measured at same conditions below 20% RH.

## 7.5 Performance of piezoresistive hard carbon thin films deposited on thermally sprayed HVOF and APS $Al_2O_3$ coatings

The direct current measurement of thermal spray aluminium oxide coatings showed promising high resistivity performance for electrical insulation and encouraged the study of the temperature and strain sensitivity of piezoresistive hard carbon thin films deposited on them. Experiments were performed to compare the properties to earlier measured samples deposited on a polyimide substrate. The mechanical performance of adhesion along with the fatigue resistance of HVOF aluminium oxide was studied in a bend test, as described in Chapter 6.3.3. with the piezoresistive carbon thin film on the cantilever beam sample.

### 7.5.1 Thermistor beta value of piezoresistive hard carbon thin films deposited on thermally sprayed HVOF and APS coatings

The thermistor properties of piezoresistive hard carbon thin films were studied for HVOF and APS samples of AlO1_70, AlO5_70, AlO5_200 and AlO27_200 coatings on S235JR cantilever beam samples. The patterned hard carbon films were deposited by vacuum arc discharge with a nominal coating thickness of 750 nm on the thermal spray insulating layers together with Ti6Al4V contact pads. Figure 71 shows the structure of the piezoresistive hard carbon thin film sensor with Ti6Al4V contact pads on the thermal spray layer. A piezoresistive hard carbon film of 5x10 $mm^2$ was deposited with 1 mm overlapping with the Ti6Al4V pads of 10x10 $mm^2$ to form a low contact resistance in the film. All the thin film layers were deposited by cathodic vacuum arc on the thermal spray layer. Contact leads were bonded with Chemtronics CW 2400 conductive epoxy (the grey dots in the image) on the Ti6Al4V contact pads for resistance measurement in an Agilent 34972 A datalogger. Temperature and strain sensitivity were measured as a change in the electrical resistance of the piezo-resistive element between the contact pads.

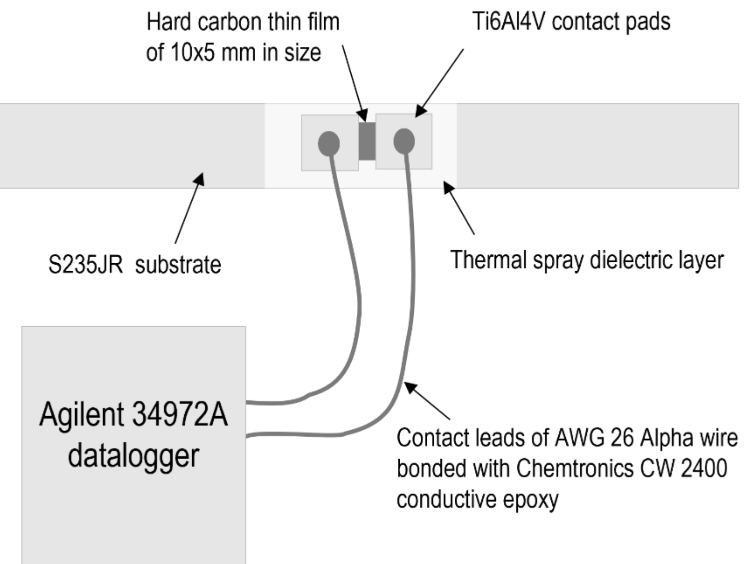


**Figure 71.** Resistance measurement of hard carbon thin film sensor structure deposited on HVOF and APS dielectric coatings on S235JR cantilever beams.

The electrical resistance of the samples was measured in a Vötsch VCL 4003 climatic cabinet at temperatures between -10 °C and +100 °C, as shown in Figure 72. The measurement temperature was raised in steps of 10 °C and kept constant for 15 minutes for each temperature step. A waiting time of 5 minutes for the temperature to stabilize was used before a 10-minute period of resistance measurement in each step.

**Figure 72.** Resistance measurement of piezoresistive hard carbon thin film thermistors on HVOF and APS insulating coatings to determine thermistor beta value.

The carbon thin films were deposited simultaneously in one batch on all the HVOF and APS dielectric layers. The thermistor beta value of the carbon thin film was determined from the resistance measurements performed, as shown in Figure 73. The average resistance $R_0$ of the carbon films on the thermal spray coatings was 80.6 kΩ with a standard deviation σ of 4.7 kΩ at 20 °C. The roughness of the thermal spray layers had an influence on the resistance level. The lowest resistance of the samples, 70.2 kΩ, was measured on the AlO1_70 layer, which also had the lowest roughness parameters measured, as shown in Figure 29. The second lowest resistance 70.6 kΩ at 20 °C was surprisingly measured with AlO27_70. This is why the resistance graphs of AlO1_70 and AlO27_70 overlap in Figure 73.

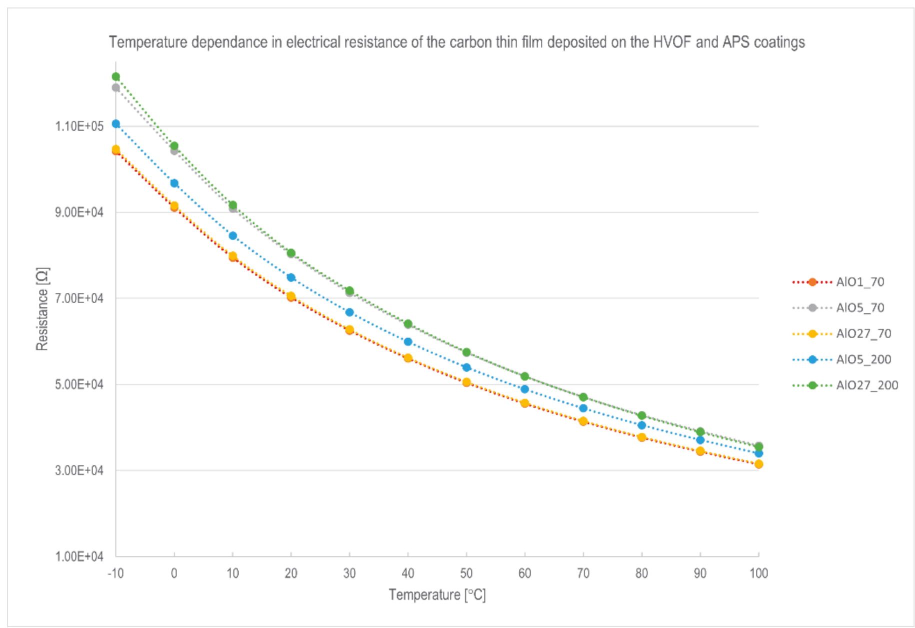


**Figure 73.** Temperature sensitivity of resistance in piezoresistive hard carbon thin films deposited on HVOF and APS aluminium oxide coatings.

Formula (1) was used to determine the beta value β of the NTC thermistors. It can be written in linear form to determine β as:

$$ln\,R = \frac{\beta}{T} + ln\,r_\infty\,, \tag{6}$$

where $r_\infty = R_0 e^{-\left(\frac{\beta}{T_0}\right)}$ is a constant with resistance $R_0$ determined at temperature $T_0$.

Beta values were calculated with the linear regression model fit shown in Figure 74. The linear fit had a good correlation with the measured data with all the samples. This can be seen from the $R^2$ coefficient of determination values of between 0.9993 and 0.9994 for the measured samples.

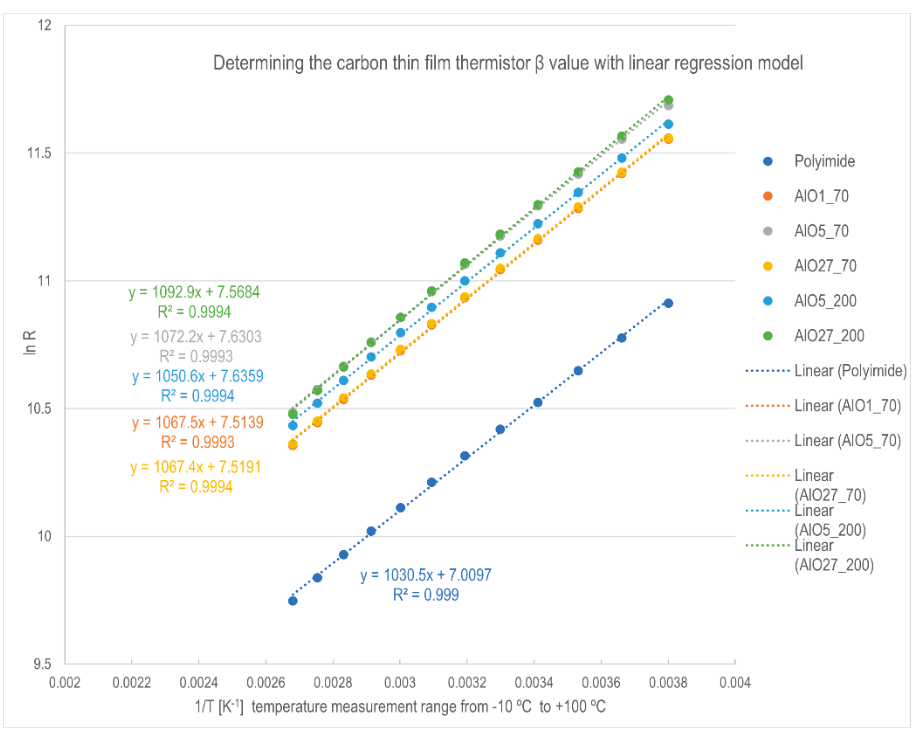


**Figure 74.** Determination of thermistor β value of piezoresistive hard carbon thin films on HVOF and APS coatings with a linear regression fit model.

The beta values β calculated from the samples are listed in Table 8. Roughness had less influence on the beta value than on the resistance level of the samples because beta value is related to the intrinsic semiconductive structure of hard carbon film which is not influenced by the dielectric layer. The variation in the beta value of the carbon thin film was 1.4 %, whereas in electrical resistance $R_0$ it was 6.7 % with for films deposited on the thermal spray coatings. A reference beta value was also measured from a carbon thin film deposited on a polyimide substrate. The electrical resistance $R_0$ measured at 20 °C of $3.72\text{x}10^4$ Ω was smaller, due to lower surface roughness of the polyimide substrate than with the thermal spray coatings. Unexpectedly, the beta value of 1031 was smaller on the polyimide substrate, indicating that the carbon thin film possessed a higher temperature sensitivity on thermal spray coatings.

**Table 8.** Beta values of carbon thin film measured on HVOF and APS thermal spray coatings.

| Substrate | Insulating layer | β value | $R_0$ (Ω) at 293 K |
|---|---|---|---|
| S235JR | AlO1_70 | 1068 | $7.02x10^4$ |
| S235JR | AlO5_70 | 1072 | $8.03x10^4$ |
| S235JR | AlO27_70 | 1067 | $7.06x10^4$ |
| S235JR | AlO5_200 | 1051 | $7.48x10^4$ |
| S235JR | AlO27_200 | 1093 | $8.06x10^4$ |
| | | | |
| Average | | 1070 | $7.53Ex10^4$ |
| Stdev | | 15 | $5.04x10^3$ |

Reference sample measured on polyimide

| Substrate | | β value | $R_0$ (Ω) at 293 K |
|---|---|---|---|
| PI | - | 1031 | $3.72x10^4$ |

### 7.5.2 Strain sensitivity and gauge factor of piezoresistive carbon thin film deposited on thermally sprayed HVOF and APS coatings

The piezoresistive carbon thin film deposited on the HVOF and thermal spray APS coatings on the S235JR cantilever beam substrates was used for the bend test measurements to determine the gauge factor of the samples. The parameters and dimensions of the cantilever beam are listed in Table 9.

**Table 9.** Parameters of S235JR cantilever beam used in gauge factor calculation.

| Cantilever beam substrate of S235JR steel | | |
|---|---|---|
| Elastic modulus | 210 | Gpa |
| Bending length, L | 120 | mm |
| Beam width, w | 20 | mm |
| Thickness of the beam, d | 2 | mm |
| Thickness of the insulating layer | 70-200 | µm |
| Other parameters | | |
| Deflection $\omega_c$ | 1 | mm |

The measurement of strain was performed by applying a bending force P to induce deflection $\omega c$ of 1 mm in the cantilever at bending distance L, on point C, shown in Figure 25. The resistance of the hard carbon film was measured as a 30-second average at two positions, the deflected position of 1 mm, and the initial position without deflection. Figure 75 shows the resistance measurement in the bend test with a 750 nm hard carbon thin film deposited on an HVOF AlO1_70 aluminium oxide layer. The change in resistance $\Delta R = R - R_0$ was determined as the difference from the integrated averages of the measured resistance of these two 30-second periods with and without deflection. The measurement was repeated 10 times in cycles of 100 seconds; the average values of $\Delta R/R_0$ are recorded in Table 10. Both the change in ambient temperature and bending deformation caused some temperature drift in the resistance level during measurements, which can be seen in the graph in Figure 75.

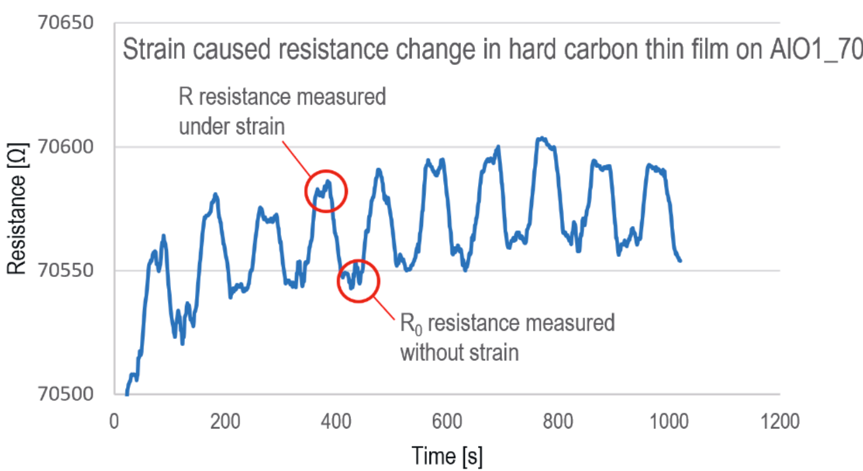


**Figure 75.** Resistance change of 750 nm hard carbon film deposited on AlO1_70 sample in strain measurement with cyclic 1 mm deflection of S235JR cantilever beam.

The gauge factor of the hard carbon thin films on thermal spray samples was calculated from formula (4) as $GF = (\Delta R / R_0)/\varepsilon$, where strain ε was calculated at point L/2 of the cantilever beam using the parameters in Tables 9 and 10.

**Table 10.** Calculated gauge factor of 750 nm hard carbon thin film on thermal spray coatings measured at 1 mm cyclic deflection of S235JR cantilever beam.

| Insulating layer | AlO1_70 | AlO5_70 | AlO27_70 | AlO5_200 | AlO27_200 |
|---|---|---|---|---|---|
| Bending force [N] | 3.7 | 3.5 | 4.0 | 3.3 | 3.6 |
| Deflection [mm] | 1 | 1 | 1 | 1 | 1 |
| Strain ε at L/2 | $8.48 \times 10^{-5}$ | $8.03 \times 10^{-5}$ | $9.17 \times 10^{-5}$ | $8.36 \times 10^{-5}$ | $9.26 \times 10^{-5}$ |
| ΔR/R | $4.59 \times 10^{-4}$ | $4.75 \times 10^{-4}$ | $4.94 \times 10^{-4}$ | $5.45 \times 10^{-4}$ | $5.46 \times 10^{-4}$ |
| | | | | | |
| Gauge factor GF | 5.41 | 5.92 | 5.38 | 6.52 | 5.90 |
| Average GF | 5.83 | | | | |
| Stdev of GF | 0.46 | | | | |

Reference strain gauge LY21-3/120 specified GF 1.97 ± 1% by the manufacturer HBM

| Substrate | Insulating layer | GF measured |
|---|---|---|
| S235JR | Polyimide | 2.04 |

The gauge factor of the samples had a relatively large variation in the calculated values of 8 %. Samples with the thicker 200 μm APS coatings possessed a slightly higher value in the gauge factor. The average gauge factor value of AlO5_200 was over the standard deviation of all the samples. The accuracy in the determination of the gauge factor was influenced by the bending of the cantilever beams caused by deposition of the thermal spray layers. This can be seen in the variation of the bending forces between the samples in Table 10. As a reference, a commercial metal foil strain gauge LY21-3/120 on polyimide was measured glued onto a S235JR cantilever beam in the L/2 position and measured in the bend test with 1 mm deflection. The GF value of 2.04 shown in Table 10 had a deviation of 3.6 % from the manufacturer's specified average value of 1.97 ± 1% measured in the bend test.

### 7.5.3 Mechanical fatigue resistance of thermal spray $Al_2O_3$ measured with hard carbon thin film on a S235JR steel cantilever beam

The fatigue resistance of the thermal spray coatings was measured with the 200 μm APS $Al_2O_3$ coating in a bend test. The sample was chosen due to the high gauge factor measured on the AlO5_200 layer and thickness of the layer which was assumed to influence the perception of potential fatigue fracture. The test was accomplished during a period of 24 working days as an average of 280 bend cycles per day at a total cycle count of 6730 and operating time of 187 hours.

The measurement of mechanical fatigue was performed as cyclic bending of the cantilever beam by force P applied at end point C of the cantilever beam to achieve a constant deflection of 3 mm, as shown in Figure 25. Before the cyclic bending, a constant preload $P_0$ of 12.5 N was applied to compensate for the distortion of the cantilever beam caused by the residual stress in the 200 μm AlO5_200 layer to reach the zero-point calibration of the deflection. Additional cyclic bending force $P_c$ of 13.6 N was applied to reach a deflection $\omega_c$ of 3 mm from the zero point. The maximum force P applied was 26.1 N (12.5 N + 13.6 N), which was calculated to be in the limit of elastic section modulus $Z = M/\sigma_y$ for the cantilever beam at anchor point (x=0), where moment was M=PL. The yield strength $\sigma_y$ was 235 MPa for S235JR steel, and elastic section modulus $Z = 1/6wd^2$ was calculated from the

cantilever beam dimensions. The calculated maximum strain ε caused by force 26.1 N was 0.067 % at point L/2 for the carbon thin film and AlO5_200 layer.

The gauge factor was calculated with the formula (4 ) as $GF = (\Delta R / R_0)/\varepsilon$ where strain was determined from formula (3) at point L/2 with the cyclic bending force $P_c = P - P_0$ needed for the 3 mm deflection and from the related resistance change $\Delta R/R_0$, where $\Delta R = R - R_0$, and R was measured when force P was applied and accordingly $R_0$ when force $P_0$ was applied. Figure 76 shows the gauge factor with the measured bending force $P_c$ needed for the 3 mm deflection. The dots in the figure represent the daily average values. The average gauge factor during the measurement of fatigue resistance was 5.6 with a standard deviation of ±0.12.

The sample was studied after the test by visual inspection, as shown in Figure 77, and by imaging the hard carbon layer and the Ti6Al4V contact pad interface of the sample with Leica DM 2500M metallurgical microscope, shown in Figure 78. No defects caused by fatigue were found in the sample. The mechanical fatigue resistance measurement did not indicate a drift in the gauge factor but a reduction in cyclic bending force $P_c$ was noticed at the beginning of the measurement. The decrease in the bending force was from a level of 13.7 N to an average level of 11.5 N. After the test, the cantilever beam was studied, as shown in Figure 79. Further inspection of the cantilever beam indicated that bending was caused by plastic deformation at the anchor point (x=0) of the cantilever beam.

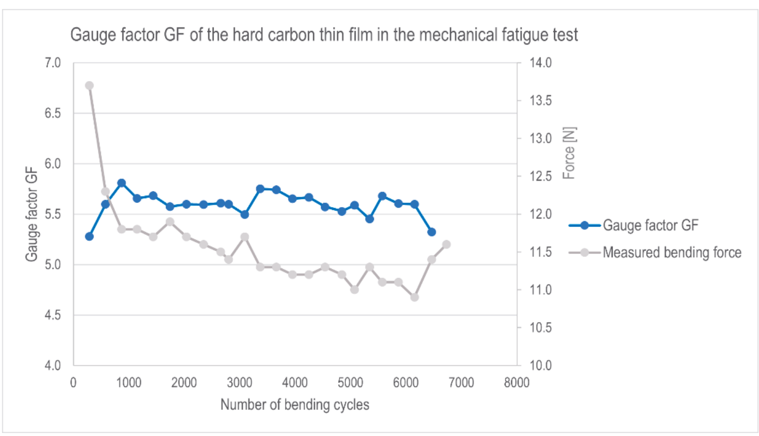


**Figure 76.** Gauge factor of hard carbon film on 200 µm APS $Al_2O_3$ layer and bending force of 3 mm deflection in mechanical fatigue resistance measurement.

**Figure 77.** APS $Al_2O_3$ sample after measurement of mechanical fatigue resistance on the S235JR cantilever beam.

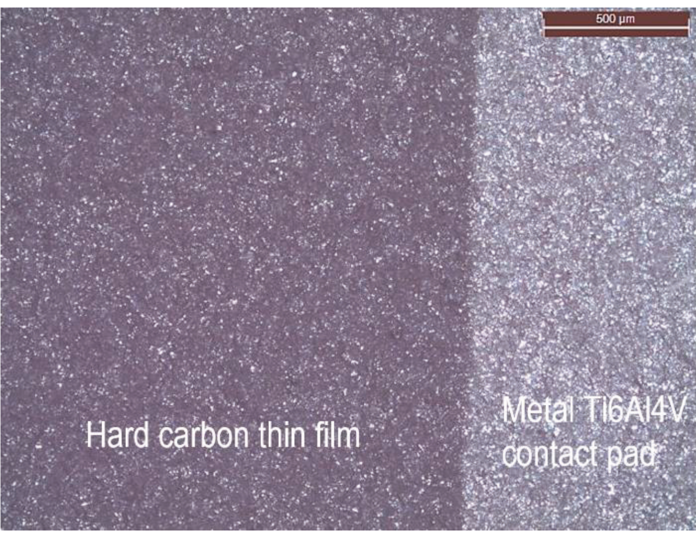


**Figure 78.** Optical image of contact interface between hard carbon layer and Ti6Al4V contact pad after fatigue resistance measurement.

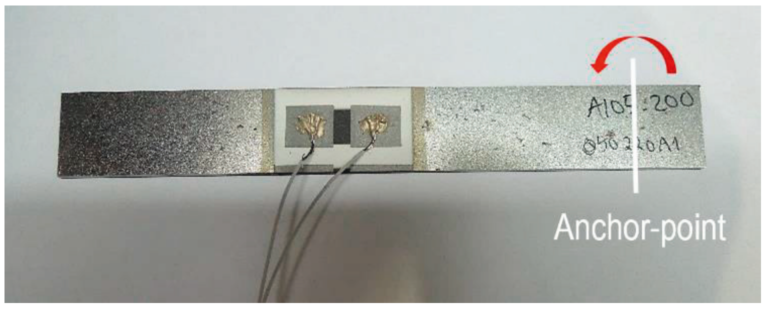


**Figure 79.** Deflection of cantilever beam at the anchor point (x=0) caused by plastic deformation.

A further study was performed to understand the reason for the decrease in the cyclic bending force in the fatigue resistance measurement. Therefore, the force-deflection curve of the S235JR cantilever beam was measured with a new sample, AlO1_40, as shown in Figure 80. A comparison of the measured force with the elastic model indicates that plastic deformation in the cantilever beam occurs already earlier between 20 N and 25 N, which is less than the calculated 26.1 N limit using the elastic section model.

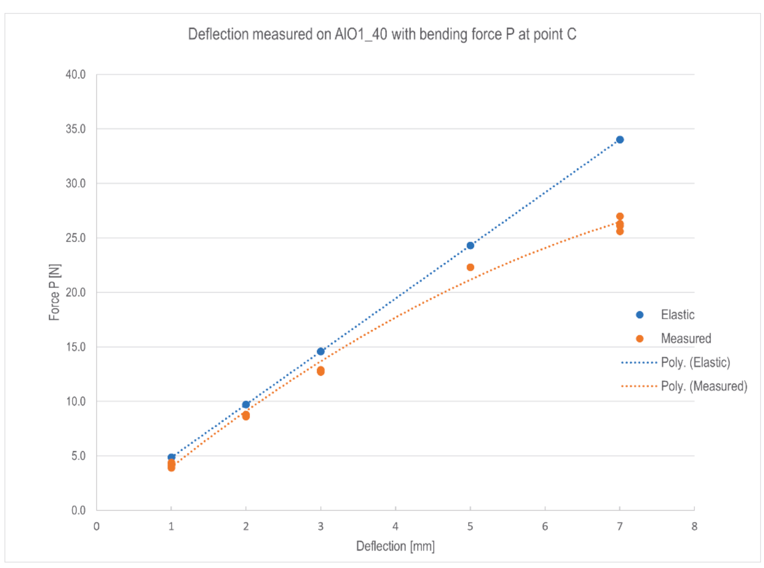


**Figure 80.** Force-deflection relation measured at end point C of S235JR cantilever beam.

A shift in the electrical resistance $R_0$ ensuing from potential defects of the hard carbon film was also studied. Drift in the electrical resistance during the 24 days of the fatigue resistance measurement was related to the changes in the ambient temperature conditions in summer. Figure 81 shows the strong correlation between $R_0$ and temperature change; however, this source of error is very small, 0.003%, when calculated from the daily min-max values $\Delta R/R_0$ of the cyclic fatigue resistance measurement. The result indicates that there is a requirement for temperature compensation if measuring a static or slowly changing strain.

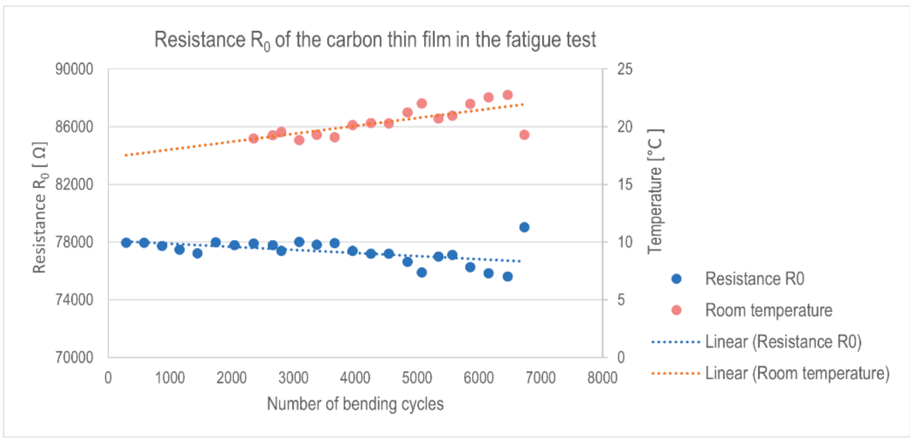


**Figure 81.** Correlation of resistance $R_0$ with ambient temperature conditions during fatigue resistance measurement.

## 7.6 RF-sputter deposited PVD $Al_2O_3$ coatings on 90MnCrV8 tool steel samples

The properties of PVD $Al_2O_3$ coatings were studied by reactive RF sputtering of thin films on 90MnCrV8 tool steel substrate discs (Ø22x5.6 mm) at deposition temperatures from room temperature to heated substrate temperatures of 125 °C, 200 °C and 250 °C. Deposition was started with a 50 nm thick aluminium interlayer in metallic mode prior to the reactive deposition of an $Al_2O_3$ layer to improve adhesion. In the reactive mode sputtering, the $O_2$/Ar flow ratio was varied from 5% to 20% and deposition pressure from 3 to 12 µbar for the samples studied.

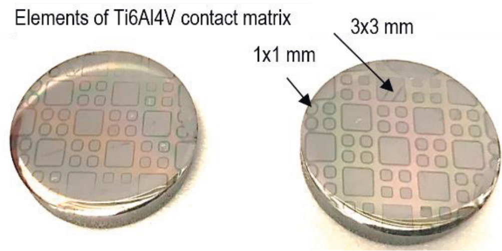


**Figure 82.** Samples of RF-sputtered $Al_2O_3$ coatings deposited at room temperature with Ti6Al4V metallic contact matrix of 3x3mm$^2$ and 1x1mm$^2$ elements as a top layer.

A conductive top layer of Ti6Al4V was deposited on the PVD aluminium oxide coatings by cathodic vacuum arc-discharge and patterned with a steel shim to form a matrix of 3x3 mm$^2$ and 1x1 mm$^2$ electrode elements for the resistivity and leakage current measurements. The purpose of the patterning was to study the areal short circuit density of the samples. Samples of aluminium oxide coatings with the patterned Ti6Al4V layer on 90MnCrV8 discs are shown in Figure 82.

### 7.6.1 Structure of PVD $Al_2O_3$ coatings deposited by RF sputtering.

Roughness parameters were studied first with the samples deposited at 12 µbar pressure and with an $O_2$/Ar flow ratio of 8–9 % at four different temperatures 20 °C (RT), 125 °C, 200 °C and 250 °C. The elevation of the substrate temperature in

the deposition increased the coating average roughness $R_a$ slightly, as seen in Figure 83. Sample 120721A1 deposited at 250 °C had the lowest $R_z$ mean roughness depth, but it had also the lowest thickness 0.58 μm measured with a Dektak XT profilometer. The high peak roughness $R_p$ values of the coatings indicated that the coatings suffered from surface anomalies caused by particles of dust and droplets of the target material collecting on the surfaces, which can be seen in the optical images of the samples in Figures 84–86. SEM surface analysis of the sample 120721A1 confirmed that the reason for the $R_p$ roughness shown in Figure 87, was the melted droplets as anomalies on the surface.

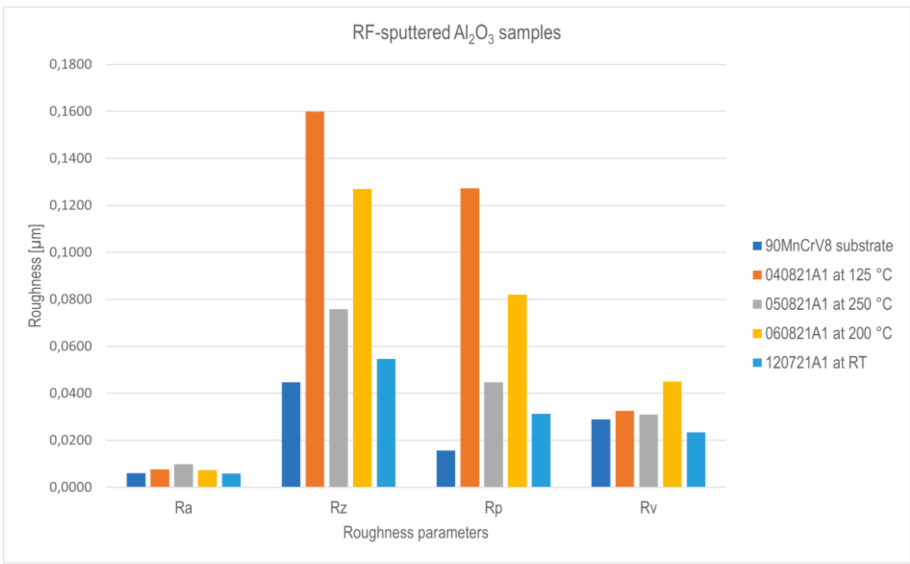


**Figure 83.** Average roughness ($R_a$), mean roughness depth ($R_z$), maximum peak ($R_p$) and maximum valley roughness ($R_v$) of RF-sputtered $Al_2O_3$ coatings measured with a Dektak XT profilometer.

**Figure 84.** Optical image of RF-sputtered $Al_2O_3$ sample 120721A1 of 0.58 µm deposited at 20 °C (RT).

**Figure 85.** Optical image of RF-sputtered $Al_2O_3$ sample 040821A1 of 0.85 µm deposited at 125 °C.

**Figure 86.** Optical image of RF-sputtered $Al_2O_3$ sample 050821A1 of 1.3 µm deposited at 250 °C.

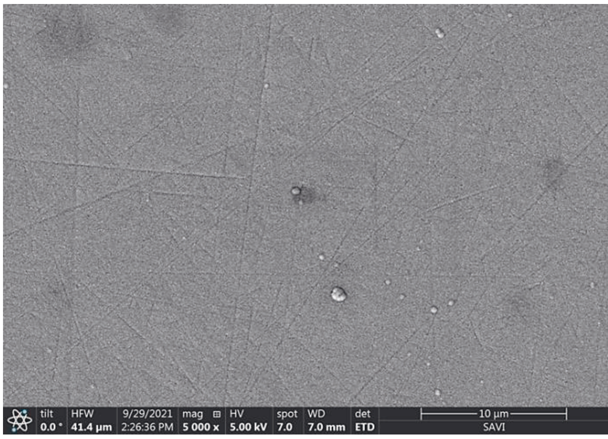


**Figure 87.** SEM surface image of RF-sputtered $Al_2O_3$ sample 120721A1 deposited at 20 °C.

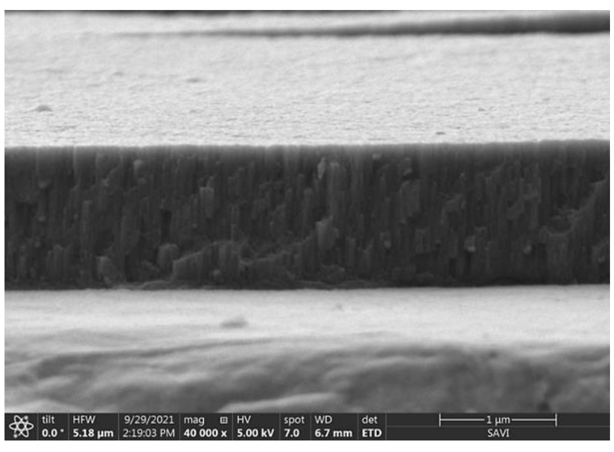


**Figure 88.** SEM cross-section image of RF-sputtered aluminium oxide sample 120721A1.

The SEM cross-section image of sample 120721A1 in Figure 88 depicts a relatively dense zone 1 type columnar structure [70] in the coating. The columnar structure was common to all samples regardless of the deposition temperature.

The mechanical properties hardness (HIT) and elastic modulus (EIT) were measured with nanoindentation. The chemical composition in the samples was measured with energy dispersive spectroscopy (EDS), shown in Table 11. The thickness of the coatings in Table 11 was determined from the SEM cross-section images.

**Table 11.** Mechanical properties and chemical composition of RF-sputtered $Al_2O_3$ coatings.

| Sample | Thickness SEM [μm] | Mechanical properties | | EDS chemical composition | | |
|---|---|---|---|---|---|---|
| | | HIT [GPa] | EIT [GPa] | Al [at%] | O [at%] | Fe [at%] |
| 120721A1 | 1.0 | 10.9 | 174.8 | 21.8 | 77.3 | 0.9 |
| 251121A1 | 1.4 | 7.3 ± 0.87 | 146.0 ± 4.0 | 34.8 | 64.3 | 0.9 |
| 261121A1 | 1.6 | 8.7 ± 0.27 | 162.9 ± 3.4 | 37.3 | 61.1 | 0.6 |
| 221221A1 | 1.6 | 6.6 ± 0.25 | 129.7 ± 2.7 | 33.7 | 65.3 | 1.0 |
| 231221A1 | 1.7 | 4.8 ± 2.2 | 115.6 ± 3.4 | 31.3 | 65.4 | 3.3 |
| 301221A1 | 10.0 | 8.6 ± 0.31 | 144.4 ± 2.7 | 36.7 | 63.3 | 0.0 |

The chemical composition of samples 261121A1 and 301221A1 was the closest to the stoichiometry of $Al_2O_3$. Sample 261121A1 was deposited at room temperature at a deposition rate of 0.25 μm/h at 6 μbar total pressure with a DC probe voltage average of 660 V and $O_2$/Ar flow ratio of 14.3%. Sample 301222A1 was deposited at room temperature at a deposition rate of 0.82 μm/h at a 12 μbar total pressure with a DC probe average voltage average of 370 V and an $O_2$/Ar flow ratio of 7.8%. The iron concentration as an impurity in the chemical composition of EDS analysis originated from the 90MnCrV8 substrate.

The SEM surface images of sample 261121A1 showed a relatively smooth surface on the10 μm scale, as can be seen in Figure 89, but higher magnification on the 1 μm scale, shown in Figure 90, revealed macroparticle droplets of aluminium oxide on the surface. The SEM cross-section image of sample 261121A1 shown in Figure 91showed the relatively dense but columnar structure of the film. The XRD analysis shown in Figure 92 confirmed the amorphous structure of the aluminium oxide layer. The main diffraction intensities in XRD spectrum originated from the 90MnCrV8 steel substrate. There was a small intensity of crystallographic planes (1 1 1) of aluminium seen in the spectrum what was assumed to originate from the interlayer deposited prior to the reactive RF sputtering of the aluminium oxide layer in the sample, as shown in Figure 92.

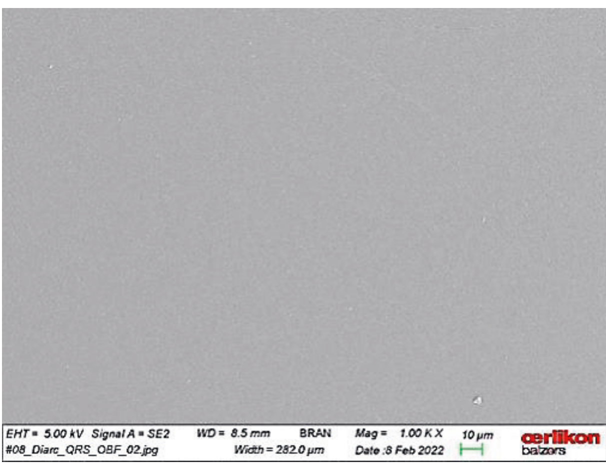


**Figure 89.** SEM surface image of sample 261121A (scale bar: 10 μm).

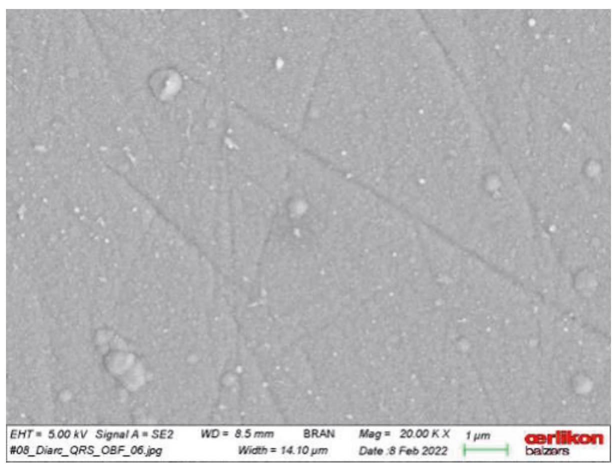


**Figure 90.** SEM surface image of sample 261121A1(scale bar: 1 µm).

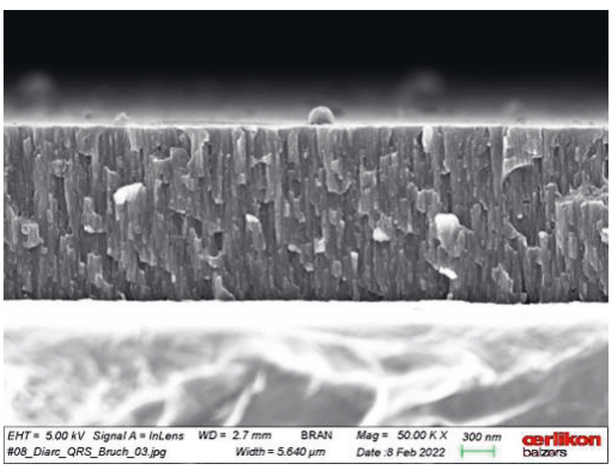


**Figure 91.** SEM cross-section image of sample 261121A1 (scale bar: 300 nm).

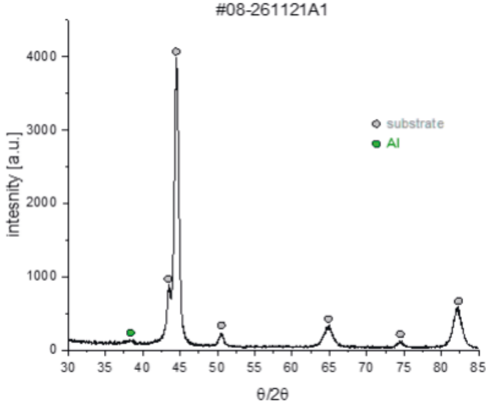


**Figure 92.** XRD pattern of sample 261121A1.

The SEM surface image of sample 301221A1 also showed some micrometre-sized nodules on the surface on the 10 µm scale, see Figure 93, and the higher magnification on the scale of 1 µm indicated the nodular surface structure of the coating, as shown in Figure 94. The SEM cross-section image on the 1 µm scale of sample 301221A1 in Figure 95 showed a columnar structure in the 10 µm thick film. The XRD analysis shown in Figure 96 also indicated the amorphous structure of the aluminium oxide layer. The main peaks in the XRD originated from the 90MnCrV8 steel substrate.

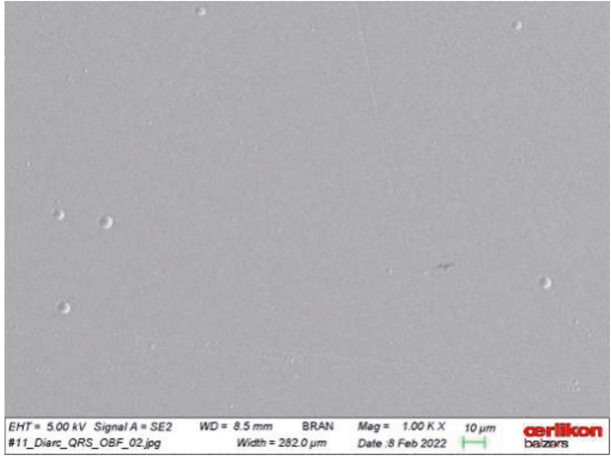


**Figure 93.** SEM surface image of sample 301221A1 (scale bar: 10 µm).

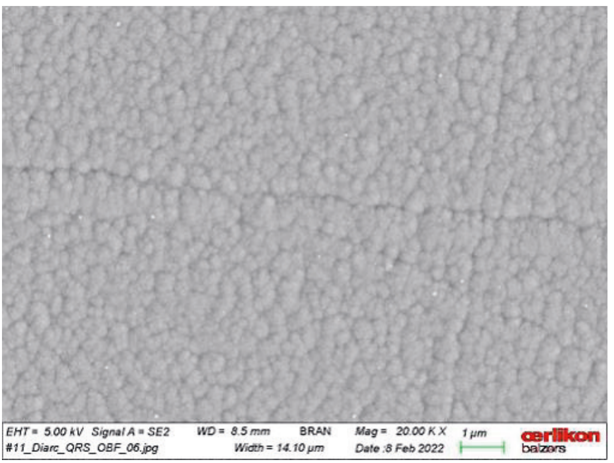


**Figure 94.** SEM surface image of sample 301221A1 (scale bar: 1 µm).

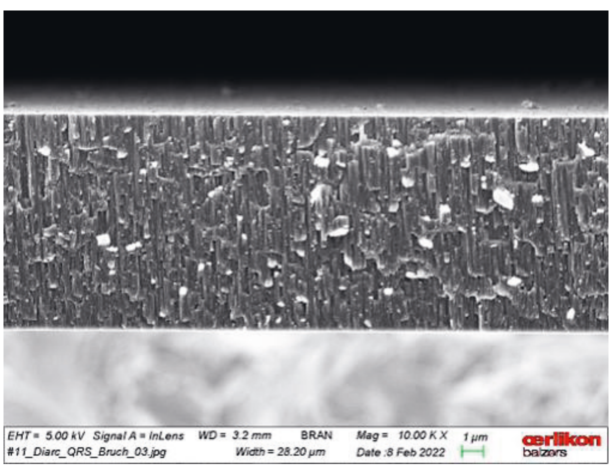


**Figure 95.** SEM cross-section image of sample 301221A1 (scale bar: 1 µm).

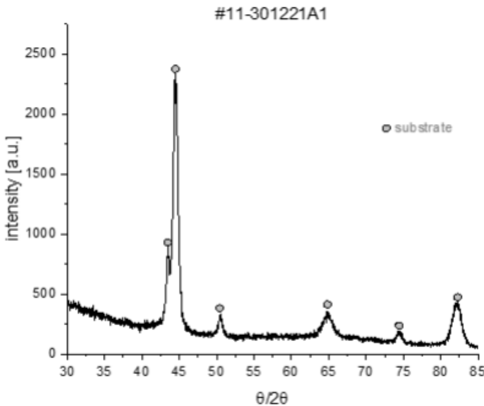


**Figure 96.** XRD pattern of sample 301221A1.

The columnar growth of the RF-sputtered aluminium oxide films was further studied with samples 160921A1 and 240921A1 deposited at 250 °C, and with added -40 V bias voltage on the substrate. Sample 160921A1 was deposited at a rate of 0.18 μm/h at 12 μbar total pressure with a DC probe voltage average of 360 V and an $O_2$/Ar flow ratio of 9%, and sample 240921A1 at a rate of 0.20 μm/h at 6 μbar total pressure with a DC probe voltage average of 400 V and an $O_2$/Ar flow ratio of 13.3%. The results were compared with sample 280921A1 deposited at 250 °C without bias and at a rate of 0.21 μm/h at 3 μbar total pressure with a DC probe voltage average of 520 V and an $O_2$/Ar flow ratio of 19.6%. The SEM surface and cross-section images of samples 160921A1 and 240921A1 are shown in Figures 97-102. The thickness of the coating was 1.4 μm in sample 160921A1 and 1.12 μm in sample 240921A1.

The main differences between the samples were the total deposition pressure and DC probe voltage level in reactive mode operation, which indicated that the sputtering took place deeper in the reactive mode at higher total pressure even when the $O_2$/Ar flow ratio was lower. When comparing the samples, the increase in columnar growth and nodular surface structure was seen more in sample 160921A1 than in sample 240921A1.

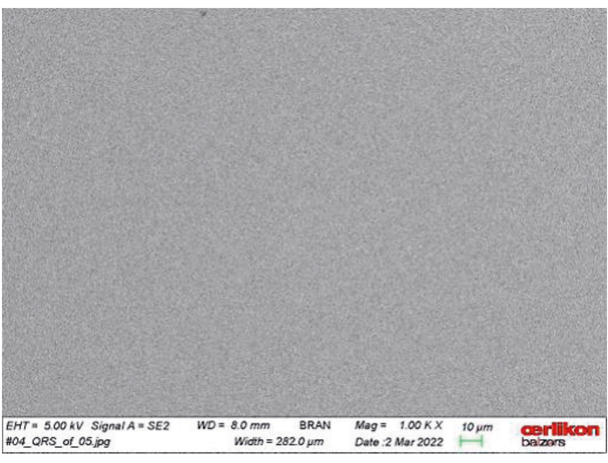


**Figure 97.** SEM surface image of sample 160921A1 (scale bar: 10 µm).

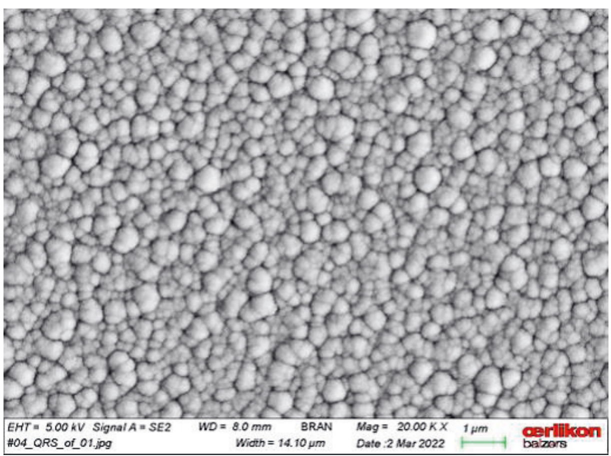


**Figure 98.** SEM surface image of sample 160921A1 (scale bar: 1 µm).

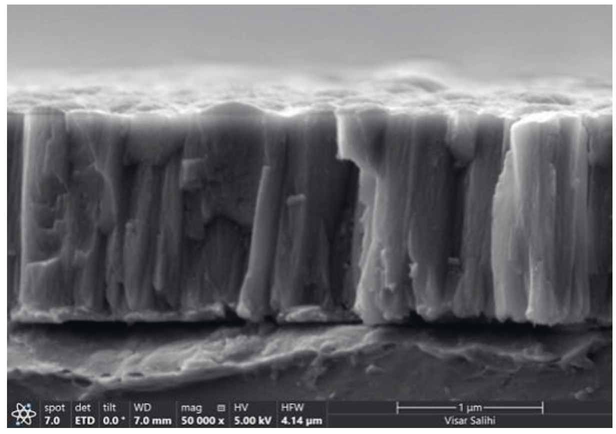


**Figure 99.** SEM cross-section image of sample 160921A1(scale bar: 1 µm).

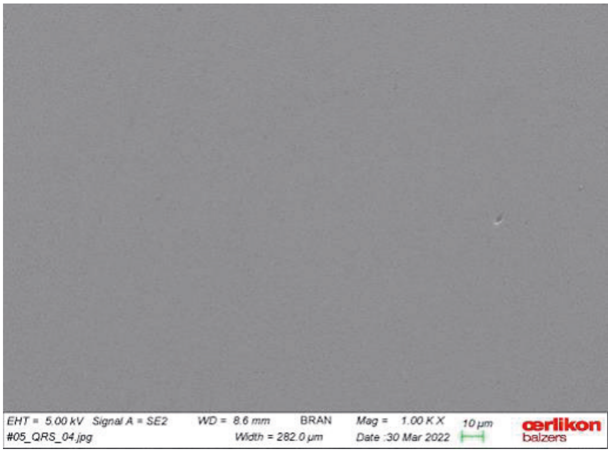


**Figure 100.** SEM surface image of sample 240921A1 (scale bar: 10 µm).

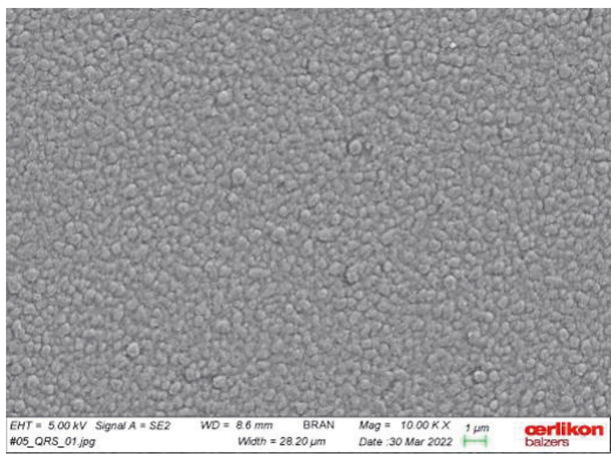


**Figure 101.** SEM surface image of sample 240921A1 (scale bar: 1 µm).

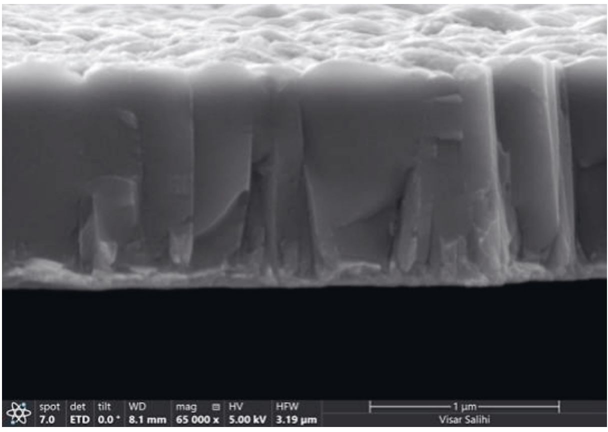


**Figure 102.** SEM cross-section image of sample 240921A1(scale bar: 1 µm).

The use of the substrate bias voltage was not seen as critical, when the result was compared to sample 280921A which was grown at 250 °C at a lower total pressure of 3 µbar with an average DC probe voltage of 520 V, i.e. not as deep in the reactive mode. The structure of sample 280921A1 shown in Figures 103–105 was less columnar, when compared to the samples deposited at higher pressure levels of 6 or 12 µbar.

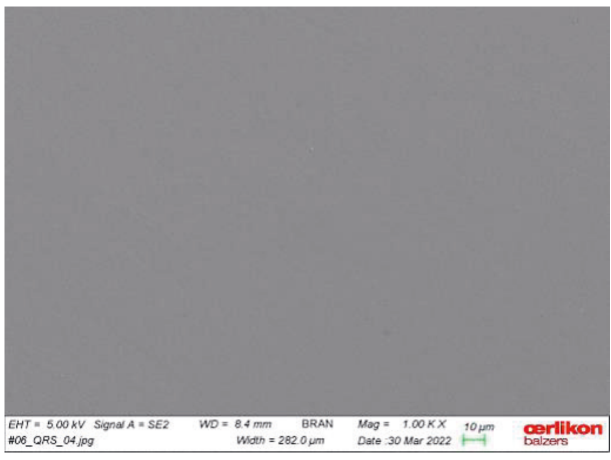


**Figure 103.** SEM surface image of sample 280921A1 (scale bar: 10 µm).

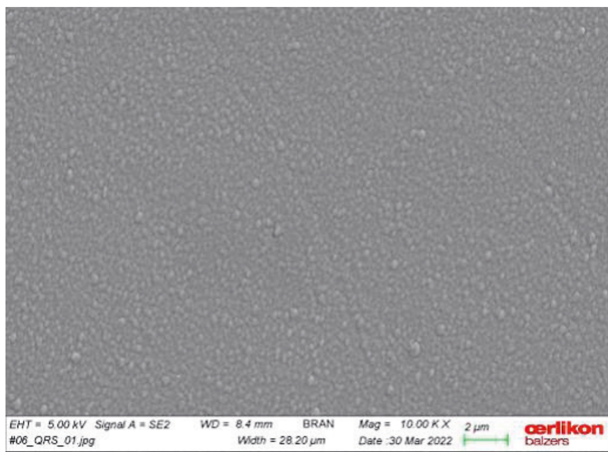


**Figure 104.** SEM surface image of sample 280921A1 (scale bar: 2 µm).

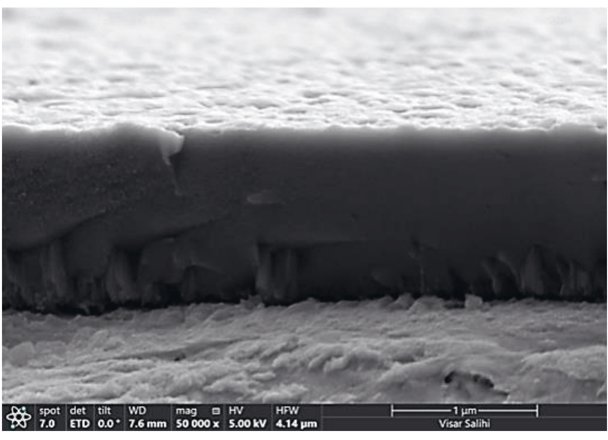


**Figure 105.** SEM cross-section image of sample 280921A1 (scale bar: 1 µm).

The XRD analysis of samples 160921A1, 240921A1 and 280921A1 in Figure 106 indicated the amorphous structure in all the coatings. A small quantity of metallic aluminium seen in the XRD spectra of the samples was assumed to originate from the aluminium interlayer deposited on the substrate prior to the reactive sputtering of the aluminium oxide layer.

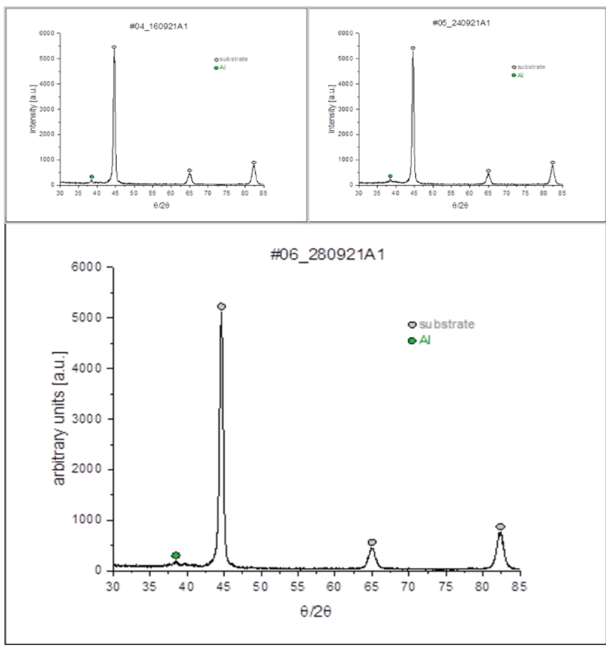


**Figure 106.** XRD patterns of samples 160921A1, 240921A1 and 280921A1.

### 7.6.2 Resistivity of RF-sputtered PVD $Al_2O_3$ coatings

The resistance of the PVD aluminium oxide samples was screened before leakage current measurements were performed with the samples. Due to the high defect density found in the aluminium oxide films the criterion for the electrode pad resistance was set as $R_{pad} > 2$ MΩ, which the RF-sputtered aluminium oxide films should fulfil when measured between the substrate and the 3x3 $mm^2$ or 1x1 $mm^2$ contact pads. The criterion of the resistance level would mean a 5% tolerance in deviation when functioning as a shunt element with a typical hard carbon sensor with 100 kΩ resistance.

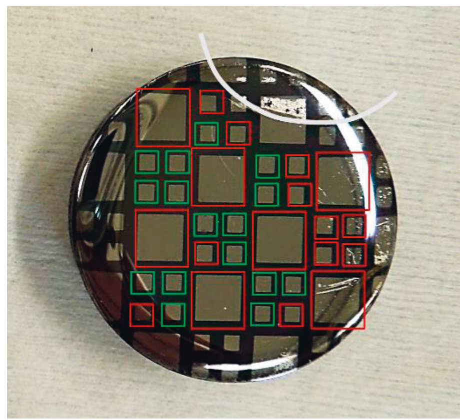

**Figure 107.** Resistance screening of RF-sputtered Al203 sample 050821A1. Contact pads marked in green possessed a resistance of over 2 MΩ.

Resistance screening performed with sample 050821A1 is shown in Figure 107. The sample had 16 pads out of a total count of 27 with a resistance value over the criterion with the 1x1 $mm^2$ pads (marked in green) and a zero count of 3x3 $mm^2$ pads which did not pass it. The 1x1 $mm^2$ pads that fulfilled the criteria possessed an electrical resistance of 850 ± 350 MΩ. The high deviation found in the pads was assumed to be due to the high defect density caused by dust particles found in the

aluminium oxide coatings. All the resistance screening results for the samples are summarized in Table 12.

**Table 12.** RF-sputtered AlO3 samples screened with criterion of $R_{pad}$ resistance > 2 MΩ.

| Sample code | Ti6Al4V electrodes of 1x1 mm with R > 2 MΩ / total quantity | Ti6Al4V electrodes of 3x3 mm with R > 2 MΩ per total quantity |
|---|---|---|
| 120721A1 | 0/20 | 0/6 |
| 040821A1 | 0/20 | 0/6 |
| 050821A1 | 16/27 | 0/7 |
| 060821A1 | 0/20 | 0/6 |
| 140921A1 | 0/20 | 0/6 |
| 160921A1 | 0/20 | 0/6 |
| 240921A1 | 1/31 | 0/6 |
| 280921A1 | 6/37 | 0/6 |
| 261121A1 | 10/24 | 0/6 |
| 221221A1 | 0/24 | 0/6 |
| 231221A1 | 8/24 | 1/6 |
| 301221A1 | 34/40 | 5/10 |

### 7.6.3 Leakage current in RF-sputtered PVD $Al_2O_3$ coatings

Direct current measurements were performed with samples 050821A1, 261121A1 and 301221A1 which gave a positive result in electrical resistance screening measured from several electrode pads of 1x1mm$^2$. The measurements were each performed on a separate electrode pad. Sample 050821A1, with layer thickness of only 1.3 μm was chosen for the study of the dielectric breakdown strength of RF-sputtered PVD aluminium oxide coatings. Measurements were performed at four different voltage levels: 20, 50, 100 and 200 VDC, as shown in Figures 108–110.

The leakage current in sample 050821A1 was very similar in measurements performed at both 20 and 50 voltage levels. A relatively fast decrease in leakage current was observed in the three consecutive measurement runs performed at 18 °C and 49.7% RH, shown in Figure 108. The resistivity of the aluminium oxide coating in sample 050821A1 was calculated from the third measurement run when

the effect of humidity on the leakage current was already low. The resistivities of the samples determined from the measurements are collected in Table 13.

**Table 13.** Resistivity of RF-sputtered $Al_2O_3$ coatings calculated from leakage current measurements.

| Sample ID | Resistivity [Ωm] | Temperature [°C] | Relative humidity [%] |
|---|---|---|---|
| 050821A1 | $4.12 \times 10^{9}$ | 18.0 | 49.7 |
| 261121A1 | $1.18 \times 10^{12}$ | 20.9 | 8.7 |
| 301221A1 | $3.77 \times 10^{10}$ | 21.3 | 13.2 |

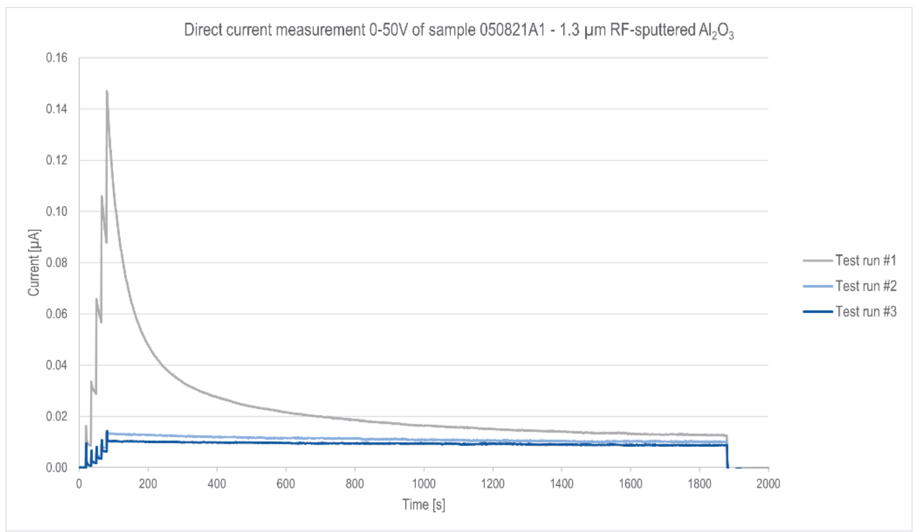


**Figure 108.** Leakage current measurement of 1.3 µm thick RF-sputtered sample 050821A1at 50 V and at 18 °C and 49.7% RH.

Testing of DBS was continued by increasing the voltage level in the direct current measurement up to 100 V, shown in Figure 109. The decrease in the leakage current was similar to the measurements performed at lower voltage levels, but the leakage current was dominated by discharge peaks of dielectric breakdown seen in the sample. This was assumed to be affected by the inhomogeneity in the film caused by conductive dust particles or voids in the deposited aluminium oxide layer. It was concluded, that for the 1.3 µm PVD aluminium oxide coating, the 50 volt level was

close to maximum, resulting in an estimate of 38 MV/m for the dielectric breakdown strength in the aluminium oxide film of the sample.

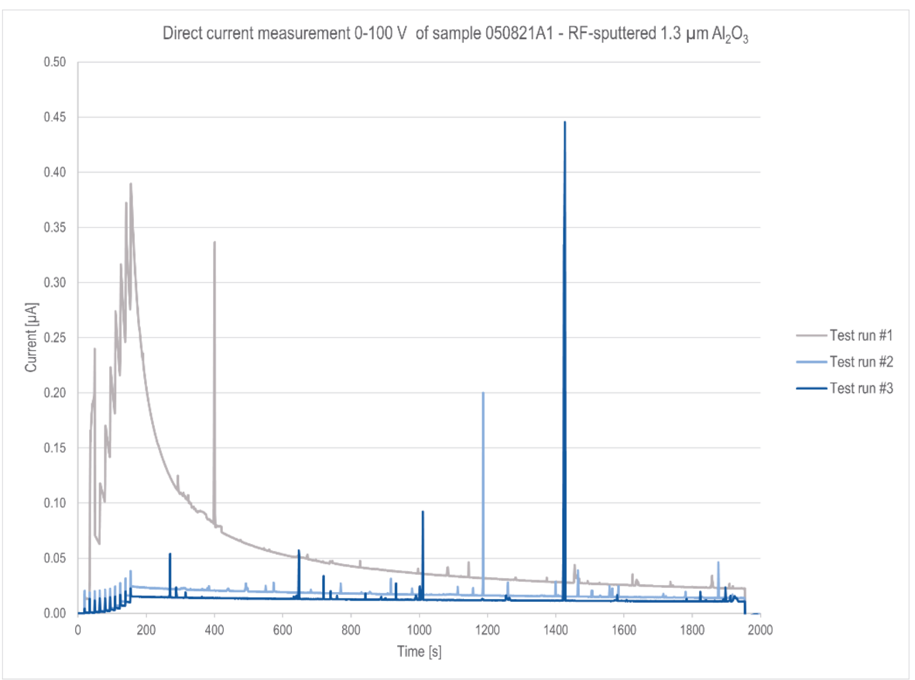


**Figure 109.** Leakage current measurement of 1.3 µm RF-sputtered sample 050821A1 at 100 V and at 19 °C and 47.2% RH.

Testing of DBS was continued at the level of 200 V with a new pad, as shown in Figure 110. The current discharge did not occur during the voltage ramp-up phase to 200 V but soon after, at 400 seconds, a current discharge peak was detected, followed by an increase in the level of the leakage current which grew to a continuous arc in 1400 seconds. The optical image of the electrode pad, shown in Figure 111, revealed the defective points in the Ti6Al4V layer where the electrical discharge had occured through the aluminium oxide layer and had caused a short circuit.

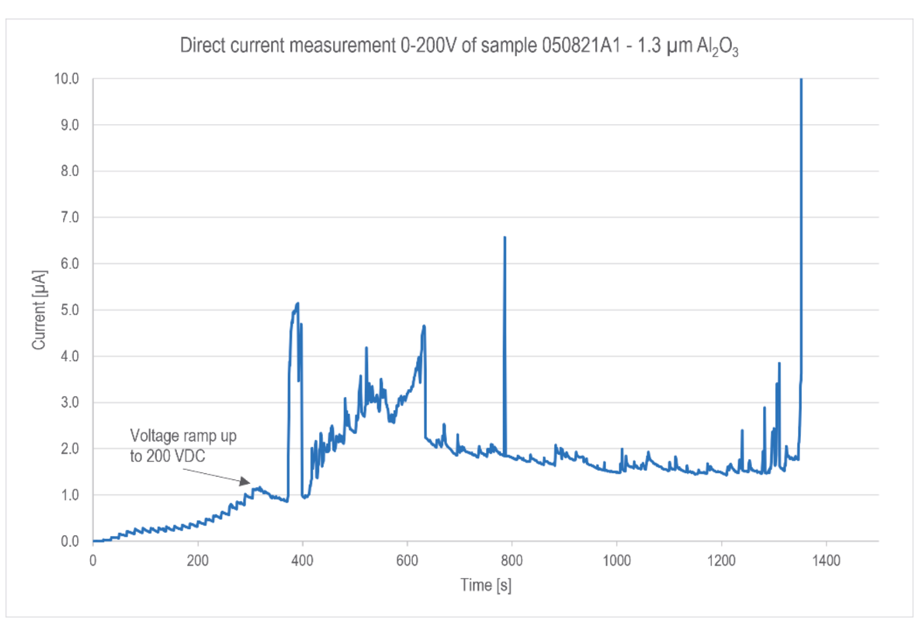


**Figure 110.** Leakage current measurement of 1.3 µm RF-sputtered sample 050821A1 at 200 V and at 21.7 °C and 69.9% RH.

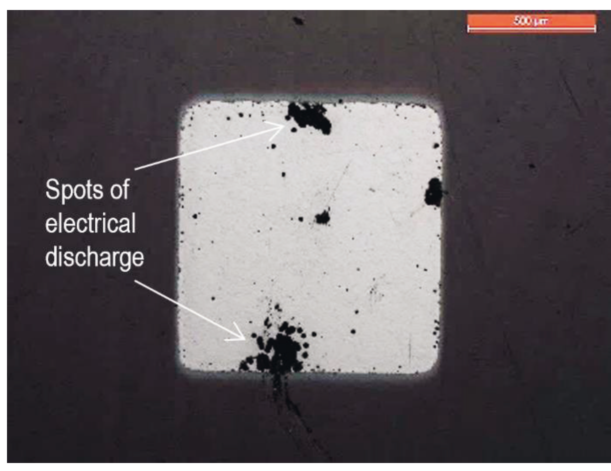


**Figure 111.** 1x1 mm[2] electrode pad of the sample 050821A1 after leakage current measurement at 200 VDC level.

The 1.7 µm thick aluminium oxide layer in sample 261121A1 was measured at dry ambient air conditions of 20.9 °C and 8.7% RH. The effect of water was present in the first measurement run. A decrease in leakage current at the 200 V level and occasional discharge peaks were detected during the first measurement run, shown

in Figure 112. The leakage current was stabilized in the second measurement run without the effect of space charge polarization or short circuit in the sample. Leakage current seen in the second and third measurement runs was on almost the same level. The only difference was detected in the charge current peaks during voltage ramp-up, indicating a difference in the polarization presumably with higher relative permittivity caused by evaporated water still in the film during the second measurement run. A resistivity of $1.18 \times 10^{12}$ Ωm was measured in the sample in the third run from the integrated average leakage current measured at 200 V, which was already close to the current detection limit of the measurement system. The DBS was not determined for sample 261121A1, due to the current discharge peaks detected during the first measurement run.

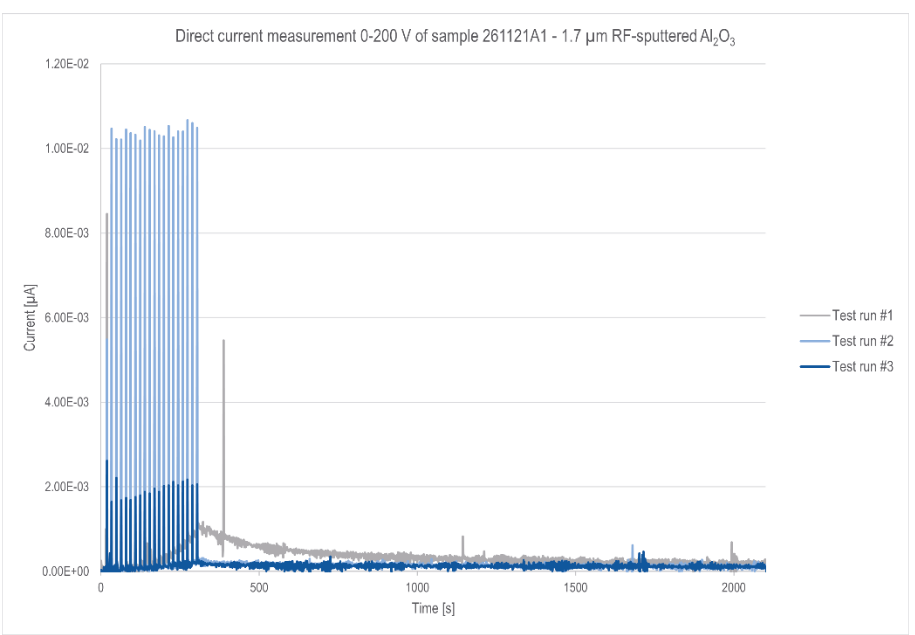


**Figure 112.** Leakage current measurement of 1.7 μm thick RF-sputtered sample 261121A1 at 200 V and at 20.9 °C and 8.7% RH.

The leakage current of the 8.8 μm thick sample, 301221A1, was measured under ambient conditions of 21.7 °C and 13.2% RH. The polarization peaks during charging in the voltage steps up to 200 V were higher in the second run than in the third run, as seen earlier with the sample 261121A1. No decrease in the leakage current was detected with any of the measurement runs for the sample. The reason

for this was assumed to be related to the low resistivity, $3.77 \times 10^{10}$ Ωm, of the aluminium oxide layer. The effect of space charge polarization in the leakage was masked by the high level of direct current through the parallel resistance of the film, as shown in Figure 113. The DBS was 22.7 MV/m calculated for the sample at 200 V. The value should be considered a low-level estimate. The limiting factor in determining the DBS was the maximum voltage level of 200 V available for the direct current measurement. The results showed that the inhomogeneity caused by dust particles and voids created a large variation in the resistivity and DBS of the films.

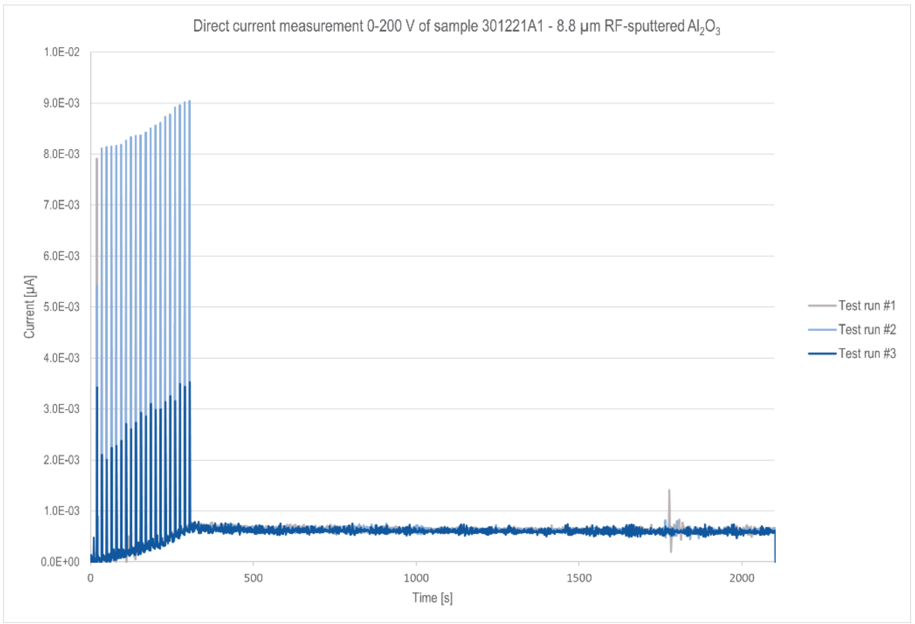


**Figure 113.** Leakage current of 8.8 µm thick RF-sputtered sample 301221A1 at 200 V and at 21.7 °C and 13.2% RH in three consecutive measurement runs.

# 8 CONCLUSIONS

The literature review in the study indicated the favourable and promising technical properties of aluminium oxide coatings prepared by thermal spray and PVD deposition for electrical insulation in embedded hard carbon thin film sensors. Two basic requirements were set for the necessary electrical insulation. The first requirement was a minimum resistivity of $10^8$ Ωm over a temperature range of between -10 °C and +100 °C under ambient air conditions of 20% RH; the second was a breakdown voltage of the insulating layer of up to 200 VDC. However, there were several open questions to tackle related to the stability of the dielectric aluminium oxide layers when applied to changing ambient conditions in direct current measurements at the operation voltage levels studied. Much of the work in this study consisted of leakage current measurements performed as step response type measurements of 30 min transient periods in consecutive measurement runs in changing ambient air conditions.

APS, HVOF and PVD aluminium oxide coatings were studied as-deposited without additional post-treatment before measurement was carried out. Leakage current measurements were performed to determine the resistivity of aluminium oxide coatings with PVD deposited Ti6Al4V contact electrodes deposited on the aluminium oxide layers. The piezoresistive properties were studied of the PVD hard carbon thin films on thermally sprayed aluminium oxide coatings. The thin Ti6Al4V PVD films highlighted the influence of surface roughness and porosity in the leakage current measurements, especially with thermal spray insulating layers. The PVD electrode layers were conformal and conductive enough for the measurements but not pinhole-free, which allowed the permeation of water. The advantage of this was the possibility to study the space charge polarization of water in aluminium oxide layers with leakage current measurements under different temperature and humidity conditions. The polarization phenomena of aluminium oxide layers were complex, starting from adsorbed water in the chemisorbed state, changing to physiosorbed and finally to ionic movement in the electric field and anodic corrosion on the mild

steel substrates. Direct current measurement cannot distinguish between surface and bulk conductivity but the rapid changes in leakage current seen close to the dew point temperatures imply that the huge changes measured in resistivity were related more to changes in surface resistivity caused by the condensed water on the hydrophilic γ-aluminium oxide surfaces of the thermal spray coatings. The adsorbed water in the aluminium oxide coatings caused more of a long-term drift influenced by the effect of ionic movement in the space charge polarization.

The thin PVD films as counter electrodes and as a piezoresistive hard carbon layer brought the importance of surface roughness and porosity of the insulating layer more into focus, especially with thermal spray coatings. The conformity of the cathodic arc deposited Ti6Al4V contact electrode and hard carbon layers was excellent over the rough aluminium oxide layers. The good adhesion of the hard carbon layer on the aluminium oxide layers was also a positive result. It was observed that the roughness of the thermally sprayed aluminium oxide coatings brought additional improvement through mechanical adhesion to the PVD electrode and sensor layers. The conductivity and functionality of the electrode and sensor layers were achieved through compensation of layer thickness. Measurements of the beta value and gauge factor of the hard carbon thin film sensor elements on thermal spray coatings were new and the results were encouraging for future work with thermal spray insulating layers as-deposited without post-treatment.

## 8.1 Answer to the research questions

The answers to the research questions formulated as the aims of study give insight into a more detailed view of the performance of aluminium oxide layers for feasible electrical insulation regarding piezoresistive hard carbon sensors.

1. What thickness of APS and HVOF thermal spray or PVD aluminium oxide coating is required for effective electrical insulation on conductive steel substrates of piezoresistive hard carbon sensors?

The thickness requirement was related to the minimum resistivity requirement of $10^8$ Ωm over the temperature range from -10 °C to 100 °C at 20% RH and to the dielectric strength of 200 V over the applied dielectric layer thickness.

All the APS, HVOF and S-HVOF thermal spray aluminium oxide coatings fulfilled both requirements at coating thicknesses over 40 µm. A practical range for thermal spray coatings was between 40 and 100 µm. Thicker coatings showed a much longer drift time to decrease to a constant level in the leakage current. This was assumed to be related to the open porosity in the coatings. As a general observation, the drift in the leakage current stabilized quicker in HVOF coatings than in APS coatings with the same thickness. Thin S-HVOF coatings of 20 µm suffered from short circuits in the layer caused by open porosity and vertical cracks in the coatings. The resistivity of the thermal spray coatings was strongly related to the original ambient conditions of the coating, depending on the quantity of adsorbed water. However, the resistivity values measured at 20 ºC and 20% RH were between $10^{10}$ and $10^{11}$ Ωm and were very similar for both APS and HVOF aluminium oxide coatings, and slightly higher (between $5x10^{10}$ and $10^{12}$ Ωm) for the S-HVOF coatings. The measured mean roughness depth of HVOF and S-HVOF coatings possessed same average $R_z$ value of around 9 µm while the rougher APS coatings had average Rz value of 17.5 µm.

In RF-sputtered aluminium oxide coatings, the minimum thickness for the voltage duration requirement of 200V was estimated to be 2–3 µm. This was strongly dependent on the coating defects found in the structure of the RF-sputtered aluminium oxide films. The decrease in leakage current to reach the base level of the PVD coatings was much faster than with thermal spray coatings. The resistivity

measured from the PVD aluminium oxide films was $4x10^9$–$10^{12}$ Ωm. The films suffered from dust particles and voids which caused a high defect density in the films. The maximum peak depth $R_p$ was higher than the maximum valley roughness $R_v$ which indicated dust as the main constituent of the defects in the films. A relatively high DBS of 38 MV/m was estimated for 1 to 2 µm thick films and 22.8 MV/m for the 8.8 µm thick film from the leakage current measurements. The measured $R_z$ roughness of the 1 µm thick coatings varied between 0.06 µm and 0.16 µm depending on the coating thickness and the deposition parameters.

2. How the ambient conditions, temperature and humidity influence on the dielectric properties and resistivity of aluminium oxide coatings deposited by thermal spray and PVD techniques?

Changes in ambient conditions have a strong influence on thermal spray coatings. The hydrophilic γ-aluminium oxide surface and open porosity of the coatings makes them sensitive for adsorbance of water vapour into the coating. The chemi- and physisorbed water in the aluminium oxide layer causes long-term drift, seen in the measured leakage current that is affected by ionic space charge polarization. When measurements were performed close to dew point conditions with Peltier element cooling of the substrate in ambient air conditions 20 °C and 20% RH, changes of several orders in magnitude in resistivity and permittivity were observed in the thermal spray coatings. The influence of humidity can be effectively reduced with the use of sealant materials.

Drift caused by humidity was also observed with RF-sputtered PVD aluminium oxide coatings but stability in leakage current was achieved much faster than with thermal spray coatings. The PVD aluminium oxide coatings are less porous and much thinner compared to thermal spray coatings with less adsorbed water resulting in faster response in polarisation.

3. What is the thermistor beta sensitivity of piezoresistive hard carbon films on as-deposited aluminium oxide coatings?

The thermistor beta value of piezoresistive hard carbon films deposited on five different APS and HVOF aluminium oxide and APS spinel insulating coatings was measured in a Vötsch VCL 4003 climatic test cabinet at a temperature range from -10 °C to +100 °C. The average beta factor 1070±15 of the samples was successfully measured for all the thermal spray coatings. The beta values were higher than the beta value of 1030 measured on the reference hard carbon film deposited on a polyimide substrate. The result indicated a higher temperature sensitivity of the hard carbon films on thermal spray coatings than on the polyimide substrate. It was also observed that the roughness of the thermal spray coatings had less influence on the beta value than on the resistance level of the hard carbon coatings because beta value is related to the intrinsic semiconductive structure of hard carbon film which is not influenced by the aluminium oxide based dielectric layer.

4. What is the gauge factor of piezoresistive hard carbon film measured on as-deposited aluminium oxide coatings?

The strain measurements were performed with piezoresistive hard carbon thin films on HVOF and APS aluminium oxide and APS spinel coatings at the centre of a cantilever beam with a 1 mm deflection applied at the free end of the beam. The measurement was repeated 10 times in a cycle of 100 seconds and the average values of relative resistance change were recorded. The value of the gauge factor was successfully measured for all the samples. The average gauge factor of the samples was 5.83 ± 0.46, with a relatively variation of 8 % between the samples. The thicker 200 μm AlO5_200 coating possessed a higher gauge factor value over the standard deviation of all the samples. The accuracy in the determination of the gauge factor was influenced by the bending of the cantilever beams in the thermal spray deposition and by the ambient temperature drift in the resistance level caused during the measurement.

In general, the gauge factor measured for the thermal spray aluminium oxide films was three times higher in comparison to the reference metal foil strain gauge LY21-3/120.

5. What is the fatigue resistance of aluminium oxide coatings on steel substrate measured with piezoresistive hard carbon film?

The fatigue resistance of thermal spray coatings was studied with a 200 µm APS $Al_2O_3$ coating in the bend test. The sample was chosen because of the high gauge factor value measured on the AlO5_200 layer and due to the thickness of the layer, which was assumed to influence the perception of potential fatigue fracture. The test was accomplished during 24 working days as an average of 280 cycles per day with a total cycle count of 6730 and operating time of 187 hours. The strain measurements were performed with piezoresistive hard carbon thin films on APS aluminium oxide at the centre of the cantilever beam with a 3 mm deflection applied at the free end of the beam. The excess bending force at the start of the test caused plastic deformation at the anchored point of the cantilever beam, which reduced the strain, but this was considered and compensated with the real bending force measured during operation. The reduction of the bending force was from 13.7 N to an average force level of 11.5 N.

During the measurement of fatigue resistance the average gauge factor was 5.6 with a standard deviation of 0.12. No drift was observed in the gauge factor during the cyclic test. The optical imaging of the top layers did not reveal any defects caused by fatigue in the coatings, thus the visual outlook of the sample was intact.

6. How to improve the electrical insulation of thermal spray and PVD aluminium oxide coatings?

The thermal spray coatings on S235JR cantilever beams had two basic limitations. The first was the high sensitivity to humidity, which caused long-term drift in resistivity at variable temperature, and huge changes in resistivity close to dew point conditions. The second limitation was that anodic corrosion of the mild steel started during the direct current measurements with the porous coatings at long humidity exposure times. We were able to reduce both limitations significantly with the use of the novel S106-049 solvent-free two-component resin solution sealant on the APS-deposited aluminium oxide layers.

With PVD aluminium oxide layers, the influence of the substrate bias used was not seen as critical but coatings deposited at a total pressure level of 3 μbar and not as deep in the reactive mode possessed a denser and less columnar structure than the coatings deposited at a higher pressure level of 6 or 12 μbar. The main constituent of defects was conductive carbon dust particles from the chamber walls. This would be improved by transferring the deposition of PVD aluminium oxide to a separate chamber. The increase in target size or the use of a backplate with the aluminium target to improve target cooling would most probably reduce the formation of aluminium droplets and thus reduce the defect density in the films.

## 8.2 Novelty of the study

It was demonstrated successfully in this research that it is possible to deposit functional piezoresistive hard carbon thin film sensors on steel substrates using APS and HVOF thermal spray aluminium oxide coatings as-deposited without the need for post-treatment in the electrical insulation of the sensor element. The beta value and gauge factor of such sensors are comparable to those earlier measured on a polyimide substrate.

The scientific novelty of the thesis is also the extensive study of moisture-induced polarization effects in porous aluminium oxide structures performed with the leakage current measurement concept described in Chapter 6.3.1. The polarization phenomena of aluminium oxide coatings were complex, starting from adsorbed water in chemisorbed state, changing to physiosorbed and finally to ionic movement in the electric field and anodic corrosion on the mild steel substrates. Direct current measurement cannot distinguish between surface and bulk conductivity but the rapid changes in leakage current seen close to the dew point temperatures implied that the huge changes measured in resistivity were related more to changes in surface resistivity caused by the condensed water on the hydrophilic γ-aluminium oxide surfaces of the thermal spray aluminium oxide coatings. This is also supported by the fact that the APS coatings without the use of a sealant showed a similar change in resistance close to dew point conditions at 80% RH. The adsorbed water in the aluminium oxide coatings caused more long-term drift influenced by the effect of ionic movement in the space charge polarization.

# 9 SUGGESTIONS FOR FUTURE WORK

The interaction between mild steel substrate and potential corrosive environment needs to be prevented by studying relevant corrosion-resistant intermediate coatings. For instance, in thermal spray coatings the use of a corrosion resistant, Ni-20Cr-based bond coatings needs to be tested for the prevention of corrosion observed on S235JR mild steel substrate.

If it is planned to use thin film PVD aluminium oxide coatings for electrical insulation between steel substrate and hard carbon thin film sensor layers, special attention must be paid to the deposition of void-free PVD coatings. As an example, the deposition of RF-sputtered aluminium oxide coatings needs to be repeated at a lower total pressure of 3 μbar and with improved target cooling.

# 10 BIBLIOGRAPHY

[1] J. Fraden, Handbook of Modern Sensors: Physics, Designs, and Applications, Fourth Edition, San Diego, California: Springer, 2010.

[2] J. Robertson, "Diamond-like amorphous carbon," *Materials Science and Engineering,* vol. 37, nos. 4-6, pp. 129-281, 2002.

[3] A. Tibrewala, E. Peiner, E. Bandorf, S. Biehl and H. Lüthje, "Piezoresistive effect in amorphous carbon thin films," *Materials Science and Technology,* vol. 23, no. 3, pp. 362-367, 2007.

[4] P. Regtien and E. Dertien, "4. Resistive sensors," in *Sensors for mechatronics*, Amsterdam, Springer, 2012, pp. 57-100.

[5] X. Ma, P. Guo, X. Tong, Y. Zhao, Q. Zhang, P. Ke and A. Wang, "Piezoresistive behavior of amorphous carbon films for high performance MEMS force sensors," *Applied physics letters,* vol. 114, no. 25, p. 253502, 2019.

[6] G. Song, Y. Wang and D. Q. Tan, "A review of surface roughness impact on dielectric film properties," *IET Nanodielectrics,* vol. 5, no. 1, pp. 1-23, 2022.

[7] P. Vuoristo, "4.10 Thermal Spray Coating Processes," in *Comprehensive Materials Processing*, Amsterdam, Netherlands, Elsevier, 2014, pp. 230-275.

[8] J. Martinez-Vega, Dielectric Materials for Electrical Engineering, London: Wiley, 2010.

[9] H. Schroeder, "Poole-Frenkel-effect as dominating current mechanism in thin oxide films—An illusion?!," *Journal of Applied Physics,* vol. 117, no. 21, pp. 215103-13, 2015.

[10] M. A. Laughton and D. F. Warne, “4. Fundamental properties of materials,” in *Electrical Engineer's Reference Book*, Oxford, Elsevier Science & Technology, 2002, pp. 3-8.

[11] J. M. Lackner and W. Waldhauser, “Adhesion Improvement of PVD Coatings by Plasma Treatmen tWith Linear Anode Layer Ion Sources,” in *50th Annual Technical Conference Proceedings (Society of Vacuum Coaters)*, Louisville, KY, USA, 2007.

[12] T. Olding, M. Sayer and D. Barrow, "Ceramic sol–gel composite coatings for electrical insulation," *Thin Solid Films,* Vols. 398-399, pp. 581-586, 2001.

[13] J. Wang, Y.-H. Yu, S. C. Lee and Y.-W. Chung, "Tribological and optical properties of crystalline and amorphous alumina thin films grown by low-temperature reactive magnetron sputter-deposition," *Surface and Coatings Technology,* Vols. 146-147, pp. 189-194, 2001.

[14] A. Schütze and D. T. Quinto, "Pulsed plasma-assisted PVD sputter-deposited alumina thin films," *Surface and Coatings Technology,* vol. 162, nos. 2-3, pp. 174-182, 2003.

[15] R. Matero, A. Rahtu, M. Ritala, M. Leskelä and T. Sajavaara, "Effect of water dose on the atomic layer deposition rate of oxide thin films," *Thin Solid Films,* vol. 368, no. 1, pp. 1-7, 2000.

[16] J. R. Davis, "Introduction to Thermal SprayTechnology," in *Handbook of Thermal Spray Processing*, Ohio, ASM International, 2004, pp. 3-13.

[17] P. Møller and L. Pleth Nielsen, "Thermal Spraying and Hardfacing," in *Advanced Surface Technology*, Washington, NASF National Association For Surface Finishing, 2012, pp. 671 - 703.

[18] D. E. Crawmer, "Thremal Spray Processes," in *ASM Handbook, Volume 5A, Thermal Spray Technology*, ASM International, 2013, pp. 33-53.

[19] G. Dwivedi, T. Nakamura and S. Sampath, "Controlled Introduction of Anelasticity in Plasma-Sprayed Ceramics," *Journal of the American Ceramic Society,* vol. 94, no. 1, pp. 104-111, 2011.

[20] P. Junge, M. Greinacher, D. Kober, P. Stargardt and C. Rupprecht, "Metastable Phase Formation, Microstructure, and Dielectric Properties in Plasma-Sprayed Alumina Ceramic Coatings," *Coatings,* vol. 12, no. 12, p. 1847, 2022.

[21] J. G. Odhiambo, W. Li and C. Li, "Porosity and Its Significance in Plasma-Sprayed Coatings," *Coatings,* vol. 9, no. 460, pp. 1-19, 2019.

[22] F.-L. Toma, L.-M. Berger, T. Naumann and S. Langner, "Microstructures of nanostructured ceramic coatings obtained by suspension thermal spraying," *Surface & Coatings Technology,* vol. 202, no. 18, pp. 4343-4348, 2008.

[23] P. Fauchais and G. Montavon, "Latest Developments in Suspension and Liquid Precursor Thermal Spraying," *Journal of Thermal Spray Technology,* vol. 19, no. 1, pp. 226-239, 2009.

[24] F.-L. Toma, L.-M. Berger, S. Scheitz, S. Langner, C. Rödel, A. Potthoff, V. Sauchuk and M. Kusnezoff, "Comparison of the microstructural characteristics and electrical properties of thermally sprayed Al2O3 coatings from aqueous suspensions and feedstock powders," *Journal of Thermal Spray Technology,* vol. 21, nos. 3-4, pp. 480-488, 2012.

[25] S. K. S. Harsha, Principles of Vapor Deposition of Thin Films, San Jose State University, CA, USA: Elsevier, 2006.

[26] A. Baptista, F. Silva, J. Porteiro, J. Míguez and G. Pinto, "Sputtering Physical Vapour Deposition (PVD) Coatings: A Critical Review on Process Improvement and Market Trend Demands," *Coatings,* vol. 8, no. 11, p. 22, 2018.

[27] R. Boidin, T. Halenkovič, V. Nazabal, L. Beneš and P. Němec, "Pulsed laser deposited alumina thin films," *Ceramics International,* vol. 42, no. 1, pp. 1177-1182, 2016.

[28] D. Depla, S. Mahieu and J. E. Greene, "Sputter Deposition Processes," in *Handbook of Deposition Technologies for Films and Coatings: Science, Applications and Technology*, Oxford, Elsevier Inc., 2009, pp. 253-294.

[29] M. Ohring, Materials Science of Thin Films, Burlington: Elsevier Science, 2001.

[30] R. Cremer, M. Witthaut, D. Neuschütz, G. Erkens, T. Leyendecker and M. Feldhege, "Comparative characterization of alumina coatings deposited by RF, DC and pulsed reactive magnetron sputtering," *Surface and Coatings Technology,* Vols. 120-121, pp. 213-218, 1999.

[31] B. G. Segda, M. Jacquet and J. P. Besse, "Elaboration, characterization and dielectric properties study of amorphous alumina thin films deposited by r.f. magnetron sputtering," *Vacuum,* vol. 62, no. 1, pp. 27-38, 2001.

[32] O. Zywitzki and G. Hoetzsch, "Influence of coating parameters on the structure and properties of Al2O3 layers reactively deposited by means of pulsed magnetron sputtering," *Surface & Coating Technology,* Vols. 86-87, nos. 1-3, pp. 640-647, 1996.

[33] J. Musil, J. Blažek, P. Zeman, Š. Prokšová, M. Šašek and R. Čerstvý, "Thermal stability of alumina thin films containing γ-Al2O3 phase prepared by reactive magnetron sputtering," *Applied Surface Science,* vol. 257, no. 3, pp. 1058-1062, 2010.

[34] J. Kohout, E. Bousser, T. Schmitt, R. Vernhes, O. Zabeida, J. Klemberg-Sapieha and L. Martinu, "Stable reactive deposition of amorphous Al2O3 films with low residual stress and enhanced toughness using pulsed dc magnetron sputtering with very low duty cycle," *Vacuum,* vol. 124, pp. 96-100, 2016.

[35] Y. Yamada-Takamura, F. Koch, H. Maier and H. Bolt, "Characterization of α-phase aluminum oxide films deposited by filtered vacuum arc," *Surface and Coatings Technology,* Vols. 142-144, pp. 260-264, 2001.

[36] K. S. Shamala, L. C. Murthy and K. Narasimha Rao, "Studies on optical and dielectric properties of Al2O3 thin films prepared by electron beam evaporation and spray pyrolysis method," *Materials Science and Engineering,* vol. 106, no. 3, pp. 269-274, 2004.

[37] S. Rossnagel, "Sputtering and Sputter Deposition," in *Handbook of Thin-Film Deposition Processes and Techniques*, Norwich New York, Noyes Publications, 2002, pp. 319-348.

[38] S. Berg, T. Nyberg and T. Kubart, "Modelling of Reactive Sputtering Processes," in *Reactive Sputter Deposition*, Berlin Heidelberg, Springer, 2008, pp. 131-151.

[39] P. Frach, K. Goedicke, C. Gottfried and H. Bartzsch, "A versatile coating tool for reactive in-line sputtering in different pulse modes," *Surface & Coatings Technology,* vol. 142, pp. 628-634, 2001.

[40] I. Safi, "Recent aspects concerning DC reactive magnetron sputtering of thin films: a review," *Surface and Coatings Technology,* vol. 127, no. 2-3, pp. 203-218, 2000.

[41] D. M. Mattox, “Physical Sputtering and Sputter Deposition,” in *Handbook of Physical Vapor Deposition (PVD) Processing*, The Boulevard, Langford Lane, Kidlington, Oxford OX5 IGB, UK, Elsevier, 2010, pp. 237-286.

[42] A. Hecimovic and J. T. Gudmundsson, "Preface to Special Topic: Reactive high power impulse magnetron sputtering," *Journal of Applied Physics,* vol. 121, no. 17, p. 171801, 2017.

[43] S. Kadlec and J. Capek, "Return of target material ions leads to a reduced hysteresis in reactive high power impulse magnetron sputtering: Experiment," *Journal of Applied Physics,* vol. 121, no. 17, p. 171911, 2017.

[44] Auerkari, Pertti;, Mechanical and physical properties of engineering alumina ceramics, Espoo: Technical Research Center Finland (VTT), 1996.

[45] I. Levin and D. Brandon, "Metastable Alumina Polymorphs: Crystal Structures and Transition Sequences," *Journal of the American Ceramic Society,* vol. 81, no. 8, pp. 1995-2012, 1998.

[46] S. Hao, C.-J. Li and G.-J. Yang, "Influence of Deposition Temperature on the Microstructures and Properties of Plasma-Sprayed Al2O3 Coatings," *Journal of Thermal Spray Technology,* vol. 20, nos. 1-2, pp. 160-169, 2011.

[47] F.-L. Toma, S. Scheiz, L.-M. Berger, V. Sauchuk, M. Kusnezov and S. Thiele, "Comparative Study of the Electrical Properties and Characteristics of Thermally Sprayed Alumina and Spinel Coatings," *Journal of Thermal Spray Technology,* vol. 20, no. 1, pp. 195-204, 2011.

[48] Y. Liu, T. E. Fischer and A. Dent, "Comparison of HVOF and plasma-sprayed alumina/titania coatings—microstructure, mechanical properties and abrasion behavior," *Surface and Coatings Technology,* vol. 167, no. 1, pp. 68-76, 2003.

[49] S. Sampath, "Thermal Spray Applications in Electronics and Sensors: Past, Present, and Future," *Journal of Thermal Spray Technology,* vol. 19, no. 5, pp. 921-949, 2010.

[50] C.-J. Li and A. Ohmori, "Relationships Between the Microstructure and Properties of Thermally Sprayed Deposits," *Journal of Thermal Spray Technology,* vol. 11, no. 3, pp. 365-374, 2002.

[51] C. J. Swindeman, R. D. Seals, W. P. Murray, M. H. Cooper and K. R. Forbes, "An investigation of thermally-sprayed aluminum oxide coatings for high-temperature electrostatic chucks (ESCs)," in *IEEE International Symposium on Semiconductor Manufacturing*, Austin, TX, USA, 1995.

[52] C. C. Stahr, S. Saaro, L.-M. Berger, J. Dubský, K. Neufuss and M. Herrmann, "Dependence of the Stabilization of α-Alumina on the Spray Process," *Journal of Thermal Spray Technology,* vol. 16, no. 5, pp. 822-830, 2007.

[53] G. Bolelli, L. Lusvarghi, T. Varis, E. Turunen, M. Leoni, P. Scardi, C. L. Azanza-Ricardo and M. Barletta, "Residual stresses in HVOF-sprayed ceramic coatings," *Surface & Coatings Technology,* vol. 202, no. 19, pp. 4810-4819, 2008.

[54] J. Gao, X. Xiong and Y. Gao, "The effect of the α/γ phase on the dielectric properties of plasma sprayed Al2O3," *Journal of Materials Science: Materials in Electronics,* vol. 28, no. 16, pp. 12015-12020, 2017.

[55] C. C. Stahr, S. Saaro, L.-M. Berger, J. Dubský, K. Neufuss and M. Herrmann, "Dependence of the Stabilization of a-Alumina on the Spray Process," *Journal of Thermal Spray Technology,* vol. 16, no. 5, pp. 822-830, 2007.

[56] R. McPherson, "On the formation of thermally sprayed alumina coatings," *Journal of Material Science,* vol. 15, no. 12, pp. 3141-3149, 1980.

[57] A. Sharma, "Thermal Spray Coatings for Electrical and Electronic Applications," in *ASM Handbook, Volume 5A, Thermal Spray Technology*, ASM International, 2013, pp. 262-269.

[58] W. Tillmann, K. Omar and A. Mohamed, "Porosity Characterization and Its Effect on Thermal Properties of APS-Sprayed Alumina Coatings," *Coatings,* vol. 9, no. 10, pp. 601-11, 2019.

[59] L. Pawlowski, "The relationship between structure and dielectric properties in plasma-sprayed alumina coatings," *Surface and Coatings Technology,* vol. 35, nos. 3-4, pp. 285-298, 1988.

[60] M. Niittymäki and K. Lahti, "Effect of temperature and humidity on dielectric properties of thermally sprayed alumina coatings," *IEEE Transactions on Dielectrics and Electrical Insulation,* vol. 25, no. 3, pp. 908-918, 2018.

[61] M. Niittymäki, I. Rytöluoto, K. Lahti, J. Metsäjoki and T. Suhonen, "Role of microstructure in dielectric properties of thermally sprayed ceramic coatings," in *2016 IEEE International Conference on Dielectrics (ICD)*, Montpellier, 2016.

[62] M. Niittymäki, J. Metsäjoki, T. Suhonen and K. Lahti, "Electric field dependency of dielectric behavior of thermally sprayed ceramic coatings," in *2015 IEEE 11th International Conference on the Properties and Applications of Dielectric Materials (ICPADM)*, Sydney, 2015.

[63] E. Turunen, T. Varis, S.-P. Hannula, A. Vaidya, A. Kulkarni, J. Gutleber, S. Sampath and H. Herman, "On the role of particle state and deposition procedure on mechanical, tribological and dielectric response of high velocity oxy-fuel sprayed alumina coatings," *Materials Science and Engineering,* vol. 415, nos. 1-2, pp. 1-11, 2006.

[64] J. Kotlan, R. C. Seshadri, S. Sampath, P. Ctibor, Z. Pala and R. Musalek, "On the dielectric strengths of atmospheric plasmasprayed Al2O3, Y2O3, ZrO2–7% Y2O3 and (Ba, Sr) TiO3 coatings," *Ceramics International,* vol. 41, pp. 11169-11176, 2015.

[65] E. J. Young, E. Mateeva, J. J. Moore, B. Mishra and M. Loch, "Low pressure plasma spray coatings," *Thin Solid Films,* vol. 377, pp. 788-792, 2000.

[66] M. Niittymäki, K. Lahti, T. Suhonen and J. Metsäjoki, "Dielectric Breakdown Strength of Thermally Sprayed Ceramic Coatings: Effects of Different Test Arrangements," *Journal of Thermal Spray Technology,* vol. 24, pp. 542-551, 2015.

[67] Iron Boar Labs Ltd., www.makeitfrom.com.

[68] H.-J. Kim, S. Odoul, C.-H. Lee and Y.-G. Kweon, "The electrical insulation behavior and sealing effects of plasma-sprayed alumina-titania coatings," *Surface and Coatings Technology,* vol. 140, no. 3, pp. 293-301, 2001.

[69] S. M. Rossnagel, "Use of plasmas in deposition technologies," in *Advanced Surface Coatings: A Handbook of Surface Engineering*, New York, Springer, 1991, pp. 14-40.

[70] J. A. Thornton, "Influence of apparatus geometry and deposition conditions on the structure and topography of thick sputtered coatings," *Journal of Vacuum Science & Technology,* vol. 11, no. 4, pp. 666-670, 1974.

[71] J. A. Thornton, "The microstructure of sputter-deposited coatings," *Journal of Vacuum Science & Technology,* vol. 4, no. 6, pp. 3059-3065, 1986.

[72] W. Engelhart, W. Dreher, O. Eibl and V. Schier, "Deposition of alumina thin film by dual magnetron sputtering: Is it γ-Al2O3?," *Acta Materialia,* vol. 59, no. 20, pp. 7757-7767, 2011.

[73] O. Zywitzki, G. Hoetzsch, F. Fietzke and K. Goedicke, "Effect of the substrate temperature on the structure and properties of Al2O3 layers reactively deposited by pulsed magnetron sputtering," *Surface and Coatings Technology,* vol. 82, nos. 1-2, pp. 169-175, 1996.

[74] F. Fietzke, K. Goedicke and W. Hempel, "The deposition of hard crystalline Al2O3 layers by means of bipolar pulsed magnetron sputtering," *Surface and Coatings Technology,* Vols. 86-87, nos. 1-3, pp. 657-663, 1996.

[75] O. Zywitzki and G. Hoetsch, "Correlation between structure and properties of reactively deposited Al2O3 coatings by pulsed magnetron sputtering," *Surface and Coatings Technology,* Vols. 94-95, nos. 1-3, pp. 303-308, 1997.

[76] R. Cremer, K. Reichert, D. Neuschütz, G. Erkens and T. Leyendecker, "Sputter deposition of crystalline alumina coatings," *Surface and Coatings Technology,* Vols. 163-164, pp. 157-163, 2003.

[77] F. Carreri, R. Bandorf, H. Gerdes, M. Vergöhl and G. Bräuer, "Highly insulating alumina films by a bipolar reactive MF sputtering," *Surface & Coatings Technology,* vol. 290, pp. 82-86, 2016.

[78] J. M. Schneider, W. D. Sproul and M. Allan, "Phase formation and mechanical properties of alumina coatings prepared at substrate temperatures less than

500 °C by ionized and conventional sputtering," *Surface and Coatings Technology,* Vols. 94-95, pp. 179-183, 1997.

[79] J. M. Schneider, W. D. Sproul, A. A. Voevodin and A. Matthews, "Crystalline alumina deposited at low temperatures by ionized magnetron sputtering," *Journal of Vacuum Science & Technology A: Vacuum, Surfaces, and Films,* vol. 15, no. 3, pp. 1084-1088, 1997.

[80] M. Sridharan, M. Sillassen, J. Bøttiger, J. Chevallier and H. Birkedal, "Pulsed DC magnetron sputtered Al2O3 films and their hardness," *Surface and Coatings Technology,* vol. 202, nos. 4-7, pp. 920-924, 2007.

[81] Q. Li, Y.-H. Yu, C. Singh Bhatia, L. D. Marks, S. C. Lee and Y. W. Chung, "Low-temperature magnetron sputter-deposition, hardness, and electrical resistivity of amorphous and crystalline alumina thin films," *Journal of Vacuum Science & Technology,* vol. 18, no. 5, pp. 2333-2338, 2000.

[82] A. Khanna, D. G. Bhat, A. Harris and B. D. Beake, "Structure-property correlations in aluminum oxide thin films grown by reactive AC magnetron sputtering," *Surface and Coatings Technology,* vol. 201, no. 3, pp. 1109-1116, 2006.

[83] V. Edlmayr, M. Moser, C. Walter and C. Mitterer, "Thermal stability of sputtered Al2O3 coatings," *Surface and Coatings Technology,* vol. 204, nos. 9-10, pp. 1576-1581, 2010.

[84] J. Andersson, E. Wallin, U. Helmersson, U. Kreissig and E. Munger, "Phase control of Al2O3 thin films grown at low temperatures," *Thin Solid Films,* vol. 513, nos. 1-2, pp. 57-59, 2006.

[85] P. Eklund, M. Sridharan, M. Sillassen and J. Bøttiger, "α-Cr2O3 template-texture effect on α-Al2O3 thin-film growth," *Thin Solid Films,* vol. 516, no. 21, pp. 7447-7450, 2008.

[86] J. Lin, "High rate reactive sputtering of Al2O3 coatings by HiPIMS," *Surface and Coatings Technology,* vol. 357, pp. 402-411, 2019.

[87] P. Vuoristo, T. Mäntylä, P. Kettunen and R. Lappalainen, "Stoichiometry and impurities in sputtered alumina films on copper," *Thin Solid Films,* vol. 204, no. 2, pp. 297-311, 1991.

[88] C.-M. Chiang and L.-S. Chang, "Microstructure and characterization of aluminum oxide thin films prepared by reactive RF magnetron sputtering on copper," *Surface and Coatings Technology,* vol. 198, nos. 1-3, pp. 152-155, 2005.

[89] E. Wallin, J. Andersson, M. Lattemann and U. Helmersson, "Influence of residual water on magnetron sputter deposited crystalline Al2O3 thin films," *Thin Solid Films,* vol. 516, no. 12, pp. 3877-3883, 2008.

[90] J. M. Schneider, K. Larsson, J. Lu, E. Olsson and B. Hjörvarsson, "Role of hydrogen for the elastic properties of alumina thin films," *Applied Physics Letters,* vol. 80, no. 7, pp. 1144-1146, 2002.

[91] T. Mäntylä, P. Vuoristo, A. Telama and P. Kettunen, "Electrical insulating properties and thermal stability of r.f.-sputtered alumina coatings," *Thin Solid Films,* vol. 126, no. 1, pp. 43-49, 1985.

[92] P. Vuoristo, T. Mäntylä and P. Kettunen, "Properties of magnetron-sputtered electrically insulating Al2O3 coatings on copper," *Journal of Materials Science,* vol. 27, no. 18, pp. 4985-4996, 1992.